



UNITED NATIONS
UNIVERSITY

UNU-GTP

 **ORKUSTOFNUN**



Water jets from Deildartunga hot spring, W-Iceland

Gaetan Sakindi

**THREE-DIMENSIONAL INVERSION OF MAGNETOTELLURIC
DATA: GEOLOGICAL/GEOTHERMAL INTERPRETATION OF
ASAL GEOTHERMAL FIELD, DJIBOUTI**

Report 4
December 2015



UNITED NATIONS
UNIVERSITY

UNU-GTP

Geothermal Training Programme

Orkustofnun, Grensasvegur 9,
IS-108 Reykjavik, Iceland

Reports 2015
Number 4

THREE-DIMENSIONAL INVERSION OF MAGNETOTELLURIC DATA: GEOLOGICAL/GEOTHERMAL INTERPRETATION OF ASAL GEOTHERMAL FIELD, DJIBOUTI

MSc thesis

School of Engineering and Natural Sciences
Faculty of Earth Sciences
University of Iceland

by

Gaetan Sakindi

Rwanda Energy Group (REG)
Energy Development Corporation, Ltd.
KN 82 St | P O Box 537 Kigali
gsakindi@edcl.reg.rw; sgaetan16@gmail.com

United Nations University
Geothermal Training Programme
Reykjavík, Iceland
Published in December 2015

ISBN 978-9979-68-375-9
ISSN 1670-7427

This MSc thesis has also been published in May 2015 by the
School of Engineering and Natural Sciences, Faculty of Earth Sciences
University of Iceland

INTRODUCTION

The Geothermal Training Programme of the United Nations University (UNU) has operated in Iceland since 1979 with six-month annual courses for professionals from developing countries. The aim is to assist developing countries with significant geothermal potential to build up groups of specialists that cover most aspects of geothermal exploration and development. During 1979-2015, 613 scientists and engineers from 59 developing countries have completed the six-month courses, or similar. They have come from Africa (37%), Asia (37%), Central America (15%), Europe (10%), and Oceania (1%) There is a steady flow of requests from all over the world for the six-month training and we can only meet a portion of the requests. Most of the trainees are awarded UNU Fellowships financed by the Government of Iceland.

Candidates for the six-month specialized training must have at least a BSc degree and a minimum of one year practical experience in geothermal work in their home countries prior to the training. Many of our trainees have already completed their MSc or PhD degrees when they come to Iceland, but many excellent students with only BSc degrees have made requests to come again to Iceland for a higher academic degree. From 1999 UNU Fellows have also been given the chance to continue their studies and study for MSc degrees in geothermal science or engineering in co-operation with the University of Iceland. An agreement to this effect was signed with the University of Iceland, and a similar agreement has recently also been signed with Reykjavik University. The six-month studies at the UNU Geothermal Training Programme form a part of the graduate programme.

It is a pleasure to introduce the 44th UNU Fellow to complete the MSc studies at the University of Iceland under the co-operation agreement. Gaetan Sakindi, BSc in Applied Physics, from Rwanda Energy Group (REG) - Energy Development Corporation, Ltd., completed the six-month specialized training in Geophysical Exploration at the UNU Geothermal Training Programme in October 2012. His research report was entitled: *Analysing the subsurface resistivity structure on two profiles across the Námafjall high-temperature geothermal field, NE-Iceland, through 1D joint inversion of TEM and MT data*. After one year of geothermal research work in Rwanda, he came back to Iceland for MSc studies at Faculty of Earth Sciences in August 2013. In May 2015, he defended his MSc thesis presented here, entitled: *Three-dimensional inversion of magnetotelluric data: geological/geothermal interpretation of Asal geothermal field, Djibouti*. His studies in Iceland were financed by the Government of Iceland through a UNU-GTP Fellowship from the UNU Geothermal Training Programme. We congratulate him on his achievements and wish him all the best for the future. We thank the Faculty of Earth Sciences at the School of Engineering and Natural Sciences of University of Iceland for the co-operation, and his supervisors for the dedication.

Finally, I would like to mention that Gaetan's MSc thesis with the figures in colour is available for downloading on our website www.unugtp.is, under publications.

With warmest greetings from Iceland,

Lúdvík S. Georgsson, director
United Nations University
Geothermal Training Programme

ACKNOWLEDGEMENTS

I would like to express my sincere appreciation to Gylfi Páll Hersir and Knútur Árnason of Iceland GeoSurvey (ISOR) for their indispensable support; technical guidance, advice and helpful comments from the beginning to the end of this research. This project would not have been completed without your constant supervision. Many thanks also to Ragna Karlsdóttir and Arnar Már Vilhjálmsson (ISOR) for your assistance, knowledge and constructive discussions during processing of the data. I am also deeply indebted to the entire staff of Orkustofnun and ÍSOR for your hospitable support in all aspects of this work. I also want to thank the Government of Djibouti for allowing the use of the resistivity data from Djibouti.

Special thanks go to the United Nations University Geothermal Training Programme (UNU-GTP) and the Government of Iceland for sponsoring my Master's studies at the University of Iceland. In a more special way, I extend sincere gratitude to the Director of the UNU-GTP, Mr. Lúdvík S. Georgsson, the Deputy Director, Mr. Ingimar G. Haraldsson and their extra-ordinary dedicated team; Ms. Thórhildur Ísberg, Ms. Málfrídur Ómarsdóttir, Ms. María S. Guðjónsdóttir and Mr. Markús A.G. Wilde for their great care and help throughout the entire study period. Many thanks also to all the UNU-GTP MSc and PhD Fellows for their un-measurable friendship and various discussions during my stay in Iceland; in particular, Mr. Samuel Kinyua Munyiri and Mr. Gift Wellington Tsokonombwe for sharing their expertise in making my maps.

I would also like to express my gratitude to the Government of Rwanda through the Rwanda Energy Group (REG) Ltd. / Energy Development Corporation for awarding me this important opportunity; that has enhanced my knowledge and technical skills and thus earning me a master's degree. To my colleagues in GDU your contributions and encouragements are highly appreciated.

Thank you to my beloved wife Clementine Nyirabashumba, my parents, brothers, sisters and friends for being with me all along my steps of life. May the almighty God bless you all and everyone who contributed by near or far toward this important achievement. Above all, thanks to the Almighty God, who has made all things possible!

DEDICATION

To my beloved wife, parents, brothers, sisters and friends.

...Your love, your patience moral support and understanding have lightened up my spirit to accomplish my master's studies....

ABSTRACT

This research study is aiming at becoming acquainted with the resistivity method and different ways of performing interpretation of MT data for deep lying subsurface investigations. The MT data collected from Asal geothermal area were used; the comparison between the results of 1-D inversion carried out previously and 3-D inversion is performed. A total of 105 MT soundings were considered in this research project and the same number of corresponding TEM soundings collected at nearby sites. To allow the static shift correction in the 1-D inversion, the MT data were jointly inverted with TEM data. Shift correction was then applied to the two polarizations for 3-D inversion. The modern computing systems have made 3-D modelling of MT data achievable and it is now becoming common and useful for detailed subsurface surveys in geothermal industries as well as in other fields including ground water, oil and natural gas and mineral exploration.

The WSINV3DMT code was used to perform 3-D inversion of the static shift corrected off-diagonal impedance tensor elements. Three different initial models were considered in order to test the inversion robustness and 31 periods evenly distributed on logarithmic scale from 0.003 to 300 s were used. The first initial model was compiled from the joint 1-D inversion of TEM and MT soundings; the second was a homogeneous earth of resistivity 10 Ωm and the third initial model was a homogeneous earth with a resistivity 50 Ωm . The RMS in all three different initial models was not of big difference with values of 1.44, 1.48 and 1.87, respectively. The final models gave similar resistivity structures underneath Asal rift and are presented here as iso-depth resistivity maps and cross-sections.

The result of the interpretation shows four main resistivity structures below the geothermal area: A shallow lying thin high resistivity layer followed by low resistivity (conductive cap). Below there is a high resistivity layer (resistive core) underlain by a deep lying conductor. Lithology based on well data shows that the shallow thin high resistivity layer corresponds to dry basaltic rocks covering the surface, the conductive layer reflects saline fluids but correlates also with low temperature alteration (smectite and zeolites), the deep resistive core correlates with the high temperature alteration minerals (chlorite and epidote) whereas the deep seated conductive body is most likely connected to the heat source of the Asal geothermal system.

At sea level, high resistivity dominates the northeast part of Asal rift towards Lake Asal in the vicinity of Ardoukoba volcano and the southeast part of the rift around Baddikoma region. An updoming conductive cap intersects the high resistivity, running NE-SW and reflects presumably alteration within the geothermal system. It covers the central part of the Asal rift including the Fiale explosion crater (Lava Lake). This is the same area where the fumaroles and hot springs in the Asal rift are located.

TABLE OF CONTENTS

	Page
1. INTRODUCTION	1
2. GENERAL GEOLOGY AND GEOTHERMAL CONDITIONS OF ASAL RIFT	3
2.1 Geology of Asal geothermal area	3
2.2 Geothermal manifestations in Asal rift	3
2.3 Previous geoscientific studies and outcomes	4
2.3.1 Geochemical survey	6
2.3.2 Gravity survey	6
2.3.3 Seismic survey	7
2.3.4 Deep exploration drilling	7
3. APPLICATION OF EM RESISTIVITY METHODS FOR GEOTHERMAL EXPLORATION	9
3.1 Resistivity of rocks	9
3.1.1 Interpretation of resistivity anomaly in geothermal system	11
3.2 Diverse methods for resistivity measurements	12
4. MAGNETOTELLURIC (MT) METHOD	14
4.1 Concepts of MT	14
4.2 Source field of MT signals and the depth of penetration	15
4.3 Electromagnetic waves in a conductive medium	17
4.3.1 Non-vertical incidence on conductive half-space	17
4.3.2 The EM in horizontally layered Earth	19
4.3.3 Conductivity in a homogeneous medium	21
4.3.4 MT transfer functions	21
4.3.5 Mathematical rotation of the impedance	25
4.3.6 Geoelectric strike analysis for MT data	26
4.3.7 Dimensionality measures	26
5. THE TRANSIENT ELECTROMAGNETIC (TEM) METHOD	28
5.1 TEM general concept	28
5.2 Calculation for voltage in central loop TEM	29
6. RESISTIVITY SURVEY IN ASAL GEOTHERMAL AREA	31
6.1 MT field instrumentation and data collection	31
6.2 The MT data processing algorithm	32
6.2.1 Data review and editing	33
6.2.2 Conversion of time series to frequency domain	33
6.2.3 Robust estimation of transfer functions	33
6.3 Remote reference and MT impedance estimation	34
6.4 TEM survey instrumentations at Asal rift	35
6.5 TEM data processing	36
7. MODELLING OF EM DATA FROM ASAL GEOTHERMAL AREA	37
7.1 Inversion of geophysical data	37
7.2 Applying 1-D inverse modelling code	38
7.3 Application of WSINV3DMT code for 3-D inversion	38
7.3.1 Data preparation and 3-D inversion	39
7.3.2 Static shift analysis for 3-D inversions	39
7.3.3 Model mesh grid design for 3-D inversion	40
7.3.4 Modelling parameters and initial models	41
7.4 Presentation of 3-D inversion results	43
7.4.1 Initial models and their respective outcomes	43

	Page
7.4.2 Iso-depth resistivity maps produced from 3-D inversion	46
7.4.3 Resistivity cross-sections produced from 3-D inversion	53
7.5 Geological/Geothermal interpretation of 3-D resistivity model of Asal rift.....	56
8. CONCLUSIONS AND RECOMMENDATIONS	58
REFERENCES	59
APPENDIX A: 3-D MT inversion responses.....	64
APPENDIX B: Iso-resistivity maps produced from 3-D inversion	76
APPENDIX C: Resistivity cross-sections.....	79

LIST OF FIGURES

1. Geological map of Asal.....	1
2. Structural map of Asal geothermal field	4
3. A map showing the two main geothermal manifestations within Asal rift	5
4. Lithology, temperature plot and alteration zones for well Asal-5.....	8
5. Typical average resistivity values for different rock types	9
6. Sketch showing the main conduction mechanisms.....	10
7. The general resistivity structure and alteration of the basaltic crust summarized.....	12
8. Illustration of MT set up for data acquisition.....	14
9. The average monthly sunspot number	16
10. The mean amplitude of the natural magnetic field spectrum	17
11. One-dimensional schematic model	23
12. Two-dimensional resistivity model.....	23
13. Three-dimensional resistivity model.....	25
14. Rotation of reference frame	26
15. Polar diagrams of the impedance tensor	27
16. TEM sounding set up	28
17. Basic principles of the TEM method	29
18. Locational map of the Asal geothermal field showing MT and TEM soundings	31
19. 1-D joint inversion of a TEM sounding and polarization of nearby MT soundings	40
20. Histograms of the shift multipliers, S_{xy} and S_{yx}	40
21. Horizontal slice showing vertical grid planes in the central part of the grid mesh for 3-D inversion.....	41
22. Data fit given as example for MT 055 and MT 039.....	42
23. Raw model, resistivity cross-section along x-axis (NS-E) at $y = 1000$ m	43
24. Resistivity maps at sea level showing comparison of results from different initial models ..	44
25. Resistivity maps at 1500 m b.s.l. showing results from different initial models	45
26. Resistivity cross-sections (EW-N) reproduced from 3-D inversion with different initial models.....	46
27. Resistivity cross-sections (NS-E) reproduced from 3-D inversion with different initial models.....	46
28. Iso-depth resistivity map at sea level	47
29. Resistivity map at 100 m b.s.l.	47
30. Resistivity map at 500 m b.s.l.	48
31. Resistivity map at 1000 m b.s.l.	48
32. Resistivity map at 2500 m b.s.l.	49
33. Resistivity map at 3500 m b.s.l.	49
34. Resistivity map at 4500 m b.s.l.	50

	Page
35. Resistivity models at sea level	51
36. Resistivity models at 500 b.s.l.	52
37. Comparison between resistivity cross-sections generated from 1-D and 3-D inversion.....	53
38. Resistivity cross-sections along the Asal rift parallel to x-axis of the internal coordinate system	54
39. Resistivity cross-sections across the Asal rift parallel to y-axis of the internal coordinate system	55
40. Alteration mineralogy in well Asal-4 and 1-D inversion of a nearby TEM sounding.....	56

ABBREVIATIONS AND SYMBOLS

MT	Magnetotelluric
AMT	Audio - Magnetotelluric
TEM	Transient ElectroMagnetic
EM	ElectroMagnetic
TE	Transverse Electric
TM	Transverse Magnetic
EDI	Electrical Data Interchange files
WSINV3DMT	3-D Inversion Program
1-D	One dimensional
2-D	Two dimensional
3-D	Three dimensional
m a.s.l.	Metres above sea level
m b.s.l.	Metres below sea level
TEMTD	1-D inversion program of MT and TEM data, separate or joint inversion
V8	Phoenix TEM equipment
$E(V/m)$	Electric field intensity
$B(T)$	Magnetic induction
$H(A/m)$	Magnetic field intensity
$D(C/m^2)$	Electric displacement
$\eta(C/m^3)$	Electric charge density of free charges
$J(A/m^2)$	Electric current density
$\sigma(S/m)$	Electric conductivity
$\mu(H/m)$	Magnetic permittivity
$\epsilon(F/m)$	Electric permittivity
$\delta(m)$	Electromagnetic skin depth
T(s)	Period
f(Hz)	Frequency
t(s)	Time
$\omega(rad/s)$	Angular frequency
$\rho(\Omega m)$	Resistivity (specific resistivity)
$\hat{Z}(\Omega)$	Impedance tensor (2x2 matrices)
$\rho_a(\Omega m)$	Apparent resistivity
$\Phi(^{\circ})$	Impedance phase
$i = \sqrt{-1}$	Imaginary number
$k (1/m)$	Propagation constant (wave number)
x, y and x', y'	Reference frame and reference frame rotated through an angle θ
\mathcal{T}	Tipper
\Re	Real part of the Tipper
\Im	Imaginary part of the Tipper
M_r	Length of the real part of the induction arrow
M_q	Length of the imaginary part of the induction arrow

1. INTRODUCTION

The magnetotelluric method has had an outstanding improvement since its initiation in the 1950s both regarding development of the methodology as well as the capacity of the method to solve different geological structures. The MT method is the main branch of EM techniques, introduced by Tikhonov (1950) and Cagniard (1953). EM theory originates from the four fundamental equations proposed by James Clerk Maxwell. Up to today, the MT technique is still the most powerful method for investigating the deeper lying structure in the subsurface and for describing the resistivity distribution within the area of interest. The measured apparent resistivity is inverted to the actual subsurface resistivity structure by applying multidimensional modelling. The geological meaning comes around to support the interpretation. The method has been successful in exploration of geothermal resources in different fields.

Asal geothermal field in Djibouti lies in the East African rift valley (Figure 1) and is covered by volcanic rocks; thermal manifestations are widespread. The exploration for geothermal resources in Asal started in the 1970s. The EM data that are used in this project were collected in two surveys; the first one in 1988 (Árnason et al., 1988) and second survey in 2007 (Árnason et al., 2008). In 1988, a TEM resistivity survey was carried out by Orkustofnun (National Energy Authority of Iceland). An MT resistivity survey was followed in the second phase in 2007 carried out by ISOR on behalf of Reykjavik Energy Invest where 109 MT soundings were collected for deeper lying structures. The joint processing technique was used to correct the static shift problems encountered by MT. In this project, 105 MT soundings and an equal number of TEM soundings are used. The main objectives of this research are highlighted in the following:

1. To become acquainted with the resistivity method and ways of using multidimensional interpretation of MT data for deep subsurface investigations.
2. To use MT data from Asal geothermal area; compare previous 1-D inversion to 3-D results and characterize the reservoir through a conceptual model.

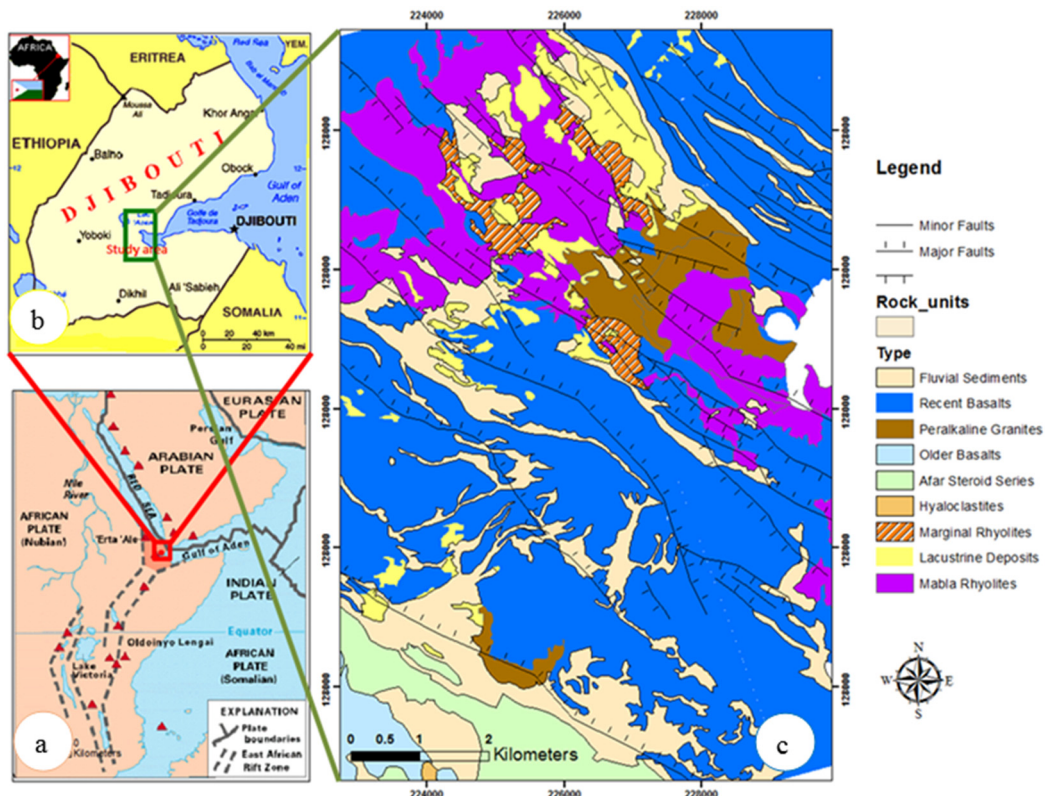


FIGURE 1: Geological map of Asal (c. modified from Stieltjes, 1979) with an insert of triple junction (a. modified from Corti, 2012) and geographical location of Djibouti (b. modified from Geographic.org, 2015)

As an outcome of the research, we will be able to understand and get to know in more details the subsurface resistivity structures, the size and extent of the geothermal area and main characteristics of the geothermal reservoir in Asal rift through comparison with results from existing boreholes. The final result will be the construction of a conceptual model which will be used to site productive wells. In Chapter two, we discuss the general geological set-up and geothermal conditions of the area, previous surveys from reconnaissance to exploration drilling and their findings. The third Chapter discusses the application of EM resistivity methods for geothermal exploration; the resistivity of rocks and resistivity in a general perspective, the relation between the electrical resistivity and resistivity of rocks, mineral conduction mechanisms and their interpretation in geothermal systems. Magnetotelluric (MT) technique is detailed in the fourth Chapter while Transient Electromagnetic (TEM) is discussed in the fifth Chapter. The resistivity survey in Asal geothermal area; MT and TEM instrumentations, data acquisition and data processing are described in Chapter six. Chapter seven discusses the modelling of EM resistivity methods. Finally, conclusion and recommendation are debated in Chapter eight.

2. GENERAL GEOLOGY AND GEOTHERMAL CONDITIONS OF ASAL RIFT

The Asal rift is the landwards extension of the Aden Tadjoura spreading ridge (Figure 1). The geology of Asal Rift is characterized by an extensional graben, generally in basaltic environment (Dalha basalts (6-8 Ma) and the basaltic stratoid series (1-4 Ma)) between Ghoubbet and Lake Asal (155 m b.s.l.). The rift is characterized by volcanic relief in origin; formed by series of successive volcanic activities caused by tectonic movements. It is the same formation which was found within the Asal Rift in the 1960s; it shows tectono-magmatic structures crisscrossing the ocean bed (Árnason and Flóvenz, 1995). The rift was opened during the Pleistocene as westward extension of the Gulf of Aden-Tadjura spreading axis. It extends about 11 km to the northwest from the bay of Ghoubbet al Kharab to Lake Asal located 155 m below sea level. The rift is about 10 km wide and is characterized by extensive faulting and volcanic activity with the latest eruption occurring in 1978. The spreading rate of the Asal Rift has been estimated to be about 1.5 cm/year (Delibrias et al., 1975). The rift is often divided into an external rift which is characterized by large normal faults and inner rift; characterized by vertical faults and fissures. The actual rifting and volcanic activity is confined to the inner rift.

2.1 Geology of Asal geothermal area

The geological formation of Asal Rift is generally of basaltic origin where the rift is surrounded by the Dalha basalts (6-8 Ma) and the basaltic stratoid series (1-4 Ma). A basaltic lava shield (Asal series), with a centre close to Lava Lake in southeastern part of the inner rift, covered most of the rift at one time. This shield, which is now broken by large faults, mostly covers hyaloclastite that is found inside the southern part of the external rift (Figure 1). In the inner rift phreatic tuff mostly underlies recent lava flows. Lava Lake is a large phreatic crater whose bottom is covered with recent basaltic lava (Árnason and Flóvenz, 1995).

Asal rift is an active frontier that can serve as reference point to observe and monitor the evolution of an ocean. This oceanization stops at the NNE displacement of the Arabian plate as it separates from the African plate. So far, the Arabian plate is still attached to Africa through the Afar depression that comprises the territory of Djibouti. This huge depression, which extends into Ethiopia and Eritrea, is crisscrossed by a complex system of large cracks and faults of which the most active ones lie between Ghoubbet-Kharab basin and Asal rift.

The Asal rift region is dominated by very recent volcanic rocks. The region has been regarded as a high potential geothermal field due to its geological situation. In this region, three main geological formations are highlighted and are correlated with borehole data. Starting from the uppermost geological strata; Asal series (recent basalts) with volcanism dating from the last 800,000 years (volcanism of the external margins of Asal, central volcanism and axial volcanism), the initial basalt series (stratoid basalt series) covering the period from 1-4 Ma and the Dalha basalt series dating between 6-8 Ma (Stieltjes, 1976). According to Stieltjes et al. (1976); the active volcanic and tectonic nature of Asal range which is displaying a continuous basaltic activity in the recent Quaternary period, with a magmatic evolution by crystal fractionation and typical rift structure of the present activity along the axis. They were considered to be indications of a magmatic heat source at shallow depth. The last eruption of Ardoukoba (Figure 2) in 1978 has been followed by a rifting episode up to 2 m opening along the axis of the Asal-Ghoubbet (Ruegg et al., 1979). An active nature of magmatic-tectonic rift segment has been confirmed. This period was followed by several years of reactivation of the Fiale explosion crater (Lava Lake), newly replenished with magma at shallow depth. From seismic sources; several episodes of magma injection were observed in the period between 1998 and 2001 (Doubre et al., 2007).

2.2 Geothermal manifestations in Asal rift

In the Asal rift, geothermal surface manifestations are linked to volcanic activities. The underground geothermal activities are reflected on the surface by the presence of alteration, hot springs and fumaroles (Figure 2). The warm springs with temperature ranging between 30 and 80°C are abundant in East part

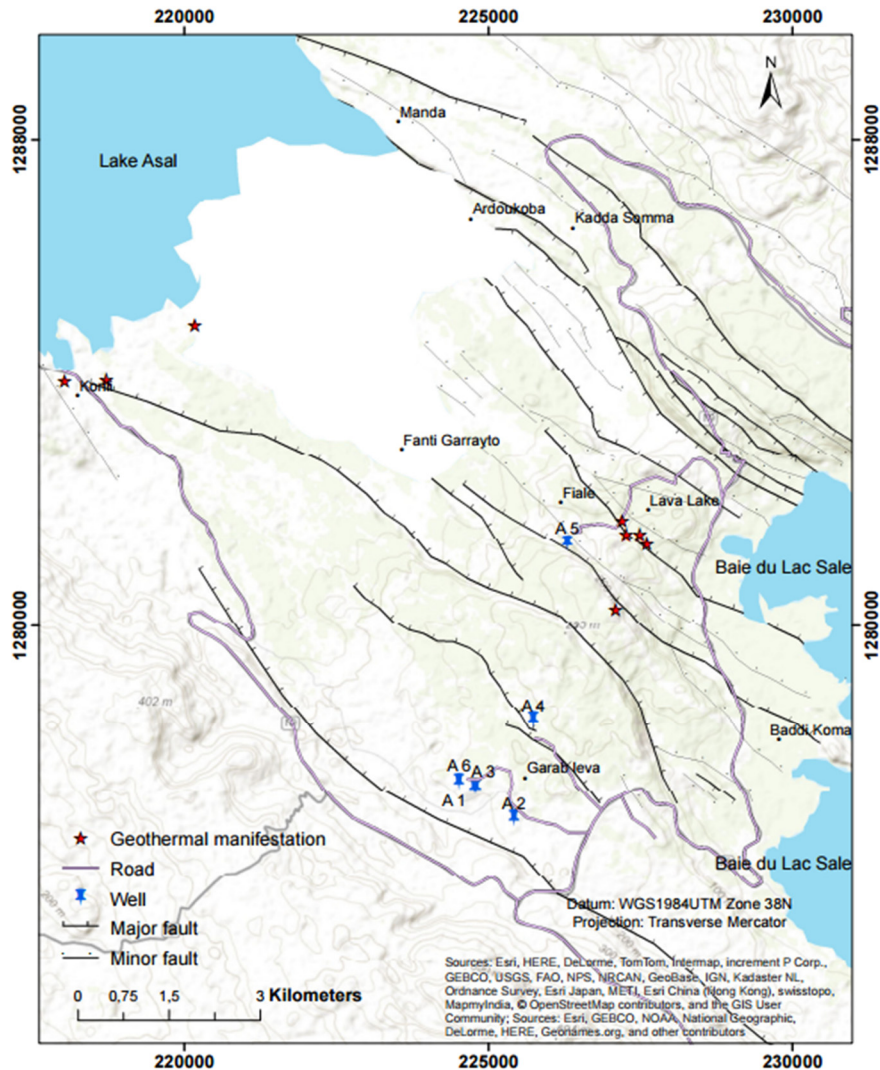


FIGURE 2: Structural map of Asal geothermal field showing geothermal manifestations, and well locations (modified from Doubre, 2004)

of Lake Asal. In the rift between Lake Asal and the Gulf of Ghoubbet, the water table is located below the ground surface and for this reason only the fumaroles are appearing on the surface. They are mainly found in two zones (see Figure 3); one is oriented NW-SE which elongates in the external rift with maximum temperature of 66°C and another zone in the southern part to the south of Lava Lake in the inner rift, with temperature of 99°C (Árnason and Flóvenz, 1995).

2.3 Previous geoscientific studies and outcomes

The exploration activities for geothermal resources in Djibouti started in the 1970s. Two consulting firms from France; BRGM and CNRS conducted geological, geochemical and geophysical surveys especially in the Asal rift (Dague et al., 1973). The exploration also included the drilling of eleven temperature gradient wells with depths varying from 50 to 180 m. From the results of the temperature gradient wells; the Asal rift was classified as a high temperature geothermal field (Stieltjes, 1976). The next phase was the drilling of deep wells in 1975; two wells A-1, 1554 m deep and A-2, 1147 m deep, were sited based on the geoscientific studies and drilled in the SW part of Asal rift. Well A-1 has shown a feed zone at a depth of 1137 m. The same feed zone was not seen in well A-2. Well A-2 did not show a permeable zone; however, it showed high temperatures above 260°C. Later, the exploration for geothermal resources in Djibouti was carried out by Aquater (Italian company) in the 1980s (Aquater, 1989). The exploration was targeting the Hanle area which is located about 60 km SW of the Asal rift.

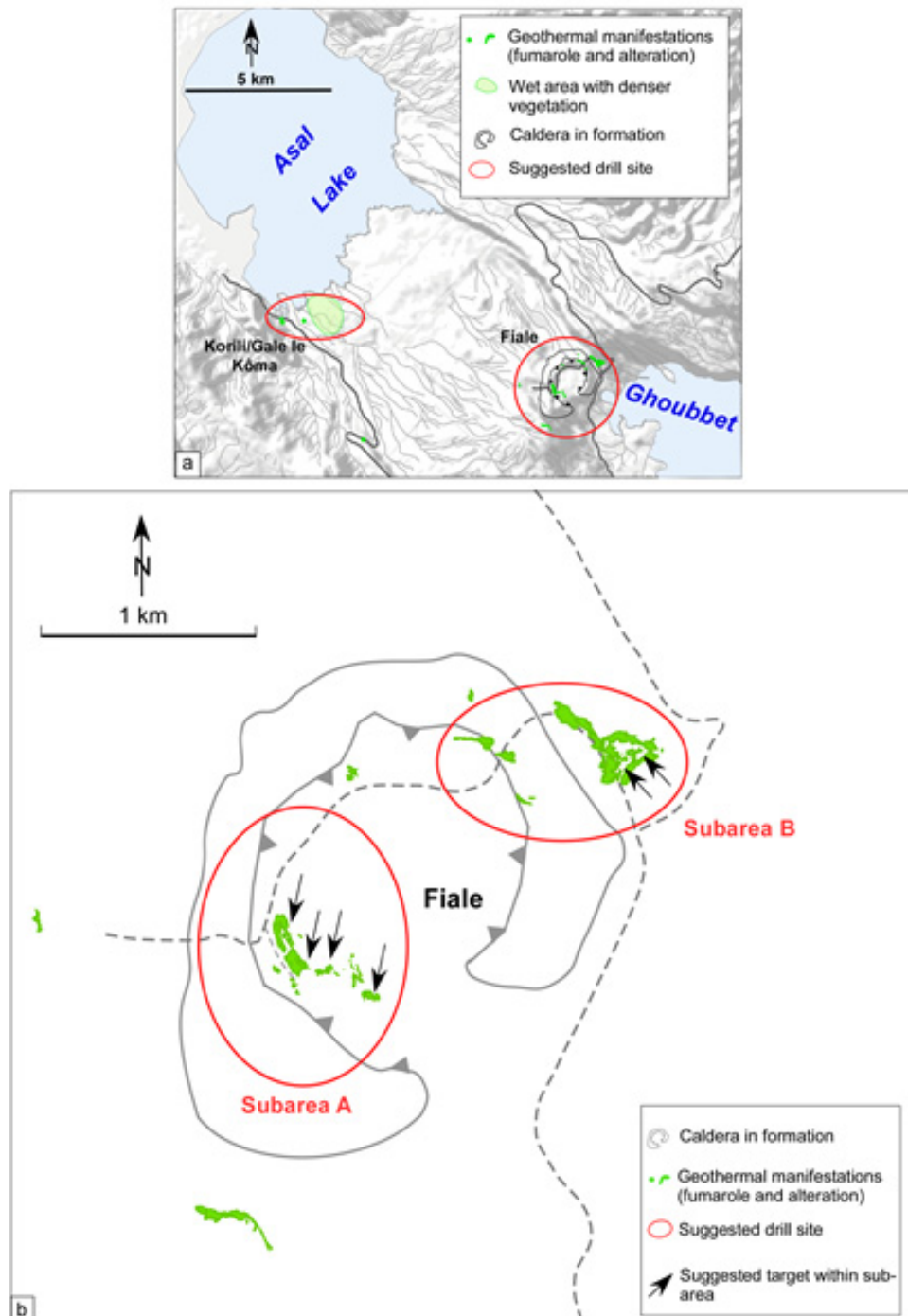


FIGURE 3: A map showing the two main geothermal manifestations within Asal rift; Korili/Gale le Kôma and Fiale viewed from the whole map (a) and zoom in of Fiale caldera (b) (modified from Árnason et al., 2008)

The exploration was finalised by the drilling of two wells in Hanle whose results are not convincing since they revealed temperatures lower than 124°C and the main target was the Asal rift. Since then; four more deep wells were drilled in the Asal rift (Aquater, 1989).

A resistivity survey using a central loop TEM was conducted by National Energy Authority (NEA) of Iceland in 1988. The survey showed a resistivity anomaly under Lava Lake and local rise in the groundwater above sea level which was interpreted to indicate the existence of a geothermal system below Lava Lake. The resistivity results based on the geological interpretation showed that increase of the saline groundwater table drops abruptly to sea level NE of the area occupied by six wells in the SW part of the Asal rift. Also, it showed that the groundwater table drops sharply to about the level of Lake Asal in a narrow zone perpendicular to the rift, west of the Lake Lava (Árnason et al., 1988).

Additional resistivity survey was conducted in 2007 and mainly comprised of MT soundings. The results of the resistivity survey highlighted the existence of very high resistivity near surface layer which is linked to dry rocks above water table. Shallow low resistivity layer extends to some hundreds of meters; it reflects the saturated rocks with conductive alteration minerals (smectite-zeolites) as confirmed by borehole data.

At greater depths, an increase in resistivity was observed and linked by well data to the resistive high temperature alteration minerals (chlorite-epidote) which are dominating in that layer. Another cause of resistivity high could be the reduction in porosity at the same depth. A low resistivity anomaly was observed in deeper structure below 5 km depth in Asal rift which is similar to other high temperature geothermal systems including Iceland. Though the cause of the deeper lying low resistivity is not yet well understood it has been proposed that it could be magmatic brine trapped below the ductile/brittle boundary at about 700°C (Árnason et al., 2010). The outcomes from different exploration methods applied were combined for the evaluation of geothermal resources and for compiling a conceptual model of the geothermal system in the Asal rift.

2.3.1 Geochemical survey

As discussed above, some of the geothermal surface manifestations in Asal rift are hot springs and fumaroles. For understanding the origin of those numerous springs and geothermal reservoir fluids, geochemical studies were conducted in the Asal rift area. The list of identified springs includes Manda springs located on the eastern side of Lake Asal, the Korili spring which is located in southern major fault system on lake side, the Manda springs and Wadi Kalou springs in the southern part of Lake Asal, Alifita and Eadkorar springs on the Northern side of the lake (Fouillac et al., 1983). The sample analysis has shown that the fluid compositions could be explained by the sea water-basalt interaction and evaporation. This has proven by the analysis of the correlations between major elements associated to the study of trace elements like lithium, strontium, bromine and barium, and strontium isotopes (San Juan et al., 1990).

The geochemical survey which has targeted samples collected from shallow aquifers from wells Assal 1, 2, 3, 4 and 6 and deep water samples from well Asal 3 as well as from samples of Lake Asal has concluded that all aquifers encountered are mainly recharged by sea water (Aquateer, 1989). Geothermal fluids within Asal rift originate from the mixing of sea water and high total dissolved solids continental water of meteoric origin. According to the equilibrium temperature calculation from all reactive gaseous species (H_2O , CO_2 , H_2 , CH_4 , CO , N_2 , NH_3), apart from H_2S ; the temperature was about 260°C which is compatible with the temperature measured in the reservoir. The waters in Lake Asal are composed of very concentrated sea water due to evaporation and its $CaSO_4$ content is changed due to precipitation. From the samples taken from deep geothermal fluids; there is no contact with Lake Asal waters and the Ca/Mg ratio is extremely different. However, the fluids sampled from well Asal 5 have shown that the water at the centre of the rift has a much higher salinity than water at the borders (Correia et al., 1985).

2.3.2 Gravity survey

A gravity survey was conducted in Asal rift with the purpose of studying the density changes within the Asal rift; which reflect the existence of sub-geological formation. The survey was conducted in 1979 and 1983 by BRGM in France (Demange and Puvilland, 1990). It was seen that there are relative gravity highs in the old rocks outside the rift and in North Ghoubbet. A positive anomaly was observed in the NE part of the inner rift and a relatively strong gravity high was observed under the south part of Lava Lake. Contrary, the SW part of the rift clear low gravity anomalies are seen which could be due to less dense hyaloclastite volcanic formations from late Pleistocene or early Holocene during the period when the rift was under the (sea) water (Demange and Puvilland, 1990).

The lithology of the wells drilled in SW part of the inner rift (A-3, A-4 and A-6) is in agreement with the gravity as hyaloclastite formations in the uppermost few hundred metres are found. This well field shows less density anomalies, towards the SE and NW, the impressive negative anomalies are observed; still confirming bigger buried hyaloclastite formations. On the other hand, gravity high is observed in

the inner rift and west of Lava Lake where the uppermost several hundred metres are predominantly subaerial basalts. It is probably linked to more dense subaerial lava flows and dense intrusions at depths in the volcanic centre.

2.3.3 Seismic survey

Seismic surveying in the area of interest is one method of monitoring volcanic activities. The Asal rift is known to be very active seismically and this has been proven by studies carried out by Lepine and Hirn (1992) and Doubre (2004). The installation of eight permanent telemetric seismic stations has facilitated the monitoring and the database was available at seismic observatory in Arta. The studies have shown that the earthquake activity is most intense in the NE part of the main rift. Less activity was observed in the main NE bordering faults but it was very intense below Lava Lake (Fiale) to the NW and in the NE part of the inner rift. It was noticed that there were no signs observed in the main faults of the rift; which could be due to very little fault movements since the rifting episode and latest eruption occurred.

The earthquakes observed below Lava Lake were quite shallow, predominantly between 0.5 and 4 km depth. In the NE part of the rift, they were relatively deeper at 1 km to 5 km depth and at some places these quakes were at two depth levels, one between 1 and 2 km and the other between 3 and 5 km. The earthquakes observed were not equally distributed; from the cumulative number of earthquakes in the Asal rift from 1979 to 2001, it is seen that they were mainly in the time intervals between 1980 and 1981, late 1987, 1991 to 1992 and from 1996 to the end of 2000. During the period from 1996 to 2000; the activity was almost constant, about 500 quakes per year. The magnitude of the quakes was relatively small and evaluated between 0.5 and 2 (Doubre, 2004).

The tomographic inversion of the seismic velocities which was performed in the volume of most intense seismicity has shown P-wave and S-wave velocities at different depths under the Asal rift. The low P-wave velocity indicates anomalously low compressibility while the high S-wave velocity indicates high shear strength of the rocks. S-waves cannot propagate through molten rocks and are attenuated and have lower velocity in partially molten rocks. In this analysis, the tomography has shown high S-wave velocity (V_s) down to 5 km depth under Lava Lake as a result of the absence of shallow magma chamber there. The low P-wave velocity (V_p) was interpreted to be reflecting rocks which are partially saturated by steam and or gas (Doubre, 2004).

The analysis based on the study of focal mechanism of the earthquakes in the Asal rift has revealed that the majority was double couple (strike-slip) earthquakes with variable faultplane solutions. But there were a small number of quakes which had non double couple solutions. They are attributed to sensible cracking or fracture collapse. The seismicity of Asal rift and its nature showed the existence of anomalous conditions under Lava Lake. The study has concluded by finding out different ways for the anomalous crust below the Lava Lake. The crust is accommodating the vast majority of the micro-earthquakes, it is presenting low V_p but high V_s and most of all non double couple quakes are found within the low P-wave velocity anomaly (Doubre, 2004).

2.3.4 Deep exploration drilling

To confirm the geothermal resources and to acquire the reservoir characteristics of geothermal in the Asal rift; deep exploration drilling was suggested where six deep wells were drilled. Based on the outcomes of geological mapping, geochemical analyses of hot springs and fumaroles, different geophysical methods as well as shallow gradient wells; the two first deep wells (Asal-1 and Asal-2) were sited at the external edge of the rift. Well testing technique of Asal-1 (temperature 258°C) drilled to a depth of 1146 m confirmed the existence of water dominated high-enthalpy geothermal reservoir. Although well Asal-2 (temperature 280°C) was dry it was generally hotter than well Asal-1. Due to high salinity problem which is characterizing the geothermal fluids of Asal-1, the geothermal drilling activities were moved to the Hanle area which was considered to have low salinity geothermal fluids. The results (temperature 70 and 120°C) of two deep wells (1600 and 2000 m) drilled in Hanle were not convincing; the field was classified to be a low temperature field. The target of exploiting geothermal

resources with the purpose of electrical power generation has pushed back the activities in the Asal field. Well Asal-3 was then sited and drilled to the East of Asal-1 at a distance of 4 m down to a depth of 1316 m with the objective of verifying the geothermal potential and the extent of the reservoir. Geothermal fluids in this well showed the same chemical characteristics and after only three months of discharging, the mass flow declined drastically due to scaling in the casing.

The next option was to locate the less saline part of the reservoir for further geothermal exploitation and development activities. Well Asal-4 was then sited 1250 m farther north of well Asal-3 and drilled to a depth of 2013 m while Asal-5 was sited 4750 m north of well Asal-3 at the edge of the rift and drilled down to 2105 m. The two wells did not give any information about the chemical geothermal fluids due to dryness but they were just highlighting the high temperature (temperature less than 350°C) characteristics of the Asal field. Asal-6 was sited in same area 300 m NW of Asal-3 and drilled to a depth of 1761 m; the well was less productive and presented similar chemical characteristics as Asal-3. Of the total of six wells drilled in the Asal geothermal field, Asal-5 was the deepest one (2105 m) but drilled to the shallowest hot reservoir (160°C) found at depth between 500 m and 550 m; the well intersected a cold zone (60°C) at a depth of 1200 m. The well which never discharged, reached a temperature of 333°C at its bottom (2105 m) (Aqater, 1989).

Borehole data from Asal-5 has provided detailed information of the geothermal reservoir in Asal geothermal field as shown in Figure 4. Further geological study (Saemundsson, 1988) and resistivity survey, using the TEM method (Árnason et al., 1988) were requested and carried out in 1988 by Icelandic scientists; these studies indicated that an upflow zone of geothermal fluid is located under Lava Lake. The results show that the Asal field is the most promising one for future geothermal exploitation and development for electrical power generation.

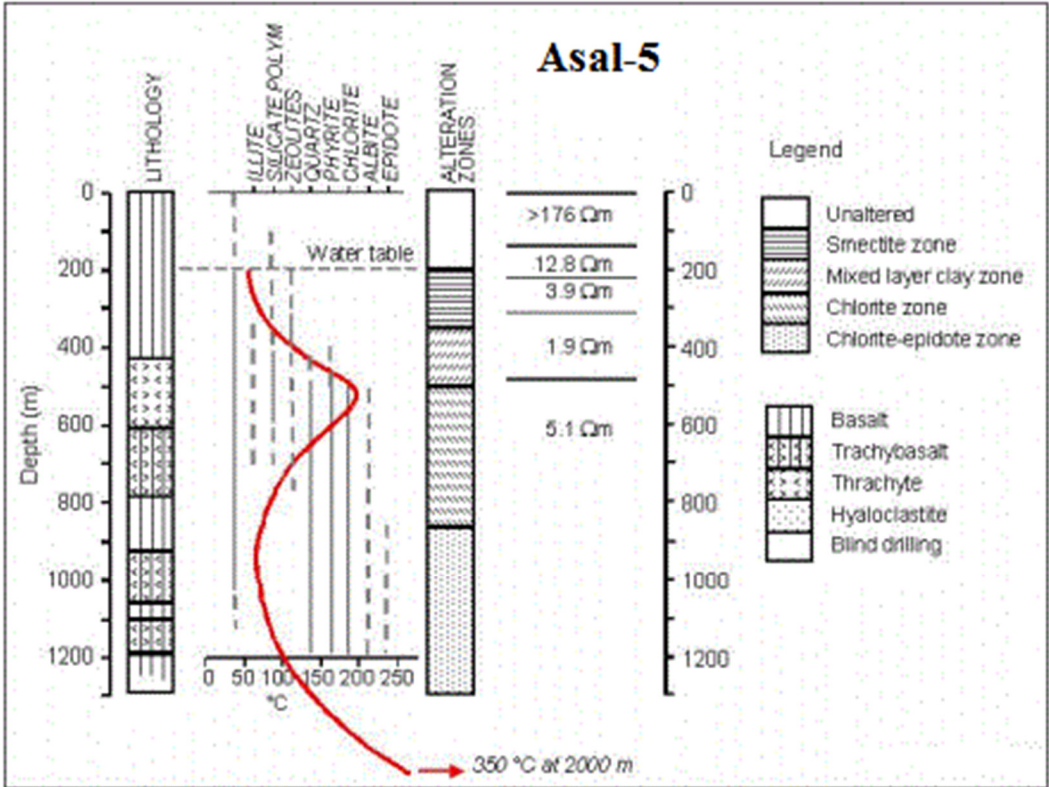


FIGURE 4: Lithology, temperature plot and alteration zones for well Asal-5 in Asal geothermal field (modified from Aqater, 1989)

3. APPLICATION OF EM RESISTIVITY METHODS FOR GEOTHERMAL EXPLORATION

For several decades, exploration for geothermal resources around the world has been based on different methods. Today, EM resistivity methods investigating the geothermal systems are the most powerful and reliable method. The main reason is that they are able to reveal directly the common properties characterising geothermal systems like permeability, porosity, salinity, temperature and the degree of hydrothermal alteration of the host rock (Hersir and Björnsson, 1991).

The information provided by resistivity measurements on the distribution of subsurface electrical resistivity is quite useful for understanding the geothermal reservoir. According to previous surveys; high temperature geothermal systems have a certain characteristic subsurface resistivity structure because of the hydrothermal alteration zones (Árnason et al., 2000). The existence of hot fluids in geothermal systems leads to the formation of a succession of hydrothermal alteration minerals controlled by temperature. The same information on subsurface electrical resistivity determines its conductivity level both laterally and vertically. EM resistivity methods are either a natural source method (e.g. MT) or a controlled source method (e.g. TEM). Compared to direct current (DC) resistivity methods, EM methods are more sensitive to conductive (less resistive) structures.

3.1 Resistivity of rocks

The measured material resistivity in the subsurface is basically controlled by the movement of charged ions in pore fluids and by conduction of secondary minerals. The electrical properties of the material are described by conductivity (reciprocal of resistivity). The electrical conductivity measures the ability of a material to conduct an electrical current. For rocks and minerals in the earth, this parameter spans several orders of magnitude (Figure 5). The variations in the observed conductivity values are not only related to the different electrical conductivities of various rock types and compositions, but also to the overall physical conditions of the media. From laboratory experiments carried out on dry granites, basalts and gabbros; it has been observed that there is a significant decrease in resistivity with an increase in temperature. It has been shown that a decrease in resistivity by two orders of magnitude for a temperature increases from 500 to 1000°C (Kariya and Shankland, 1983). Wet environment is more likely to be more conductive than a dry environment. This was proven by studies done on dry olivine which showed that implausibly high temperatures (>1500°C) would be required in the asthenosphere to explain the high observed conductivity (Karato, 1990). Another factor is the connectivity of the minerals. Strongly interconnected minerals will enhance the conductivity as compared to the same minerals with poor connectivity.

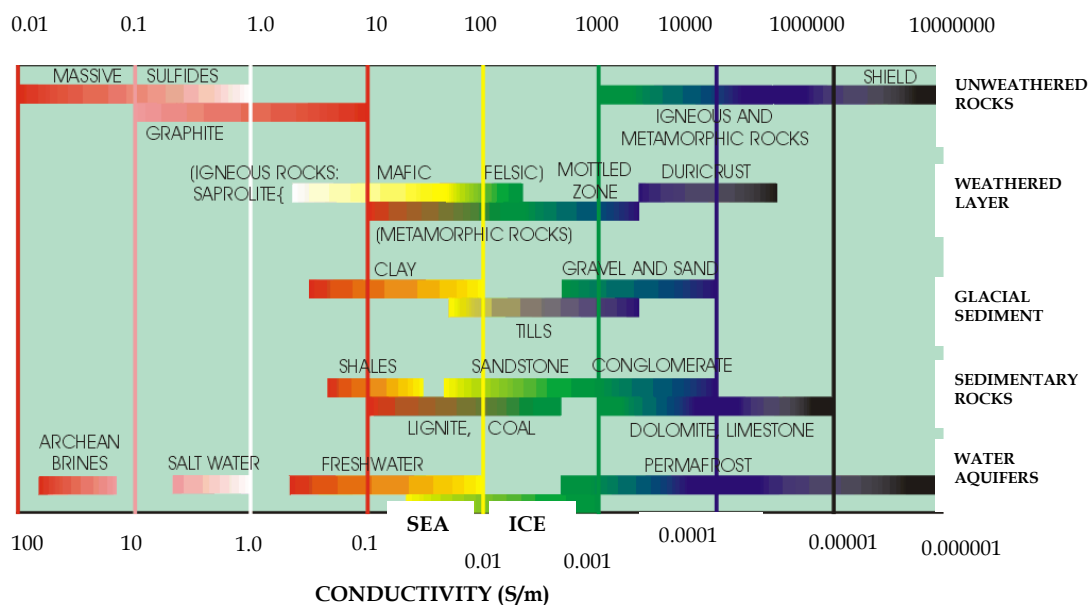


FIGURE 5: Typical average resistivity values for different rock types (modified, EOS 2007)

EM methods have the ability of defining geologic structures by relating electrical resistivity to the composition of rocks and other processes affecting them. However, most minerals forming the rock are electrical insulators. Though water is not alone a good conductor of electricity, saline ground waters generally contain dissolved compounds that greatly enhance electrical conductivity. Ground water movement is facilitated by interconnected pores and fractures, thus causing hydrothermal alteration of the host rocks.

The specific resistivity is defined through Ohm's law, $E = \rho J$; E [V/m] and J [A/m²]. It is defined as the ratio of the potential difference to the current I [A] across a material which has a cross-sectional area of 1 m² and is 1 m long

$$\rho = E/J = \Delta V / I \quad (3.1)$$

where ρ is the specific resistivity which depends on the material and is measured in Ωm . The reciprocal of resistivity is conductivity ($1/\rho = \sigma$) [Siemens/m] or [S/m].

Figure 5 is a summary of the resistivity (conductivity) of various rock materials.

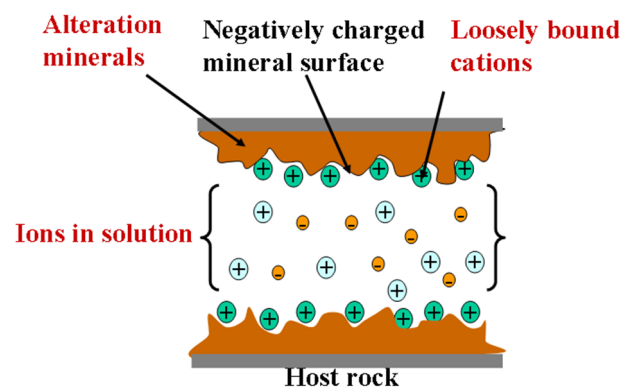
The main parameters controlling the electrical resistivity are the degree of water or brine saturation, temperature, porosity as well as electrical resistivity of the fluid filling the pore space (Palacky, 1987). When working with fractured zones, porosity and permeability are dominated by the fractures. The porosity level tends to decrease with depth which then reduces the effect of the pore fluid conditions. Consequently, the resistivity is increasing, countering to some extent the effect of higher salinity that is commonly inferred to lie in the deeper parts within the systems. In the pores, the salinity is high thus controlling the electrical resistivity.

Archie's law (1942) implies that for a given pore fluid the lower the porosity the larger is the bulk resistivity. The law expresses the influence of the water on the resistivity of a rock or sediment by the following equation:

$$\rho_o = A\rho_f\varphi^{-m} \quad (3.2)$$

where ρ_o is the bulk resistivity, ρ_f is the resistivity of the pore fluid and φ is the porosity. The term m is the factor which depends on the degree of interconnectivity of the pore fluids and ranges between 1.5 and 2. In Archie's law, higher values of m reflect a weak bond and low permeability fluid distribution. The term A is representing surface area and depends on pore geometry.

This law doesn't take into consideration the conducting mineral grains like a clay. According to the same Archie's law, when conducting grains are electrically connected; it will lower the bulk resistivity of the rock from what is predicted by the law.



The same applies also to the case of clay; the bulk conductivity could be resulted from conducting clay minerals instead of pore water.

In terms of mineral electrical conduction mechanisms; we observe mineral conduction which is negligible in most cases, pore fluid conduction where the conduction is controlled by dissolved ions in the pore fluid and surface conduction where the conduction is handled by absorbed ions on the pore surface (Figure 6). At the high temperatures close to solidus of the rock, the conductivity of the rock matrix becomes dominant and follows the Arrhenius formula:

FIGURE 6: Sketch showing the main conduction mechanisms (Hersir and Árnason, 2010)

$$\sigma_m(T) = \sigma_0 e^{-E/kT} \quad (3.3)$$

where σ_m is the matrix conductivity, σ_0 is the conductivity at infinite temperature, E is the activation energy (eV), k is the Boltzmann constant (eV/°K) and T is the temperature in °K (see e.g. Flóvenz et al., 2012).

The measurements carried out in laboratory on basalts and related material over the temperature range 400-900°C provided typical values of 0.80 for E and 300 for σ_m . It indicates that the matrix resistivity of basaltic rock is the order of 1000 Ωm at 400°C and decreases to 10 Ωm at 800°C. At higher temperature, partial melt will still increase the conductivity. At great depth in the geothermal system, we can expect high temperature exceeding 400°C which will explain the impact of the increase on the overall conductivity.

3.1.1 Interpretation of resistivity anomaly in geothermal system

A resistivity survey in geothermal area is one of the most useful geophysical tools for exploring and delineating geothermal resources. The main common factors behind the fluctuations of resistivity in rocks are salinity, water content, temperature of the fluid and the type of hydrothermal alteration of the rocks due to geothermal activity. Naturally, the dry rocks conduct more poorly the electrical currents compare to water saturated rocks and the conductivity increases with increasing temperature up to about 300°C (Violay et al., 2012).

We can distinguish geothermal systems from other surrounding systems by the fact that electrical conductivity (resistivity) of certain clay minerals like phyllosilicates (smectite) which are found in fractures in the rocks and is strongly dependent on temperature. The electrical resistivity of rocks is only weakly influenced by the salinity of the fluid, unless the salinity is very high and approaches that of seawater (Flóvenz et al., 2005).

In high temperature geothermal systems dominated by basaltic or where the host rocks are volcanic; the resistivity surveys are mostly revealing similar resistivity structure which correlates to the distribution of alteration mineralogy. A conductive cap (low resistivity) is observed on the outer and upper margins of the reservoir, and it is underlain by a more resistive core. To understand this resistivity structure; a thorough comparison with borehole data is necessary and has revealed a consistent correlation to the zones of dominant alteration minerals. The conductive cap coincides with the smectite-zeolite zone and the transition to the more resistive (less conductive) core occurs within the mixed layer clay zone. Chlorite and epidote are found to be the dominating alteration minerals in the resistive core zone. Temperature is the main factor influencing the alteration mineralogy. Consequently, if the alteration is in equilibrium with the present formation temperature; the resistivity structure can be interpreted in terms of temperature. The low resistivity cap within upper boundary is found where the temperature is in range of 50-100°C. The transition to the resistive core appears within temperature range of 230-250°C (Árnason et al., 2000) as seen in Figure 7.

Resistivity reflects hydrothermal alteration caused by heating of the rocks and reflects the highest temperature experienced by the same system in the recent time or the past. An exception is for a young system being heated up and the alteration is lagging behind and still not in equilibrium with the temperature. Hence, resistivity measurements reveal the alteration but do not indicate clearly if cooling has occurred after the alteration was formed as the resistivity profile expresses only the alteration in the formation which is irrespective of any later cooling of the system under examination. When there is equilibrium between the present temperature and alteration; resistivity reflects temperature. During the cooling the alteration may persist and the resistivity will reflect the temperature at which the alteration was formed. Therefore, the conclusion whether resistivity or the alteration indicates the present temperature of the system can only taken from an exploration drilling.

Taking an example of Krafla high temperature geothermal area, in the volcanic zone in north of Iceland; resistivity measurements (MT soundings) have been conducted and revealed that in most places deep-seated low resistivity at depths between 10 and 15 km. The same low resistivity layer (less than 10 Ωm) extends up to shallow depths of 2 to 3 km under the high temperature area (Mortensen et al., 2009). As the low resistivity layer is thought to reflect very high temperatures, it is interpreted as providing

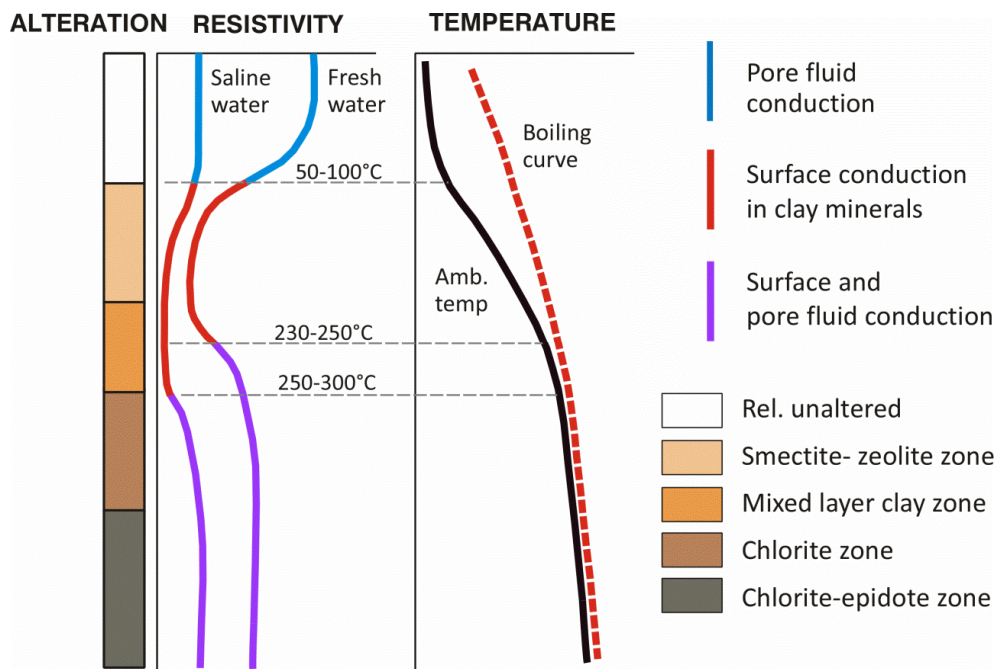


FIGURE 7: The general resistivity structure and alteration of the basaltic crust summarized. The depth scale is arbitrary (Flóvenz et al., 2012; modified from Flóvenz et al., 2005)

information about upwelling of heat into the geothermal system. The same idea is supported by TEM and MT measurements at Uppþyppingar in north Iceland; plume where a low resistivity anomaly in limited areas beneath the deep seated low resistivity layer is associated with active up flow of hot material (Vilhjálmsson et al., 2008).

3.2 Diverse methods for resistivity measurements

In geosciences, resistivity measurements are common not only in geothermal but also in oil and gas industry, ground water and mineral exploration. Depending on the methods, various parameters can be measured in geophysical exploration. In general, geophysical methods in geothermal exploration can be divided in two categories: direct methods (thermal, electrical or resistivity methods and Self Potential (SP) methods) and indirect or structural methods (magnetics, gravity and active and passive seismic methods) (Hersir and Björnsson, 1991; Manzella, 2007).

The direct methods give information on parameters that are influenced by the geothermal activity, while the structural methods give information on geological parameters which may reveal structures or geological bodies that are important for the understanding of the geothermal system. It is advisable to combine different methods for gathering detailed information rather than relying on the results of measurements of a single parameter. Resistivity or electrical methods are the most important geophysical method in surface exploration of geothermal areas, and as such the main method used in delineating geothermal resources and production fields. The parameters of interest are the electrical resistivity of the rocks which correlates with salinity, temperature, porosity and mineral alteration which are key parameters for the understanding of the geothermal systems.

DC (Direct current) methods: An electrical current is injected into the earth through a pair of electrodes and the resulting potential difference is measured between another pair of electrodes at the surface. Several variations of the direct current resistivity method have been used for decades, but the most widely used one in geothermal exploration is the Schlumberger array. Distinction is made between a resistivity sounding and profiling, aimed at measuring resistivity changes with depth and lateral variations, respectively.

The following DC configurations have been used in geothermal exploration: *Schlumberger sounding*, which has been widely used for a long time and is still the most popular one. The electrodes are on a line, and the setup is mirrored around the centre. The pair of potential electrodes is kept close to the centre, while the pair of current electrodes is gradually moved away from the centre, for the current to probe deeper and deeper into the earth. Another common configuration is the *Wenner array* where four collinear electrodes are equally spaced. The outer two are the current electrodes and the inner two the potential ones. All electrodes spacing is expanded along the line about the midpoint while the equal spacing between the electrodes is maintained.

Dipole soundings or profiling; here various arrays exist, many used quite extensively in the 1970s and into the 1980s.

Head-on profiling is a successful method for locating near-surface vertical fractures or faults. It is really a variant of the Schlumberger profiling method with a third current electrode located far away at a right angle to the profile line (see e.g. Flóvenz, 1984).

SP (Self Potential): This is another natural source electrical method and is a low-cost surveying technique. It has been applied in many geothermal areas. However, the anomalies are hard to interpret.

Electromagnetic methods: Both natural source electromagnetic methods like MT and controlled source electromagnetic methods like TEM are widely used. In the *MT method*, natural time variations in the earth's magnetic field induce currents in the earth, and the electrical field induced is measured at the surface. This is a powerful method for determining resistivity distribution within the earth down to depths of several tens or even hundreds of kilometres. On the other hand, in the *TEM method* an artificial source is used to generate the electromagnetic field (Árnason, 1989). Both resistivity methods are discussed here.

4. MAGNETOTELLURIC (MT) METHOD

4.1 Concepts of MT

The magnetotellurics (MT) is a passive electromagnetic (EM) exploration method initiated by Tikhonov (1950) and Cagniard (1953). It is based on measuring the orthogonal components of the electric and magnetic field at the Earth's surface. The technique images the electrical properties of the Earth's subsurface. It uses the energy from the natural source of external origin which is categorized as the primary electromagnetic field. When reaching the Earth's surface, part of the energy goes back due to the reflection and the other part penetrates into the Earth. The Earth that acts in this case as a good conductor allows a flow of the telluric currents that are induced in turn to produce a secondary magnetic field.

The electromagnetic fields are measured simultaneously; time variations of the magnetic field, $H(t)$ and the induced electric field, $E(t)$. The electrical conductivity structure of the underlying material can be determined from the relationship between the orthogonal components of the measured electric and magnetic field variations (Figure 8).

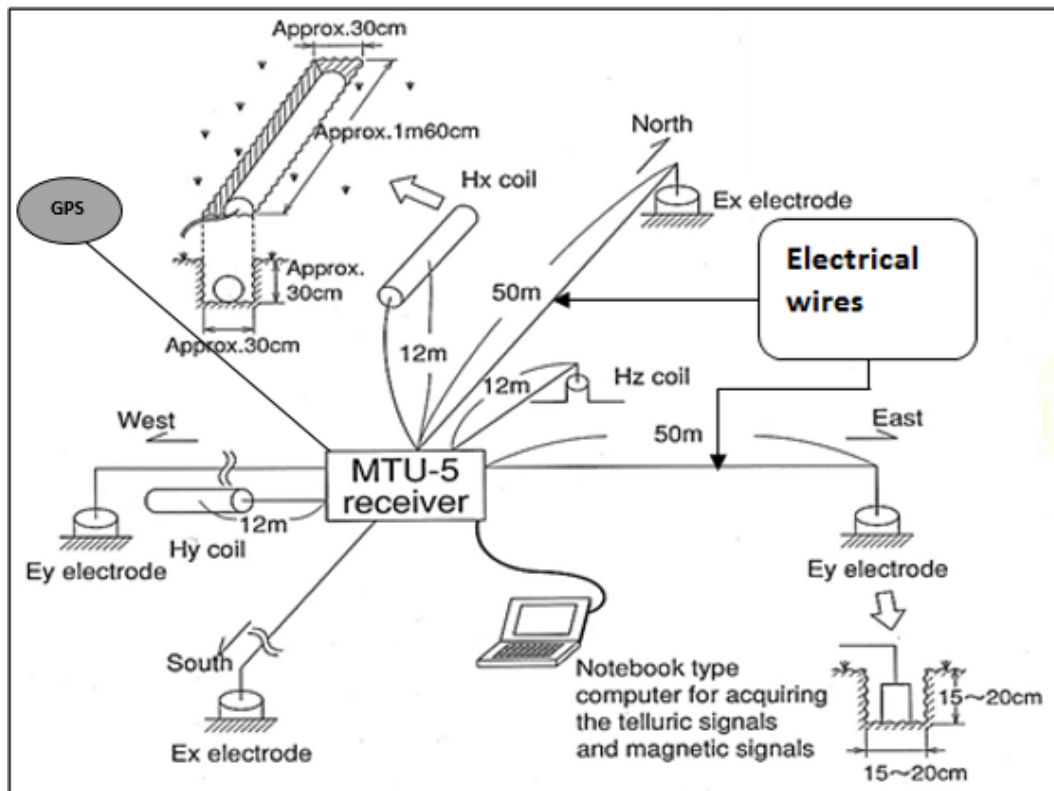


FIGURE 8: Illustration of MT set up for data acquisition: Electrodes for measuring the electric field, coils for the magnetic field; acquisition unit for digital recording and GPS for synchronizing data (modified from West JEC, 2012)

Maxwell's equations

For better understanding how the electromagnetic fields serve to study the structure of the Earth and determine its electric and magnetic behaviour, Maxwell's equations are applied. These equations relate the electric and magnetic fields.

The following set of the four Maxwell's equations is used to describe the EM field in a conductive medium.

$$\nabla \times E = -\frac{\partial B}{\partial t} \quad \text{Faraday's law} \quad (4.1)$$

$$\nabla \times H = J + \frac{\partial D}{\partial t} \quad \text{Ampere's law} \quad (4.2)$$

$$\nabla \cdot D = \eta \quad \text{Gauss's law for electric field} \quad (4.3)$$

$$\nabla \cdot B = 0 \quad \text{Gauss's law for magnetic field} \quad (4.4)$$

where E (V/m) and H (A/m) are the electric and magnetic field, respectively, B (T) is the magnetic induction. D (C/m²) is the electric displacement, $\frac{\partial D}{\partial t}$ (C/m²s) is the displacement current density and η (C/m³) is the electric charge density owing to free charges. J (A/m²) is the current density.

Maxwell's equations can also be related through their constitutive relationships, for a linear and isotropic medium.

$$J = \sigma E, D = \epsilon E \text{ and } B = \mu H \quad (4.5)$$

where σ , ϵ and μ describe intrinsic properties of the materials through which the electromagnetic waves propagate; μ (H/m) is the magnetic permeability and $\mu = \mu_0 \mu_r$ where $\mu_0 = 4\pi \cdot 10^{-7}$ (H/m). σ (S/m) is the electric conductivity (its reciprocal being the electrical resistivity $\rho = 1/\sigma$ (Ωm)) and ϵ (F/m) is the dielectric permittivity; $\epsilon = \epsilon_0 \epsilon_r$ where $\epsilon_0 = 8.85 \cdot 10^{-12}$ (F/m).

In isotropic media, these magnitudes are scalar quantities but they must be expressed in a tensor form when they are in anisotropic materials.

Assuming that the variations in μ_r and ϵ_r are negligible compared to variations in the bulk conductivity, σ of rocks, or $\mu_r \approx 1$ and $\epsilon_r \approx 1$, and we have: $\mu = \mu_0$ and $\epsilon = \epsilon_0$.

The MT technique depends on the penetration of the EM energy into the Earth as proposed by Vozoff (1972). The two following assumptions are used and further discussed and explained in section 4.3.1:

- (1) The electrical conductivity is always much larger than the product of angular frequency and the dielectric permittivity i.e. $\sigma \gg \omega \epsilon$
- (2) Due to the large resistivity contrast at the air–Earth interface, an incoming natural EM wave propagates essentially vertically into the Earth.

4.2 Source field of MT signals and the depth of penetration

The naturally generated variations in the Earth's magnetic field are the source for MT, providing a wide and continuous spectrum of EM field waves that induce currents within the Earth. These induction currents contribute to the measured fields on the surface and hold information about the subsurface conductivity structure ranging from a few tens of meters to tens of kilometers depth (Vozoff, 1972).

Two main sources are commonly known to be the origin of MT signals (Naindu, 2012):

1. For lower frequencies (long wavelengths) less than 1 Hz or less than one cycle per second, the source of the signal originates from the interaction of solar wind with the Earth's magnetic field. As solar wind emits streams of ions, which travel into space and disturbs the Earth's ambient magnetic field and produces low frequency electromagnetic energy penetrating the Earth.
2. The high frequency signal, greater than 1 Hz or more than one cycle per second, is created by world wide thunderstorm activity, usually near equator. The energy created by these storms travels around the Earth in a wave guide between the Earth's surface and the ionosphere, with part of the energy penetrating into the Earth.

The above mentioned signal sources create time varying electromagnetic waves; their strength varies over the hours, days, weeks and even over the sunspot cycle. Since the mid-seventeen century, the sunspot cycle has been monitored; it observes that there is a regular cycle over 10 to 11 years. From the sunspot cycle over the past 60 years, the last minimum activity was estimated to be at around 2010 (Figure 9). Hence, the source spectrum was extremely weak which causes the acquisition of MT data to be relatively difficult, compared with the time around five years earlier where the signal was strong (Flóvenz et al., 2012).

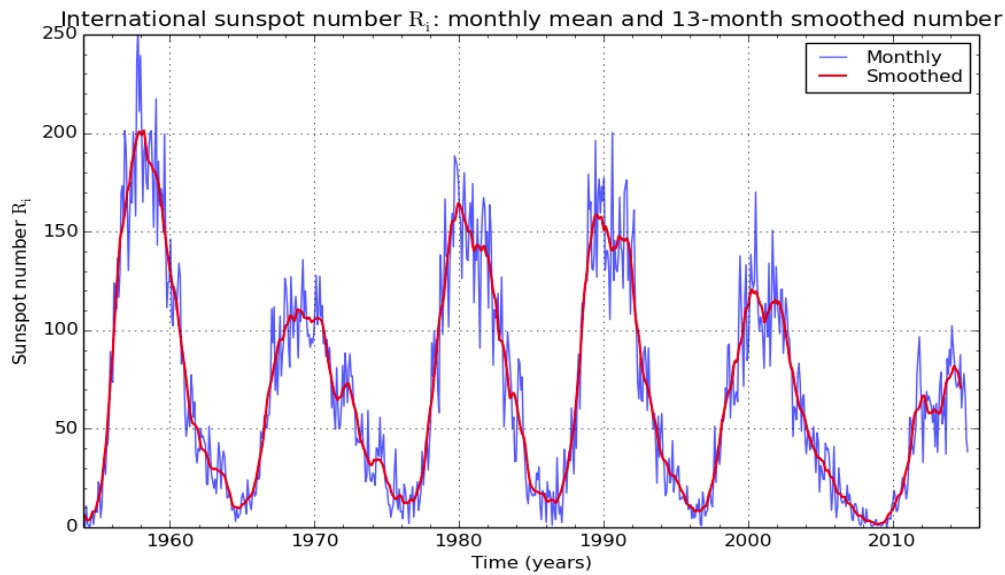


FIGURE 9: The average monthly sunspot number (blue) and 13-month smoothed monthly sunspot number (red) for the last five cycles (SILSO data/image, Royal Observatory of Belgium, 2015)

MT survey for the deeper lying subsurface structure, requires enough time (many hours) at each sounding in order to come up with good signal to ensure good quality data. This is due to the requirement of low frequencies (10^{-3} Hz or 1 cycle per 1000 s) to be able to image great depths. One sample of data needs 16 min (=1000 s) to be recorded; this requires reasonably several hours to record many samples (25-50) for a meaningful statistical average of data (Naidu, 2012).

Two serious problems in MT measurements are identified and should be taken into consideration in the processing of the data;

Static shift problem:

This is the distortion due to an electric field generated from boundary charges on surfacial inhomogeneities and persists throughout the entire MT recording range. The problem occurs particularly in volcanic areas where the effect due the resistivity heterogeneity in the vicinity of the measuring dipole is quite high comparatively to the sediment areas. The whole response of the earth is shifted downward or upward, thereby giving misleading resistivity as well as in depth values. The static shifts are manifested in the data as vertical, parallel shifts of apparent resistivity sounding curves on log-log scale. However, it does not affect the phase of the MT impedance tensor (Pellerin and Hohmann, 1990). Actually, this problem is corrected by using TEM in conjunction with MT collected in the same site. TEM sounding which doesn't rely on measurement of electric fields, is not affected by the same problem (Simpson and Bahr, 2005). There are two main reasons causing the static shift problem Árnason (2008):

- a) *Galvanic distortion:* Whereby the electric current flowing in the earth is encountering conductivity anomalies which affect its flow path. The type of anomalous conductivity determines how the current is altered. Currents are channeled into a higher conductivity anomaly but are deflected from a lower conductivity anomaly. Galvanic distortion is caused by charge distributions accumulated on the surface of shallow bodies. The last ones are producing anomalous electromagnetic field. The topography effects are attributed also to be the cause of current channelling or repelling.

It is found that the rough topography can produce static distortion where currents concentrate beneath depressions and disperse under peaks. This leads to electric field increase in valleys and reduction on hills due to galvanic effects. Therefore, MT fields and current density are higher in a valley and lower on a hill. This results to the upward or downward shift for the apparent resistivity curve which is known as static shift.

b) *Electric field or voltage distortion*: This is resulted to the vertical resistivity inhomogeneity; the electric field is higher in the resistive layer due to the slow flow of current and causes the increase of the voltage to occur within the same layer. When reaching geological material with high conductivity (low resistive layer), all layers below will be affected and moved upward. In different scenario, the layers move downwards due to the appearance of low conductivity (high resistivity layer) in place.

Dead band problem:

It occurs in the frequency band ranging between 0.5 and 5 Hz (2-0.2 s) for MT and for AMT, the dead band is appearing at range of 1-5 kHz. MT and AMT measurements in these frequency ranges usually suffer from poor data quality; resulting in inaccurate data for a certain depth interval. Noise due to wind is also typically highest in these frequency ranges, thus diminishing the signal to noise ratio (Figure 10). According to the EM principle; higher frequencies, greater than 1 Hz (short periods) are generated from thunderstorm activity near the Equator and are distributed as guided waves called spherics, between the ionosphere and the Earth to higher latitudes (Flóvenz et al., 2012). It is attributable to inductive source mechanisms, one effective below 1 Hz and the other above 1 Hz; this causes a reduction in MT data quality.

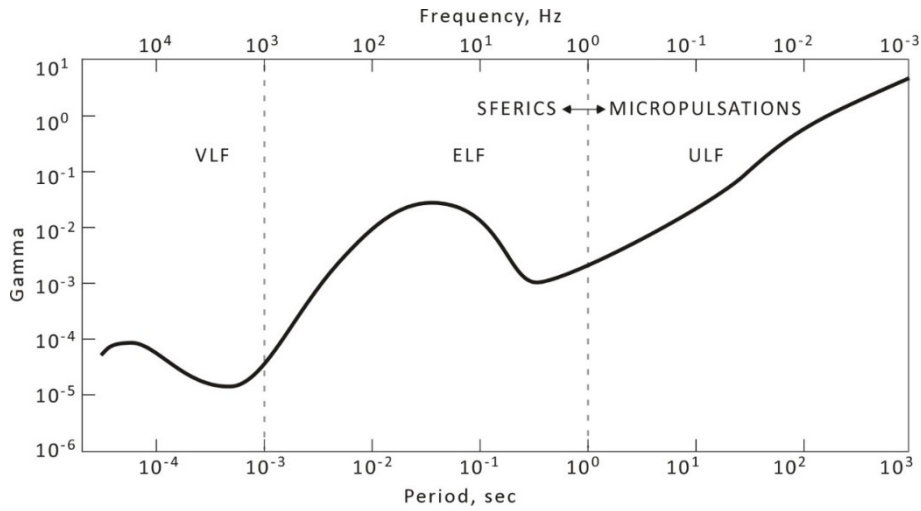


FIGURE 10: The mean amplitude of the natural magnetic field spectrum in gamma ($\gamma=nT$) as a function of the period (Flóvenz et al., 2012)

4.3 Electromagnetic waves in a conductive medium

4.3.1 Non-vertical incidence on conductive half-space

In homogeneous and isotropic half space, using the constitutive relationships in Equation 4.5 and assuming time dependence of $e^{-i\omega t}$. Therefore; Equations 4.1 and 4.2 may be rewritten as

$$\nabla \times E = i\omega\mu H \quad (4.6)$$

$$\nabla \times H = \sigma E - i\omega\epsilon E \quad (4.7)$$

The only conductive boundary is the horizontal surface, so only a vertical component of the electric field, E_z would lead to charge build up on the surface. In the MT sounding method, the EM source waves are considered to be plane waves. An EM wave of angular frequency ω and with an angle of incidence θ_i travels through the air and approaches the surface of the homogeneous Earth of conductivity σ . When the wave hits the surface it is both reflected back and refracted into the half space at an angle of refraction, θ_t . The relation between angles of incidence and the refracted waves is given by Snell's law as follows;

$$\frac{1}{v_0} \sin\theta_i = \frac{1}{v} \sin\theta_t \quad (4.8)$$

where

$$v_0 = \frac{1}{\sqrt{\epsilon_0 \mu_0}} = c \quad \text{and} \quad v = \frac{\omega}{|k|} = \sqrt{\frac{2\omega}{\mu_0 \sigma}} \quad (4.9)$$

v_0 is the velocity of an EM wave in the free air, the speed of light c ; v is the velocity of an EM wave in the homogeneous half space, ω is the angular frequency and k is the wave propagation constant.

Inserting the values, Equation 4.8 becomes

$$\sin\theta_t = \sin\theta_i \sqrt{\frac{2\epsilon_0 \omega}{\sigma}} \quad (4.10)$$

The frequency range for the MT method is 10^4 - 10^4 Hz and the conductivity of the subsurface rocks ranges from 10^3 - 10^4 S/m (10^{-3} - 10^4 Ω m). In the following discussion it is assumed that the magnetic permeability is equal to that of vacuum. The relative dielectric permittivity values of rocks are in range of 1-100, generally ~ 10 .

By using the upper limits of this range gives $\sqrt{\frac{2\omega \epsilon_r \epsilon_0}{\sigma}} < 10^{-6}$.

As $\sin\theta_i \leq 1$, the angle of the refracted wave in the homogeneous half space is close to zero, indicating that the wave travels close to the vertical for all angles of incidence. It can be assumed that the EM wave travels as a plane wave with a direction of travel vertically into the Earth. In a half space, the E_z component is always 0, leading to no surface charge build up. The electrical charge density η , is always zero within the half space and Equation 4.3 becomes:

$$\nabla \cdot D = 0 \quad (4.11)$$

Taking the curl of Equations 4.6 - 4.7 gives;

$$\nabla \times \nabla \times E = i\omega\mu\nabla \times H = i\omega\mu(\sigma - i\omega\epsilon)E \quad (4.12)$$

$$\nabla \times \nabla \times H = (\sigma - i\omega\epsilon)\nabla \times E = (\sigma - i\omega\epsilon)i\omega\mu H \quad (4.13)$$

Using the vector identity:

$$\nabla \times \nabla \times A = -\nabla^2 A + \nabla(\nabla \cdot A) \quad (4.14)$$

And the condition from Equation 4.1, Equation 4.12 becomes

$$\nabla^2 E + i\omega\mu(\sigma - i\omega\epsilon)E = 0 \quad (4.15)$$

Similarly, by using the condition from Equation 4.2, Equation 4.13 becomes;

$$\nabla^2 H + i\omega\mu(\sigma - i\omega\epsilon)H = 0 \quad (4.16)$$

Both of Equations 4.15 and 4.16 are second order differential equations with dependence on ω and wave propagation constant of $k^2 = \omega\mu(i\sigma + \omega\epsilon)$. Using the same extreme values for the conductivity σ and the angular frequency ω as before, it holds that $(\omega\epsilon)_{max} = 2\pi f \epsilon_r \epsilon_0 \approx 5 \cdot 10^{-5}$.

It holds that $\sigma \gg \omega\epsilon$ and therefore neglecting the non-diffusive part of the EM wave is justified. This simplification is referred to as the quasi static approximation and reduces the wave propagation constant to $k^2 = i\omega\mu\sigma$. In this approximation; Equations 4.15 and 4.16 are reduced to:

$$\nabla^2 E + i\omega\mu\sigma E = 0 \quad (4.17)$$

$$\nabla^2 H + i\omega\mu\sigma H = 0 \quad (4.18)$$

4 3.2 The EM in horizontally layered Earth

An EM plane wave travels vertically in horizontally layered Earth successively from one layer to another. The current flow is excited while passing through the layers and produces EM fields. The produced fields are depending on the conductivity of the layer which results to the derivation of conductivity information.

Assume a layered Earth of N layers with uniform conductivity σ_i , thickness d_i and magnetic permeability as that of free air, μ_0 . Being half space, the Nth layer is considered to have infinite thickness. Equations 4.17 and 4.18; known as Helmholtz equations are describing the propagation of the EM wave in the Earth.

In Cartesian coordinate system; x, y and z axes are positive oriented in North, East and Down, respectively. By writing out the ∇^2 operator, the equations become:

$$\frac{\partial^2 E}{\partial x^2} + \frac{\partial^2 E}{\partial y^2} + \frac{\partial^2 E}{\partial z^2} + i\omega\mu_0\sigma_i E = 0 \quad (4.19)$$

$$\frac{\partial^2 H}{\partial x^2} + \frac{\partial^2 H}{\partial y^2} + \frac{\partial^2 H}{\partial z^2} + i\omega\mu_0\sigma_i H = 0 \quad (4.20)$$

The wave propagates only downwards while the variations in x and y are zero; therefore the Equations 4.19 and 4.20 are simplified as:

$$\frac{\partial^2 E}{\partial z^2} + i\omega\mu_0\sigma_i E = 0 \quad (4.21)$$

$$\frac{\partial^2 H}{\partial z^2} + i\omega\mu_0\sigma_i H = 0 \quad (4.22)$$

where the propagation constant for the i^{th} layer is $k_i^2 = i\omega\mu_0\sigma_i$, the Earth surface is at $z_0 = 0$ and the depth to the top of the i^{th} layer is z_i . Equation (4.21) in the i^{th} layer has the following harmonic solutions;

$$E_x(z, \omega) = A_x e^{-ik_i z} + B_x e^{ik_i z} \quad (4.23)$$

$$E_y(z, \omega) = A_y e^{-ik_i z} + B_y e^{ik_i z} \quad (4.24)$$

In Equations 4.23 and 4.24, the first terms describe electric fields that increase in amplitude with depth (upwards) while the second ones describe fields that are decreasing with depth (downwards). The constants A and B are arbitrary and are determined using boundary conditions.

By writing out the $\nabla \times$ operator in Equation 4.6 in scalar form and remembering that the derivatives with respect to x and y are zero:

$$H_x(z, \omega) = -\frac{1}{i\omega\mu} \frac{\partial E_y(z)}{\partial z}, \quad H_y(z, \omega) = \frac{1}{i\omega\mu} \frac{\partial E_x(z)}{\partial z}, \quad H_z(z, \omega) = 0 \quad (4.25)$$

By substituting the solutions in Equations 4.23 and 4.24 into Equation 4.25 gives

$$H_x(z, \omega) = \frac{k_i}{\omega\mu_0} (A_y e^{-ik_i z} - B_y e^{ik_i z}) \quad (4.26)$$

$$H_y(z, \omega) = -\frac{k_i}{\omega\mu_0} (A_x e^{-ik_i z} - B_x e^{ik_i z}) \quad (4.27)$$

Taking the ratio of the electric and magnetic fields, yields the Tikhonov-Cagniard wave impedance as:

$$Z_{xy} = \frac{E_x}{H_y} \quad ; \quad Z_{yx} = \frac{E_y}{H_x} \quad (4.28)$$

Substituting Equations 4.24, 4.25, 4.26 and 4.27 into Equation 4.28 gives:

$$Z_{xy} = \frac{\omega\mu_0 A_x e^{-ik_i z} + B_x e^{ik_i z}}{k_i A_x e^{-ik_i z} - B_x e^{ik_i z}} \quad (4.29)$$

$$Z_{yx} = \frac{\omega\mu_0 A_y e^{-ik_i z} + B_y e^{ik_i z}}{k_i A_y e^{-ik_i z} - B_y e^{ik_i z}} \quad (4.30)$$

where A_x , A_y , B_x and B_y are arbitrary constants that are dependent on layer properties and they are constant in the horizontal directions.

Therefore, $A_x = A_y = A_i$ and $B_x = B_y = B_i$

The impedance should be constant at boundaries between layers. The impedance at the top of i^{th} layer is following:

$$\hat{Z}_{i-1} = Q \frac{A_i e^{ik_i z_{i-1}} + B_i e^{ik_i z_{i-1}}}{A_i e^{ik_i z_{i-1}} - B_i e^{ik_i z_{i-1}}} \quad (4.31)$$

where $Q = \frac{\omega\mu_0}{k_i}$ is the characteristic impedance of the i^{th} layer, A_i , B_i are arbitrary constants for the i^{th} layer and z_{i-1} is the depth to the top of the layer.

On other hand, the impedance at bottom of i^{th} layer is given as:

$$\hat{Z}_i = Q \frac{A_i e^{-ik_i z_i} + B_i e^{ik_i z_i}}{A_i e^{-ik_i z_i} - B_i e^{ik_i z_i}} \quad (4.32)$$

where z_i is the depth to the bottom of the i^{th} layer.

Dividing the denominator and the numerator of Equation 4.31 by $(A_i B_i)^{\frac{1}{2}}$ and rearranging gives:

$$\hat{Z}_i = Q \frac{\left(\frac{A_i}{B_i}\right)^{\frac{1}{2}} e^{-ik_i z_i} + \left(\frac{B_i}{A_i}\right)^{\frac{1}{2}} e^{ik_i z_i}}{\left(\frac{A_i}{B_i}\right)^{\frac{1}{2}} e^{-ik_i z_i} - \left(\frac{B_i}{A_i}\right)^{\frac{1}{2}} e^{ik_i z_i}} \rightarrow \left(\frac{A_i}{B_i}\right)^{\frac{1}{2}} = \frac{\left(\frac{B_i}{A_i}\right)^{\frac{1}{2}} (\hat{Z}_i e^{ik_i z_i} + Q e^{ik_i z_i})}{(\hat{Z}_i e^{-ik_i z_i} - Q e^{-ik_i z_i})} \quad (4.33)$$

Applying the same methodology, Equation 4.32 becomes:

$$\hat{Z}_{i-1} = Q \frac{\left(\frac{A_i}{B_i}\right)^{\frac{1}{2}} e^{-ik_i z_{i-1}} + \left(\frac{B_i}{A_i}\right)^{\frac{1}{2}} e^{ik_i z_{i-1}}}{\left(\frac{A_i}{B_i}\right)^{\frac{1}{2}} e^{-ik_i z_{i-1}} - \left(\frac{B_i}{A_i}\right)^{\frac{1}{2}} e^{ik_i z_{i-1}}} \quad (4.34)$$

The substitution by Equation 4.33 into Equation 4.25 will yield an equation without any constants A_i and B_i as:

$$\hat{Z}_{i-1} = Q \frac{\hat{Z}_i + Q \tanh(ik_i d_i)}{Q + \hat{Z}_i \tanh(ik_i d_i)} \quad (4.35)$$

where $d_i = z_i - z_{i-1}$ is the thickness of the i^{th} layer.

The previous Equation 4.45 is known as recursion formula and is used for calculation of impedance at the top of the i^{th} layer given the impedance of $(i + 1)^{th}$ layer. The impedance at the top of the N^{th} layer is the same as that of half space. At the bottom, there are no waves travelling upwards, therefore the fields are given as:

$$E_x = A_N e^{ik_N z} \quad (4.36)$$

$$H_y = \frac{k_N}{\omega\mu_0} (A_N e^{ik_N z}) \quad (4.37)$$

Then, calculating the impedance for the bottom half space gives:

$$Z_N = \frac{E_x(z)}{H_y(z)} = -\frac{E_y(z)}{H_x(z)} = \frac{\omega\mu_0}{k_N} \quad (4.38)$$

Since $z_{N-1} \leq z \leq \infty$; this will yield the impedance at the boundary between the N^{th} and $(N-1)^{th}$ layer. The recursive Equation 4.35 could provide the impedance at each layer boundary from the bottom up once solved. The impedance at the surface of the Earth will be provided by solving the equation $N-1$ times.

4.3.3 Conductivity in a homogeneous medium

Conductivity σ is assumed to be isotropic and the impedance is calculated by using Equation 4.38. By substituting the wave propagation constant $k = \sqrt{i}\sqrt{\omega\mu_0\sigma} = \frac{1+i}{\sqrt{2}}\sqrt{\omega\mu_0\sigma}$ in Equation 4.38 gives the impedance as:

$$Z = \frac{\omega\mu_0}{\sqrt{\omega\mu_0\sigma}} \frac{\sqrt{2}}{1+i} = \sqrt{\frac{\omega\mu_0}{\sigma}} \frac{\sqrt{2}}{2} (1-i) = \sqrt{\frac{\omega\mu_0}{\sigma}} e^{-i\pi/4} \quad (4.39)$$

The phase angle between the E and H fields is $\pi/4$ or 45° , the E field lags behind the H field. Considering the absolute value and squaring the impedance yields:

$$\left| \frac{E}{H_\perp} \right|^2 = \left| \frac{\omega\mu_0}{\sigma} \right|^2 = \frac{\omega\mu_0}{\sigma} \quad \Rightarrow \quad \rho = \frac{1}{\sigma} = \frac{1}{\omega\mu_0} \left| \frac{E(\omega)}{H_\perp(\omega)} \right|^2 = \frac{1}{\omega\mu_0} |Z|^2 \quad (4.40)$$

where \perp is the orthogonal field. The resistivity derived in Equation 4.40 is the true resistivity of the half-space. The skin depth of an EM wave is the depth where the amplitude of the field has decreased to e^{-1} of its amplitude at the surface. It is the reciprocal of the real part of the wave propagation constant and is calculated as:

$$\delta(\omega) = \frac{1}{\Re(k)} = \sqrt{\frac{2\rho}{\omega\mu_0}} \quad (4.41)$$

In the standard units, Equation 4.41 is reduced to:

$$\delta(f) \approx 503 \sqrt{\frac{\rho}{f}} \quad [m] \quad (4.42)$$

where δ is the skin depth, f is the frequency and ρ is the apparent resistivity

4.3.4 MT transfer functions

Magnetotelluric transfer functions or MT responses are functions that are relating the registered electromagnetic field components at given frequencies. The functions do not depend on the electromagnetic source fields which can be taken as plane waves; they depend only on the electrical properties of the material and frequency.

For this reason, they are able to characterize the resistivity distribution of the underlying material according to the measured frequency.

Geomagnetic transfer functions

The geomagnetic transfer function is a complex vector that reveals the relationship between the horizontal and vertical components of the magnetic field. The vertical component is generated by lateral conductivity gradients in the earth. This function is also known as the tipper vector or Tipper \mathcal{T} and is dimensionless.

$$H_z(\omega) = \mathcal{T}_{zx}H_x(\omega) + \mathcal{T}_{zy}H_y(\omega) \quad (4.43)$$

For 1-D or a homogeneous Earth, the Tipper is zero ($\mathcal{T}_{zx} = \mathcal{T}_{zy} = 0$) due the absence of an induced vertical magnetic field, H_z .

On the hand, there is an induced vertical magnetic (H_z) field close to a vertical boundary between low and high conductivity structures (for example at the boundary between ocean and land). For 2-D Earth, the coordinate system can be rotated so that the x-axis is in the strike direction which is called T-strike; $\mathcal{T}_{zx} = 0$ but $\mathcal{T}_{zy} \neq 0$. This is done by minimizing $|\mathcal{T}_{zx}|$. The tipper vector can be decomposed into two real vectors in the horizontal xy plane; they are commonly called induction arrows. The induction arrows have the role of inferring the presence of lateral conductivity variations. Two convention representations of the real induction arrows exist: the reversed (Parkinson convention, Parkinson, 1959) and the non-reversed (Schmucker or Wiese convention). In the last one, the vectors point away from lateral increase in electrical conductivity (Wiese, 1962). The arrows have a real (in phase) and quadrature (out of phase) part.

The length of the real (M_r) and imaginary (M_q) arrows are given as:

$$\begin{aligned} M_r &= (\Re \mathcal{T}_{zx}^2 + \Re \mathcal{T}_{zy}^2)^{1/2} \\ M_q &= (\Im \mathcal{T}_{zx}^2 + \Im \mathcal{T}_{zy}^2)^{1/2} \end{aligned} \quad (4.44)$$

where \Re and \Im are the real and imaginary parts of the tipper, respectively.

The magnitude of the induction arrows depends on both the proximity to the conductor and the conductivity contrast. The bigger the contrast the longer the arrows and the closer the conductor the longer is the arrow.

The directions of the arrows are similarly determined as:

$$\begin{aligned} \theta_r &= \tan^{-1} \left(\frac{\Re \mathcal{T}_{zy}}{\Re \mathcal{T}_{zx}} \right) \\ \theta_q &= \tan^{-1} \left(\frac{\Im \mathcal{T}_{zy}}{\Im \mathcal{T}_{zx}} \right) \end{aligned} \quad (4.45)$$

θ_r and θ_q are clockwise positive from the x-axis (usually geomagnetic North) along which the coherency between vertical and the horizontal magnetic field is at its maximum.

For 2-D Earth; the direction of the induction arrow is perpendicular to the true orientation of the regional strike. On other hand, for 3-D Earth, the direction varies and always points away from the conductive body.

MT impedance tensor

The orthogonal electrical and magnetic fields that are collected at each sounding are related by a complex impedance tensor \hat{Z} . This relation can be expressed as: $E(\omega) = Z(\omega)H(\omega)$ and written in matrix form as:

$$\begin{bmatrix} E_x(\omega) \\ E_y(\omega) \end{bmatrix} = \begin{bmatrix} Z_{xx}(\omega) & Z_{xy}(\omega) \\ Z_{yx}(\omega) & Z_{yy}(\omega) \end{bmatrix} \begin{bmatrix} H_x(\omega) \\ H_y(\omega) \end{bmatrix} \quad (4.46)$$

The impedance depends on the frequency. The linear relationship of the fields can be expressed as:

$$E_x(\omega) = Z_{xx}(\omega)H_x(\omega) + Z_{xy}H_y(\omega) \quad (4.47)$$

$$E_y(\omega) = Z_{yx}(\omega)H_x(\omega) + Z_{yy}H_y(\omega) \quad (4.48)$$

i. One-dimensional (1-D) impedance tensor

The conductivity σ changes only with depth in 1-D layered earth (Figure 11). Therefore, the impedance tensor can written as:

$$Z_{1D} = \begin{pmatrix} 0 & Z_{xy} \\ -Z_{yx} & 0 \end{pmatrix} \quad (4.49)$$

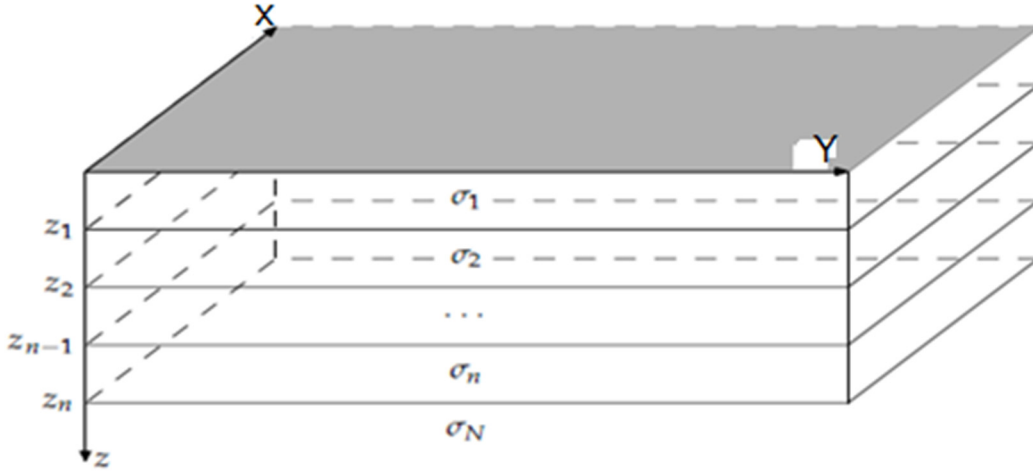


FIGURE 11: One-dimensional schematic model with σ varying in the z -direction only

The apparent resistivity ρ_a for layered earth is given by

$$\rho_a(\omega) = \frac{1}{\mu_0 \omega} |Z|^2 \quad (4.50)$$

The phase angle of the complex impedance tensor is defined as:

$$\phi_a(\omega) = \tan^{-1} \left(\frac{\text{Im}Z}{\text{Re}Z} \right) \quad (4.51)$$

Thus, in both Equations 4.50 and 4.51; the apparent resistivity and phase depend on the angular frequency $\omega=2\pi f$ where f is the frequency.

ii. Two-dimensional (2-D) impedance tensor

In the case of 2-D earth, the conductivity σ changes with depth and in one horizontal direction (Figure 12). The resistivity is constant in the other horizontal direction which is commonly known as the electromagnetic strike or geo-electrical strike direction.

The diagonal elements of the impedance tensor Z_{xx} and Z_{yy} are equal in magnitude but opposite in sign, on the other hand the off-diagonal elements Z_{xy} and Z_{yx} are not the same.

Therefore, the impedance tensor for 2-D is written as

$$Z_{2D} = \begin{pmatrix} Z_{xx} & Z_{xy} \\ Z_{yx} & -Z_{yy} \end{pmatrix} \quad (4.52)$$

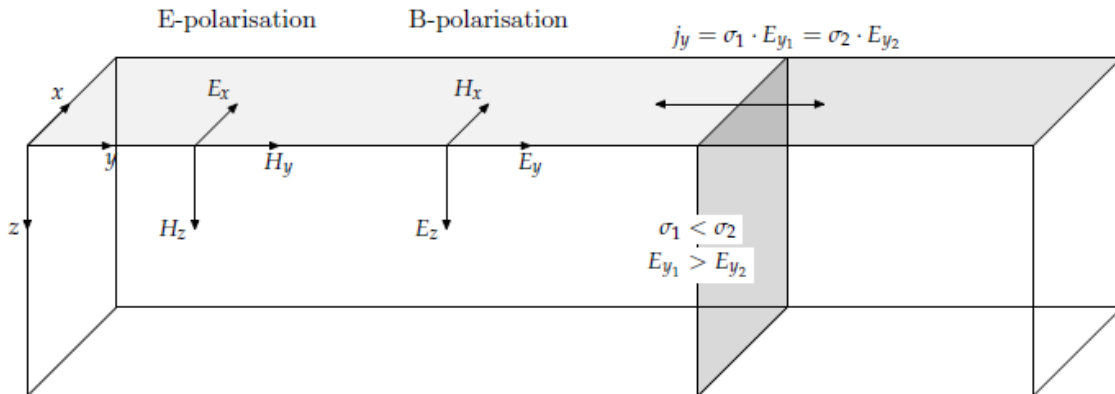


FIGURE 12: Two-dimensional resistivity model with a lateral contact striking in the x -axis

There is a resistivity boundary that separates two regions of different conductivity ($\sigma_1 < \sigma_2$). The electric field is discontinuous across the resistivity boundary.

It is rare to work with MT field layout in the strike direction due to lack of information on the geological structure; the axes generally don't coincide with the axes parallel and perpendicular to the geological strike. To be able to carry out 2-D analysis; the measuring axes should be rotated mathematically by an angle α to the respective polarization direction. Therefore, the diagonal components of the impedance tensor become zero and the new x' -axis is parallel to the geological strike (Section 4.3.4).

In this case, the impedance tensor needs to be decoupled into two independent modes by rotating to a coordinate system where x or y is parallel to strike and y or x perpendicular to strike (Berdichevsky and Dmitriev, 2008). Therefore, the Z_{2D} impedance tensor simplifies to:

$$Z_{2D} = \begin{pmatrix} 0 & Z_{xy} \\ Z_{yx} & 0 \end{pmatrix} \quad (4.53)$$

When the electric field is parallel to the electromagnetic strike; this is referred to as Transverse Electric (TE) mode or E-polarization, on other hand, the Transverse Magnetic (TM) mode or B-polarization is when the magnetic field is parallel to the electromagnetic strike. The diagonal elements of the impedance tensor are zero for a perfect 2-D earth (Equation 4.53) but this condition is not always observed with measured data due to distortion or 3-D induction.

Equation 4.1 provides the E-polarization in terms of the electromagnetic field components E_x , B_y and B_z as:

$$\text{E-polarization} \begin{cases} \frac{\partial E_x}{\partial y} = \frac{\partial B_z}{\partial t} = i\omega B_z \\ \frac{\partial E_x}{\partial z} = \frac{\partial B_y}{\partial t} = -i\omega B_y \\ \frac{\partial B_z}{\partial y} - \frac{\partial B_y}{\partial z} = \mu\sigma E_x \end{cases} \quad (4.54)$$

On other hand, the B-polarization in terms of magnetic field components will be given as:

$$\text{B-polarization} \begin{cases} \frac{\partial B_x}{\partial y} = -\mu\sigma E_z \\ \frac{\partial B_x}{\partial z} = \mu\sigma E_y \\ \frac{\partial E_z}{\partial y} - \frac{\partial E_y}{\partial z} = -i\omega B_x \end{cases} \quad (4.55)$$

From the Equation 4.53; TE mode is $Z_{TE} = Z_{xy} = \frac{E_x}{H_y}$ and TM mode is $Z_{TM} = Z_{yx} = \frac{E_y}{H_x}$

For each of the modes, the apparent resistivity can be calculated as:

$$\rho_{aTE}(\omega) = \frac{1}{\omega\mu_0} |Z_{TE}(\omega)|^2 \text{ and } \rho_{aTM}(\omega) = \frac{1}{\omega\mu_0} |Z_{TM}(\omega)|^2 \quad (4.56)$$

And the phase angle is given as

$$\phi_{TE}(\omega) = \tan^{-1} \left(\frac{\text{Im}Z_{TE}(\omega)}{\text{Re}Z_{TE}(\omega)} \right) \text{ and } \phi_{TM}(\omega) = \tan^{-1} \left(\frac{\text{Im}Z_{TM}(\omega)}{\text{Re}Z_{TM}(\omega)} \right) \quad (4.57)$$

iii. Three dimensional (3-D) impedance tensor

The conductivity, σ in a 3-D earth model (Figure 13) varies in all directions; $\sigma(x, y, z)$. The general form for the impedance tensor in 3-D earth model is

$$Z_{3D} = \begin{pmatrix} Z_{xx} & Z_{xy} \\ Z_{yx} & Z_{yy} \end{pmatrix} \quad (4.58)$$

All the elements in the tensor need to be considered in the interpretation. There is no direction in which the diagonal elements of the impedance tensor or any component of the tipper vector vanish; they are all non-zero elements.

From the full impedance tensor, we can derive different forms of apparent resistivity.

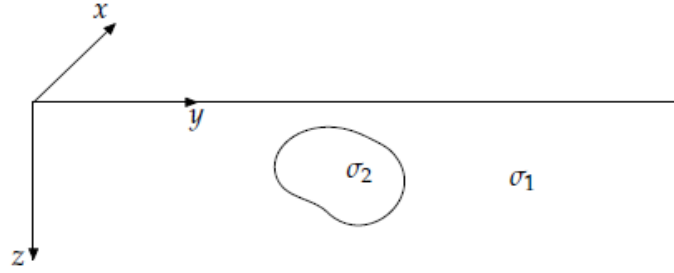


FIGURE 13: Three-dimensional resistivity model, σ varies in all three directions

The rotationally dependent tensor elements (Z_{xy} and Z_{yx}), provide the apparent resistivity and phase as:

$$\begin{aligned}\rho_{xy} &= \frac{1}{\mu_0\omega} |Z_{xy}|^2; \\ \rho_{yx} &= \frac{1}{\mu_0\omega} |Z_{yx}|^2 \text{ and phase} \\ \phi_{xy} &= \tan^{-1} \left(\frac{\text{Im}Z_{xy}}{\text{Re}Z_{xy}} \right) \\ \phi_{yx} &= \tan^{-1} \left(\frac{\text{Im}Z_{yx}}{\text{Re}Z_{yx}} \right)\end{aligned}\quad (4.59)$$

The rotationally independent determinant, $Z_{det} = \sqrt{Z_{xx}Z_{yy} - Z_{xy}Z_{yx}}$ gives:

$$\rho_{det} = \frac{1}{\mu_0\omega} |Z_{det}|^2 \text{ and phase } \phi_{det} = \arg(Z_{det}) \quad (4.60)$$

Arithmetic mean, $Z_{ave} = \frac{Z_{xy} - Z_{yx}}{2}$ gives:

$$\rho_{ave} = \frac{1}{\mu_0\omega} |Z_{ave}|^2 \text{ and phase } \phi_{ave} = \arg(Z_{ave}) \quad (4.61)$$

4.3.5 Mathematical rotation of the impedance

The impedance tensor depends on the coordinate frame of the measurement. The measurement axes have to be orthogonal, but their direction is otherwise arbitrary. A mathematical rotation can be applied to rotate the direction of the measurement axes, such that:

$$Z'(\omega) = R(\theta)Z(\omega)R(\theta)^T \quad (4.62)$$

where Z' is the rotated impedance, θ is the angle of rotation that is defined positive clockwise, and $R(\theta)$ and $R(\theta)^T$ are the rotation matrix and its transpose, respectively (Figure 14). They are defined as:

$$R(\theta) = \begin{bmatrix} \cos(\theta) & \sin(\theta) \\ -\sin(\theta) & \cos(\theta) \end{bmatrix} \text{ and } R(\theta)^T = \begin{bmatrix} \cos(\theta) & -\sin(\theta) \\ \sin(\theta) & \cos(\theta) \end{bmatrix} \quad (4.63)$$

Within the new coordinate system, the elements of the impedance tensor Z' can be written in terms of the original impedance tensor as:

$$\begin{aligned}Z'_{xx} &= Z_{xx}\cos^2\theta + (Z_{xy} + Z_{yx})\sin\theta\cos\theta + Z_{yy}\sin^2\theta \\ Z'_{xy} &= Z_{xy}\cos^2\theta + (Z_{yy} - Z_{xx})\sin\theta\cos\theta - Z_{yx}\sin^2\theta \\ Z'_{yx} &= Z_{yx}\cos^2\theta + (Z_{yy} - Z_{xx})\sin\theta\cos\theta - Z_{xy}\sin^2\theta \\ Z'_{yy} &= Z_{yy}\cos^2\theta + (Z_{xy} + Z_{yx})\sin\theta\cos\theta + Z_{xx}\sin^2\theta\end{aligned}\quad (4.64)$$

If the earth is two-dimensional; the principal directions are obtained by minimizing

$$|Z'_{xx}|^2 + |Z'_{yy}|^2 \quad (4.65)$$

or maximizing

$$|Z'_{xy}|^2 + |Z'_{yx}|^2$$

4.3.6 Geoelectric strike analysis for MT data

The impedance tensor can provide diverse information about dimensionality and directions. The geoelectric strike analysis for MT data serves for determination of the strike of dominant 2-D geo-electrical structure even though the noise and local distortion may be challenging. Normally, the strike angle is the least stable parameter which can be resolved from MT data (Jones and Groom, 1993).

In MT studies, the choice of the interpretation coordinate frame for the appropriate strike angle should be done cautiously especially in 2-D interpretation due to its critical importance. It is necessary to consult other information sources including geological strike.

In 2-D layered earth, the impedance tensor is given as:

$$Z_{2D} = \begin{pmatrix} 0 & Z_{TE} \\ Z_{TM} & 0 \end{pmatrix} \quad (4.66)$$

The impedance elements Z_{TE} and Z_{TM} relate the fields parallel and perpendicular to the geo-electrical strike, respectively. The angle of strike θ_0 is obtained from the measured impedances by maximizing suitable function of off-diagonal impedance, Z_{xy} and Z_{yx} under rotation of the axis as shown in Equation 4.65.

$$\theta_0 = 1/4 \tan^{-1} \frac{(Z_{xx} - Z_{yy})(Z_{xy} - Z_{yx})^* + (Z_{xx} - Z_{yy})^*(Z_{xy} + Z_{yx})}{|Z_{xx} - Z_{yy}|^2 - |Z_{xy} - Z_{yx}|^2} \quad (4.67)$$

where * denotes the complex conjugate.

Equation 4.67 gives four angles which maximize the off-diagonal components to form two principal directions perpendicular to each other.

The computed strike direction has a 90° ambiguity, since rotation by 90° only switches the location of the two principal impedance tensor elements within the tensor. The inherent $\pm 90^\circ$ ambiguity can be resolved by use of tipper strike, which uniquely defines the regional strike under the assumption of 2-D regional structure (Zhang et al., 1987). Sometimes, the local strike determined from MT data can deviate considerably from the geological strike.

4.3.7 Dimensionality measures

MT data can provide important information regarding the dimensionality of the Earth structure by their different parameters like skew, ellipticity, tipper magnitude and use of polar diagrams analysis.

Before going further into data analysis and processing for 2-D and 3-D; it is possible to get this useful information through simple techniques.

i. Skew

The measure of the EM coupling between the measured electric and magnetic variations in the same direction is known as ‘‘skew’’ and is given by the ratio of the sum of the diagonal and the difference between the off-diagonal impedance elements (Swift, 1967). It is calculated as:

$$\text{Skew} = \frac{|Z_{xx} + Z_{yy}|}{|Z_{xy} - Z_{yx}|} \quad (4.68)$$

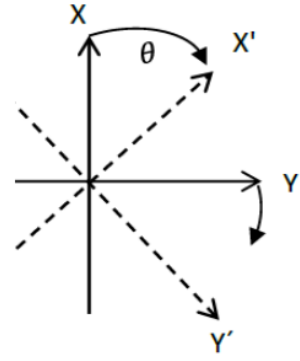


FIGURE 14: Rotation of reference frame

The skew parameter is rotationally invariant and can serve as an indicator of the dimensionality of the impedance tensor. Normally, for 1-D and 2-D structure, the skew should be zero but it is not easy to fulfill the required conditions in practice due the noise in the data. For 3-D structure, the skew value is always high and even goes beyond 0.2 except at a point of radial symmetry. Increased values indicate the presence of 3-D structure; therefore, the skew could be the measure of 3-dimensionality of conductivity structure on the site.

ii. Tipper magnitude

The Tipper is a useful measure of the tipping of the magnetic field out of the horizontal plane (Vozoff, 1991). For 1-D Earth, it is zero. For multidimensional Earth, the vertical magnetic component is equal to $T = T_x H_x + T_y H_y$ (Equation 4.43); where T stands for Tipper. The Tipper magnitude is given by:

$$|T| = \sqrt{|T_x|^2 + |T_y|^2}.$$

iii. Ellipticity

Ellipticity is a dimensionality parameter that is defined by the ratio of the impedance tensor similar to the skew but varies with rotation. It is defined by:

$$E(\alpha) = \left| \frac{Z_{xx}(\alpha) - Z_{yy}(\alpha)}{Z_{xy}(\alpha) + Z_{yx}(\alpha)} \right|$$

where α is angle of rotation.

The value of ellipticity is almost zero for 1-D earth when working with noise-free data.

For 2-D earth, it will also be close to zero if the x- or y-axis are along the geo-electric strike direction.

iv. Impedance polar diagrams

MT polar plots or polar diagrams are plots of $|Z_{yx}|$ and $|Z_{xx}|$ for a rotation from 0 to 360° at a particular frequency which can be used to evaluate the MT data dimensionality (Figure 15). For 1-D data, the plots appear in a circular form for the off-diagonal impedance while the polar diagram for the diagonal impedances they reduce to a point. For 2-D and 3-D resistivity structures, the principal impedance polar diagrams elongate in a direction either parallel or perpendicular to the strike (Reddy et al., 1977). The 2-D polar diagrams for Z_{xy} are oval and elongated along the symmetry lines. On other hand the Z_{xx} polar diagrams attain the shape of a clover leaf. Away from the symmetry lines, polar diagrams start to distort and their magnitudes become greater, particularly at the lower frequency indicating 3-dimensional structure.

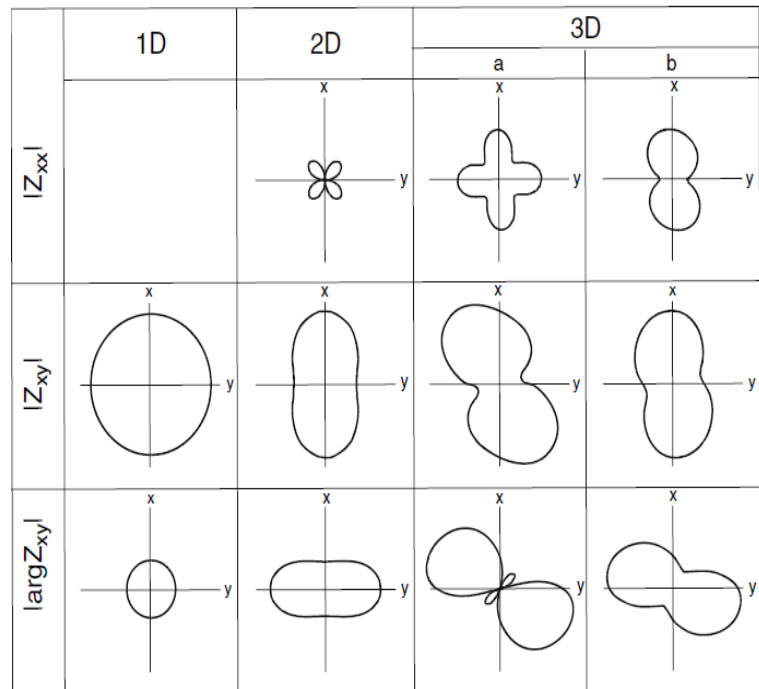


FIGURE 15: Polar diagrams of the impedance tensor (Berdichevsky and Dmitriev, 2002)

5. THE TRANSIENT ELECTROMAGNETIC (TEM) METHOD

5.1 TEM general concept

The Transient Electromagnetic (TEM) method, sometimes called the Time Domain Electromagnetics (TDEM) is a geophysical method which is used to obtain the subsurface resistivity (or conductivity) information. The TEM configuration is shown in Figure 16.

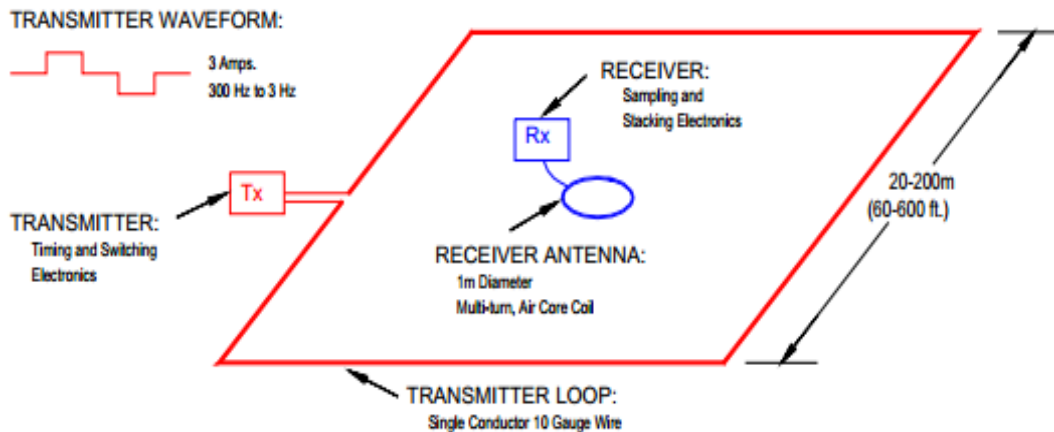


FIGURE 16: TEM sounding set up, the receiver coil is at the centre of the transmitter loop (Rowland, 2002)

The development of the TEM sounding method started in early 1950's; it was not commonly used due to lack of adequate instrumentation and interpretation methods. In 1970's, the development of instruments and methods of interpretation for TEM soundings attained high levels and became well known and used widely (Spies and Frischknecht, 1991).

The method involves using a specialized transmitter to drive a time varying current into a transmitter loop, usually an ungrounded loop of wire on the surface. The EM wave which is generated by the transmitter loop is then propagating into the subsurface. On its way, EM energy encounters different subsurface materials; it induces eddy currents that generate secondary EM fields. These secondary EM fields are collected up at the surface by receiver loop or magnetic antenna and recorded as the induced energy diffuses into the earth. The rate of diffusion indicates the resistivity of the subsurface materials.

According to Faraday's law of induction (Equation 4.1); a time varying magnetic field produces an electric field which in turn creates an electric current. Thus, the rapidly changing magnetic field induces eddy currents to flow in nearby conductors producing small secondary magnetic fields. Hence, the secondary magnetic fields attenuate with time: The terms "transient" and "time domain" are used to describe the method (Figure 17).

The EM eddy currents decay due to Ohmic dissipation into earth whereby their induced magnetic fields decrease and the induction process continues. The depth of investigation varies from tens of meters to over 1000 meters depending mainly on the size of the transmitter loop in use, quantity of power transmitted and ambient noise.

According to Nabighian and Macnae (1991); the depth to which eddy currents can reach in the Earth depends on the time from the current turn off and the conductivity of the Earth. Sternberg et al. (1988) show that the diffusion depth (time domain equivalent of skin depth) of the central loop TEM method is given as:

$$\delta_{\text{TEM}}(t) = 1.28 \sqrt{t / \sigma \mu} \text{ [m]} \quad (5.1)$$

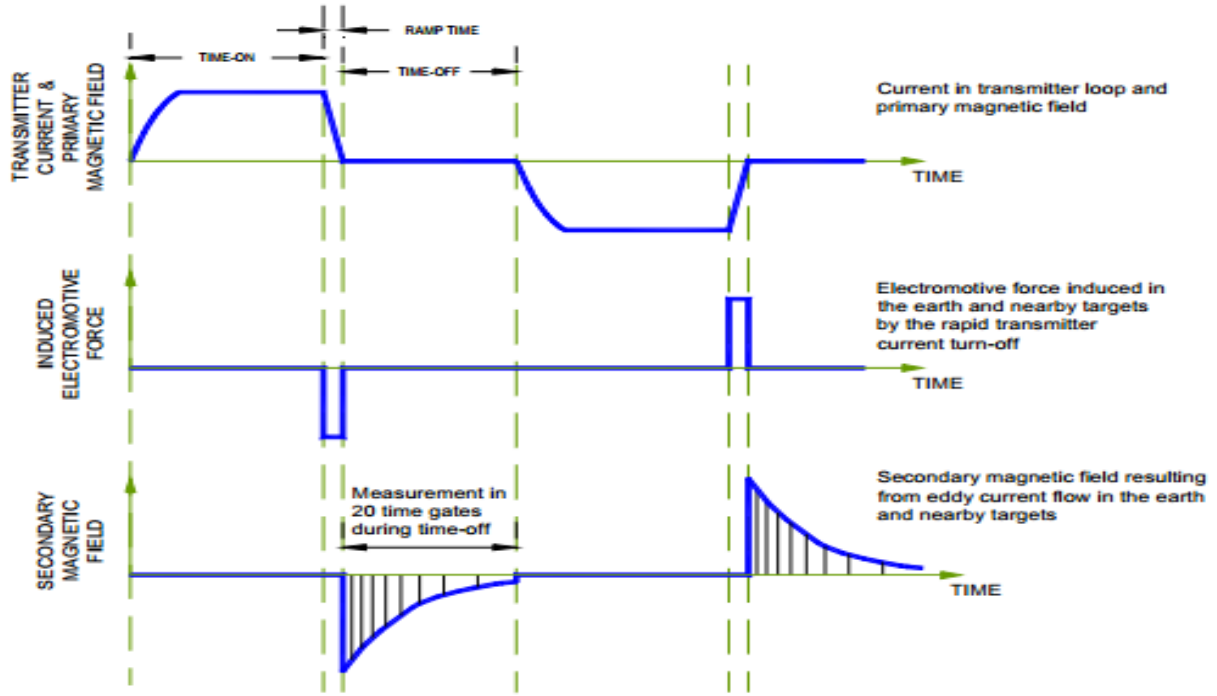


FIGURE 17: Basic principles of the TEM method: The current in the transmitter loop (top). The induced electromotive force in the ground (middle) and at bottom; the secondary magnetic field measured in the receiver coil (Christensen et al., 2006)

5.2 Calculation for voltage in central loop TEM

The voltage in the receiver loop after switching off a constant current I_0 in a circular transmitter loop can be calculated as:

$$V(r, t) = \frac{2}{\pi} A_r n_r A_s n_s \frac{\mu_0}{2\pi r^3} \int_0^\infty \mathcal{R}(E^e(\omega, r)) \cos \omega t d\omega \quad (5.2)$$

Thus,

$$V(t, r) \approx I_0 \frac{C(\mu_0 \sigma r^2)^{3/2}}{10\pi^{1/2} t^{5/2}} \quad (5.3)$$

where $C = A_r n_r A_s n_s \frac{\mu_0}{2\pi r^3}$;
 A_r = Area of the receiver coil [m²];
 n_r = Number of turns in the receiver coil;
 A_s = Area of the transmitting loop [m²];
 n_s = Number of turns in transmitting loop;
 t = Time elapsed after the current in the transmitter is turned off [s];
 μ_0 = Magnetic permeability [Henry/m];
 $V(t, r)$ = Transient voltage [V];
 r = Radius of the transmitter loop [m]; and
 I_0 = Current in the transmitting loop [A].

As detailed by Árnason (1989); the transient response in Equation 5.2 should be calculated numerically. The electrical field E^e is an integral as well that needs to be evaluated numerically for a layered Earth. The transient voltage for late times after the current in the transmitter is abruptly turned off, is proportional to $\sigma^{3/2}$ and falls off with time as $t^{-5/2}$.

By solving for resistivity in the Equation 5.3; the apparent resistivity for the TEM is given by the following equation:

$$\rho_a(r, t) = \frac{\mu_o}{4\pi} \left(\frac{2\mu_o A_r n_r A_s n_s I_o}{5 t^{5/2} V(t, r)} \right)^{2/3} \quad (5.4)$$

MTU is monitoring the acquisition procedure by filtering, amplifying and converting data into digital format to facilitate the storage into memory card. The five channels as indicated by their names; are two orthogonal horizontal electric fields (E_x , E_y) and three channels for the orthogonal horizontal (H_x , H_y) and vertical (H_z) magnetic fields (Figure 8). The measurements of potential difference (ΔV) between pairs of electrodes forming a dipole and buried in ground to mitigate temperature variations, at distance d gives the electric field as follows: $E = \Delta V/d$.

At the measurement site which should be relatively free from both cultural and electrical noise and relatively flat; one electric dipole is seated in the magnetic north-south direction and other one is oriented in east-west position. Commonly, the used electrodes are non-polarisable formed by a plastic pot with a porous bottom filled with a lead chloride ($PbCl_2$) solution.

To enhance ground contact and electrical conductivity, the bottom of each electrode is smeared with bentonite (clay) to prevent the electrolyte from drying up and salty water is also poured in each hole before the electrode is placed. However, this use of bentonite is not advisable when dealing with long-period MT soundings where it may dry out over the duration of recording time and cause the potential difference to drift (Simpson and Bahr, 2005). On the other hand; magnetic fields are obtained from magnetic coils seated in x, y and z directions. Among the useful accessories; a spirit level and compass are used to adjust the axes in the ways that x and y are horizontal and orthogonal to each other, then z is vertically seated.

In the survey, one MTU-5A set is installed far away from the main survey area about some tens of kilometers. It is maintained as a remote reference station and records continuously. During data processing, it is used to obtain better quality data with higher signal to noise ratio and also to remove the bias caused by local noise sources (Gamble et al., 1979).

The acquisition unit which acts as the receiver is connected to a 12V DC battery and a memory card is inserted for data storage; it is also grounded by an electrode. The real time GPS (Global Positioning System) for time series synchronization with satellites is also done and connected to the same acquisition unit.

When the data have been successfully collected; the electric and magnetic field variations are recorded as time series. These time series are composed of harmonic (sinusoidal) components of different frequencies. It is noticed that waves with high frequencies are attenuated at shallow depth and they are not able to penetrate deeper. However, the waves with low frequencies (long periods) have the capacity of penetrating deeper into the earth. Therefore, MT has proven as a tool with high penetration capacity from shallow depths to several tens of kilometers. In the next step of data processing; the time series are sorted into different frequencies by using Fourier transformation methods and the relation between the electric and magnetic fields give information about the resistivity at different depths. For this specific field carried out in Asal rift, the survey crew had a challenge since the MT signal was terribly weak and had to record 48 hours instead of the normal 24 hours recording to be able to collect data with enough quality.

6.2 The MT data processing algorithm

The data recorded by MT data logger and stored on memory card in form of time series are then downloaded for further processing. The first thing to be done at this stage is the inspection of data by using the synchro-time series viewer program (Phoenix Geophysics, 2005). With the same program; it is possible to view and print the graphical representations of the raw time series data, power spectra that are derived from the time series data and coherence between pairs of orthogonal electric and magnetic components as described in Equation 4.46. Information about magnetic declination of the study area should be provided and saved into the startup file; this serves when the program rotates the impedance tensor elements to the geographic north-south direction. The magnetic declination in Asal rift area, Djibouti is $+1^{\circ}49'$. The processing of MT data transforms the time varying geo-electric field components

into earth response functions. The last ones contain information regarding the distribution of the conductivity structure. Three general time series processing steps are here discussed below.

6.2.1 Data review and editing

The time series are then divided into M segments containing N data points per segment. The N-value is chosen based on the recorded time window such that each segment contains evaluation periods equally spaced on logarithmic scale. Additionally, each time window must be divided into a sufficient number of segments for further statistical estimation of the transfer functions. Definition of segments followed by inspection with the purpose of identifying and removing trends and noise effects. The action is performed automatically or manually by using MT editor program.

6.2.2 Conversion of time series to frequency domain

The same manufacturer of MT equipment provides also computer programs including SSMT2000 program (Phoenix Geophysics, 2005) which was used to perform time series processing by using a robust processing technique and editing the results (Egbert and Booker, 1986). The measured time series are Fourier transformed into the frequency domain. The measured channels E_i ($i=x, y$) and H_j ($j=x, y, z$) for each segment, are converted from time series to frequency domain by using the discrete Fourier transform (Brigham, 1974). Conversion from time series to frequency domain is commonly performed by Fast Fourier Transform (FFT) method due to its speed (Vozoff, 1991). A raw spectrum with N/2 frequencies is then attained. Thereafter, the evaluation frequencies; equally distributed in log scale, optimally 6-10 per period decade are chosen. The final spectra are smoothed by averaging over neighbouring frequencies using Parzen-Window Density Estimation.

It is important to calibrate each field component according to the instrument sensitivity at a given frequency. The product of field components and their respective complex conjugates produce auto and cross spectra segments K, and they are calculated from segments of the original time series for each frequency as: $\langle E_{Kj}(\omega) \cdot E_{Kj}^*(\omega) \rangle$; $\langle H_{Kj}(\omega) \cdot H_{Kj}^*(\omega) \rangle$; $\langle E_{Kj}(\omega) \cdot H_{Kj}^*(\omega) \rangle$ and $\langle H_{Kj}(\omega) \cdot E_{Kj}^*(\omega) \rangle$. They are stored in the spectral matrix, which contains the distribution from all the segments at a specific frequency.

By estimation, the auto-spectral density or spectrum of one channel A around frequency f_j in the band (f_{j-m}, f_{j+m}) is given by:

$$\langle A(f_j) \rangle = \sqrt{\frac{1}{2m+1} \sum_{k=j-m}^{j+m} A_k A_k^*} = \langle A_j A_j^* \rangle^{1/2} \quad (6.1)$$

where A represents E or H. Its square is the autopower spectral density at f_j .

Also, the crosspower density at f_j of two channels A and B is given by:

$$\langle A(f_j) \cdot B(f_j) \rangle = \frac{1}{2m+1} \sum_{k=j-m}^{j+m} A_k B_k^* = \langle A_j B_j^* \rangle$$

The following relations are used to determine the tensor elements time series as Fourier transformed:

$$\begin{aligned} E_x(t) &\rightarrow E_x(\omega) & E_y(t) &\rightarrow E_y(\omega) \\ H_x(t) &\rightarrow H_x(\omega) & H_y(t) &\rightarrow H_y(\omega) \end{aligned} \quad (6.2)$$

6.2.3 Robust estimation of transfer functions

As discussed in Section 4.3.4, MT transfer function is a function that relates the measured magnetic and electric fields at a given frequency. It depends only on the electrical properties of the material through which the EM waves are propagating but does not depend on their source. The most common MT

transfer functions are represented by the impedance tensor or MT tensor and the geomagnetic transfer function (tipper vector or vertical magnetic transfer function).

From Equations 4.43, 4.47 and 4.48:

$$H_z(\omega) = \mathcal{T}_{zx}H_x(\omega) + \mathcal{T}_{zy}H_y(\omega), \text{ and}$$

$$E_x(\omega) = Z_{xx}(\omega)H_x(\omega) + Z_{xy}H_y(\omega), \quad E_y(\omega) = Z_{yx}(\omega)H_x(\omega) + Z_{yy}H_y(\omega)$$

The measured electric and magnetic field contain measurement noise due to plane wave source field approximation which introduces uncertainties of the impedance tensor. Statistically, it is preferable to record many sets which facilitate the averaging to reduce the noise.

Conventionally, the way of solving the above equations assumes that Z_{ij} are constant over an averaging band (window), which is physically reasonable if the bands are narrow enough. In each band the crosspowers are taken with H_x and H_y , giving the following pairs of equations:

$$\begin{aligned} \langle E_x(\omega)H_x^*(\omega) \rangle &= Z_{xx}(\omega)\langle H_x(\omega)H_x^*(\omega) \rangle + Z_{zy}(\omega)\langle H_y(\omega)H_x^*(\omega) \rangle \\ \langle E_y(\omega)H_y^*(\omega) \rangle &= Z_{yx}(\omega)\langle H_x(\omega)H_y^*(\omega) \rangle + Z_{yy}(\omega)\langle H_y(\omega)H_y^*(\omega) \rangle \end{aligned} \quad (6.3)$$

where $H_x^*(\omega)$ and $H_y^*(\omega)$ are the complex conjugates of horizontal magnetic field.

On the other hand, the cross power of tipper H_z taken with H_x and H_y gives the two equations:

$$\begin{aligned} \langle H_z(\omega)H_x^*(\omega) \rangle &= \mathcal{T}_{zx}(\omega)\langle H_x(\omega)H_x^*(\omega) \rangle + \mathcal{T}_{zy}(\omega)\langle H_y(\omega)H_x^*(\omega) \rangle \\ \langle H_z(\omega)H_y^*(\omega) \rangle &= \mathcal{T}_{zx}(\omega)\langle H_x(\omega)H_y^*(\omega) \rangle + \mathcal{T}_{zy}(\omega)\langle H_y(\omega)H_y^*(\omega) \rangle \end{aligned} \quad (6.4)$$

Therefore, by solving the pairs of simultaneous equations for impedance and tipper, we find out six independent estimates of the transfer functions (Vozoff, 1972):

$$\begin{aligned} Z_{xx} &= \frac{\langle E_x H_x^* \rangle \langle H_y H_y^* \rangle - \langle E_x H_y^* \rangle \langle H_y H_x^* \rangle}{\langle H_x H_x^* \rangle \langle H_y H_y^* \rangle - \langle H_x H_y^* \rangle \langle H_y H_x^* \rangle} \\ Z_{xy} &= \frac{\langle E_x H_x^* \rangle \langle H_x H_y^* \rangle - \langle E_x H_y^* \rangle \langle H_x H_x^* \rangle}{\langle H_y H_x^* \rangle \langle H_x H_y^* \rangle - \langle H_y H_y^* \rangle \langle H_x H_x^* \rangle} \\ Z_{yx} &= \frac{\langle E_x H_x^* \rangle \langle H_y H_y^* \rangle - \langle E_y H_x^* \rangle \langle H_y H_y^* \rangle}{\langle H_x H_x^* \rangle \langle H_y H_y^* \rangle - \langle H_x H_y^* \rangle \langle H_y H_x^* \rangle} \\ Z_{yy} &= \frac{\langle E_y H_x^* \rangle \langle H_x H_y^* \rangle - \langle E_y H_y^* \rangle \langle H_x H_x^* \rangle}{\langle H_y H_x^* \rangle \langle H_x H_y^* \rangle - \langle H_y H_y^* \rangle \langle H_x H_x^* \rangle} \\ \mathcal{T}_{zx} &= \frac{\langle H_z H_x^* \rangle \langle H_y H_y^* \rangle - \langle H_y H_x^* \rangle \langle H_z H_y^* \rangle}{\langle H_x H_x^* \rangle \langle H_y H_y^* \rangle - \langle H_y H_x^* \rangle \langle H_x H_y^* \rangle} \\ \mathcal{T}_{zy} &= \frac{\langle H_z H_y^* \rangle \langle H_x H_x^* \rangle - \langle H_z H_x^* \rangle \langle H_x H_y^* \rangle}{\langle H_x H_x^* \rangle \langle H_y H_y^* \rangle - \langle H_y H_x^* \rangle \langle H_x H_y^* \rangle} \end{aligned} \quad (6.5)$$

6.3 Remote reference and MT impedance estimation

In Section 6.1, the remote reference technique applied in MT data acquisition was discussed. This technique consists of deploying additional MT sensors at a chosen quiet site, outside the influence of cultural noise and remote from the survey area (Goubau et al., 1979; Clarke et al., 1983). It is assumed that the induced field is coherent over spatial scales of many kilometres. Also, the noise is generally random and incoherent at two locations far away from each other (10-100 km). Thus, it is possible to remove uncorrelated bias effects between the sites arising from the presence of noise by measuring selected electromagnetic components at both local and remote sites. But, the same technique doesn't work when correlated noise is present in both local and remote sites. The set of Equations 6.5 described

here contain the auto-powers of the magnetic field and the problem with above procedure is the bias effect of noise. The coherent noise in the data at single site causes the impedance estimate, Z_{ij} to be biased.

In order to avoid any effect of the noise, the remote site should be as far as possible from the local so that the sources of noise are incoherent. In this survey, the remote station was located 10 km away from Asal rift (survey area).

Considering the linear relationship between electric and magnetic field spectra of the impedance tensor as described by Equation 4.47 and 4.48 and multiply it with the remote site components, R_x^* and R_y^* by averaging over a number of determinations. The pairs of simultaneous equations for impedance can be solved to get the following remote reference estimates of the impedance tensor elements Z_{ij} here below:

$$\begin{aligned}
 Z_{xx} &= \frac{\langle E_x R_x^* \rangle \langle H_y R_y^* \rangle - \langle E_x R_y^* \rangle \langle H_y R_x^* \rangle}{\langle H_x R_x^* \rangle \langle H_y R_y^* \rangle - \langle H_x R_y^* \rangle \langle H_y R_x^* \rangle} \\
 Z_{xy} &= \frac{\langle E_x R_x^* \rangle \langle H_x R_y^* \rangle - \langle E_x R_y^* \rangle \langle H_x R_x^* \rangle}{\langle H_y R_x^* \rangle \langle H_x R_y^* \rangle - \langle H_y R_y^* \rangle \langle H_x R_x^* \rangle} \\
 Z_{yx} &= \frac{\langle E_x R_x^* \rangle \langle H_x R_y^* \rangle - \langle E_y R_y^* \rangle \langle H_y R_x^* \rangle}{\langle H_x R_x^* \rangle \langle H_y R_y^* \rangle - \langle H_x R_y^* \rangle \langle H_y R_x^* \rangle} \\
 Z_{yy} &= \frac{\langle E_y R_x^* \rangle \langle H_x R_y^* \rangle - \langle E_y R_y^* \rangle \langle H_x R_x^* \rangle}{\langle H_y R_x^* \rangle \langle H_x R_y^* \rangle - \langle H_y R_y^* \rangle \langle H_x R_x^* \rangle}
 \end{aligned} \tag{6.6}$$

In the above equations, R_x and R_y represent the magnetic components H_x and H_y of the remote reference stations, respectively. The use of electric field components E_x and E_y of the remote reference as R_x and R_y is also possible. It is however, common to use the magnetic field since the horizontal magnetic field is known to be less susceptible to polarization, and is less contaminated by noise than the electric field. Another useful property of remote reference technique is to provide estimates of noise in each of the channel (Gamble et al., 1979). It makes possible to estimate the noise in each of the impedance elements at each frequency.

However, in many circumstances with high noise effects, the resulting cross powers may not be as smooth as preferred. In this case, manual editing by using MT-Editor programme of the stacked apparent resistivity values for each frequency is used to produce practical results and smoother curves.

For the study discussed here, Fourier transform band averaged cross and auto-powers were calculated by using robust processing method. MT-Editor program was used to edit graphically the cross-powers by masking the noisy data points in order to evaluate coherences for both phase and apparent resistivity. The final cross and auto-powers with related calculated MT parameters (i.e. impedances, phase coherences, apparent resistivity, strike directions, skew, ellipticity, etc.) are stored in Electrical Data Interchange format (EDI). The file is then ready for plotting and export to interpretation software for multidimensional inversion. The output of MT-Editor (edi file) was taken and run through spec2edi Linux based program developed at ÍSOR which calculates various MT parameters (some are not implemented in MT-Editor) and generates the results in the standard of the Electrical Data Interchange (EDI) for further interpretation.

6.4 TEM survey instrumentations at Asal rift

The resistivity survey using TEM method was one of the preliminary geoscientific surveys carried out in 1988 within Asal Rift by Orkustofnun (National Energy Authority of Iceland) (Árnason et al., 1988). The TEM data were insufficient as the survey covered only a limited area and depth of penetration was not great. An additional survey was suggested for carrying out more TEM soundings and including MT soundings for deep resistivity structure study of Asal Rift. It was conducted in 2007-2008 by Iceland

GeoSurvey (ISOR). A total of 105 TEM soundings are used in this project as they were collected near the same sites as the MT soundings to allow the joint inversion to correct the MT data static shift (for location see Figure 18).

The TEM data were collected by using PROTEM 67 equipment from Geonics Ltd. Field setup is well described here in section 5; in the survey the transmitter loop size was 300 m x 300 m and the transmitted current was around 20 to 23 A. In the receiver coil, the induced voltage was measured in two segments of 20 time gates equally spaced in logarithmic scale. Two frequencies were used; the first at 2.5 Hz and the second at 25 Hz with effective area of 100 m² for receiver coil. The segments overlap by 10 gates and together they span 30 time gates from 0.09 to 70 ms after the current turn-off.

6.5 TEM data processing

The raw TEM data recorded on the receiver internal memory were downloaded. The processing work was performed by using a special program Temx, developed at ISOR; it has the ability of averaging data acquired at the same frequency and calculate the late time apparent resistivity as a function of time after the turn-off. It helps to eliminate outliers and unreliable data points before the data can be used for interpretation. By using TEMTD Linux based program developed at ISOR (Árnason, 2006a); it was possible to achieve 1-D inversion for TEM data. The forward algorithm calculates the induced transient voltage in the receiver as the sum of the responses from successive current turn-on and turn-off times. The transient response is calculated both as induced voltage and late time apparent resistivity as a function of time. A non-linear least- squares inversion of Levenberg-Marquardt method is the type of inversion algorithm used in the program (Árnason, 1989). The inversion starts with the data and an educated guess of an initial model. The inversion algorithm improves the model in an iterative process. It runs by calculating adjustments to the model from the difference between the measured data and the response of the model until a satisfactory agreement has been reached.

The inversion produces the statistically best solution and determines estimates of the model parameters. It can detect the well determined parameters or the poorly determined ones and how the estimates may be interrelated (Flóvenz et al., 2012).

The misfit function is the root-mean-square (chi^2 , χ^2), difference between measured and calculated values weighted by the standard deviation of the measured values. The user has the option of choosing whether the program fits the measured voltages or the late time resistivity values. To obtain smooth models; damping is achieved by utilizing both first derivatives and second derivatives (Árnason, 2006b).

The actual function that is minimised is not just the weighted root-mean-square (chi^2) but the potential (Pot).

$$Pot = chi^2 + \alpha DS1 + \beta DS2 + \gamma DD1 + \delta DD2 \quad (6.7)$$

where DS1 and DS2 are first and second order derivatives of log-conductivities in the layered model, DD1 and DD2 are first and second order derivatives of logarithms of the ratios of layer depths. The coefficients α , β , γ and δ are the relative contributions of the different damping terms.

It is also possible to perform minimum structure (Occam) inversion with the same program where the input file for TEMTD is the output file from TEMX for TEM. In this case the layer thicknesses are kept fixed, equally spaced on log scale, and the conductivity distribution is forced to be smooth by adjusting α and β (Equation 6.7).

7. MODELLING OF EM DATA FROM ASAL GEOTHERMAL AREA

The electromagnetic (MT and TEM) data were already processed and ready for the next step of modelling with the purpose of achieving the geophysical exploration target. At this step, we need to obtain reliable information regarding resistivity distribution underneath the area of interest through inversion processes. In this project, a general overview of 1-D and 3-D EM inversion routines are discussed. The application of the EM method was initially based on 1-D interpretation and different developers have contributed to the inversion codes which are being used today (Constable et al., 1987; Smith and Booker, 1991). Therefore, programs like TEMTD for 1-D inversion (Árnason, 2006a), REBOCC (Reduced Basis Occam) for 2-D inversion (Siripunvaraporn et al., 2000) and WSINV3DMT for 3-D inversion (Siripunvaraporn et al., 2005) were developed.

7.1 Inversion of geophysical data

The outcome from a planned geophysical exploration work is to obtain information about the subsurface of the study area. The results are interpreted based on the existing geological features which are in some cases correlated or have some relations. The measured data should be explained by the detailed structure of the physical properties within the area of study and linked to their surroundings (Rosenkjær, 2011)

Here we discuss the forward modelling which is a process of computing responses for a physical property distribution in either 1-D, 2-D or 3-D. Theoretically speaking, we assign constant physical properties to each cell in the model, m , and physical relationships enable us to compute data resulting from m . The common ways of discretization are based on use of rectangular or triangular meshes where all the calculation formulations depend on these meshes. On the other hand, an inversion problem uses the forward modelling to find a physical property model where the misfit between the predicted and measured data are at a preferred level. The misfit functional below serves us to calculate the data misfit:

$$\phi_d = \sum_{i=1}^N \left(\frac{d_i^{meas} - d_i^{pred}}{\sigma_i} \right)^2 \quad (7.1)$$

where N is the number of data, d^{meas} is the measured data, d^{pred} is the predicted data and σ is the standard deviation estimate of the errors for the difference between the measured and predicted data.

It is impossible to assign exact errors but often a simple assumption of independent Gaussian errors are used with a zero mean and standard deviation of σ . The determination of σ should be carefully evaluated as we are working with different kinds of noise like modelling errors and repeatability with an unknown correlation. The good estimate of the standard deviation gives the possibility of getting the target misfit in Equation 7.1 equal to the number of data N . In the inversion problem we have the difficulty of non-uniqueness and also the inversion problem is typically underdetermined. There is less data compared to the degrees of freedom in the model. Since, many models can produce data within the desired data misfit; we need to add more constraints and regularization for better outcome model. In the inversion, the choice of the regularization plays a big role and it is commonly regularised to find a best model that has a smallest perturbation and is smoother compared to a user defined reference model. The following model objective functional is mostly used:

$$\phi_m = \alpha_s \int_{\Omega} w_s (m - m_{ref})^2 dV + \alpha_r \int_{\Omega} w_r \left(\frac{d(m - m_{ref})}{dr} \right)^2 dV \quad (7.2)$$

where m_{ref} the reference model is constructed from geological and a priori information, w_s is the smallness weighting and w_r is the directional smoothness weighting. The directions used are typically the x , y and z directions in the model. α_s and α_r are the trade off parameters controlling the relative importance between the smallness and the smoothness and Ω is the discretized domain.

The inverse problem is defined as the minimization of a functional $\phi(m)$ that is a combination of the data and the model functionals in Equations 7.1 and 7.2, respectively. Hence, the inversion is able to minimize the following equation:

$$\phi(m) = \phi_d(m) + \beta\phi_m(m) \quad (7.3)$$

where β is the trade-off parameter of Tikhonov parameter which controls the relative importance of the model functional in the objective function in Equation 7.3.

We need to choose the value of β such that when $\phi(m)$ is at a minimum then $\phi_d(m)$ equals the number of data, N (Oldenburg and Li, 2005).

7.2 Applying 1-D inverse modelling code

To perform 1-D inversion for TEM and MT data, TEMTD program was used in the previous work carried out in Asal geothermal field by Árnason et al. (2008). The program was written by Knútur Árnason of ÍSOR (Árnason, 2006a) and can do 1-D inversion of TEM and MT data separately and/or jointly. With this program, one is able to invert MT apparent resistivity and phase derived from the rotationally invariant determinant of the MT tensor elements or the average of the off-diagonal elements. Joint inversion is the method applied in this particular project to overcome the MT static shift problem; the additional parameter namely “static shift multiplier” is inverted for (in addition to the layered model parameters) and it needs to fit both the TEM and MT data within the same model.

TEMTD can do both standard layered inversion (inverting for resistivity values and layer thickness) and Occam (minimum structure) inversion with exponentially increasing layer thicknesses with depth. The program offers a user specified damping of first (sharp steps) and second order derivatives (oscillations) of model parameters (logarithm of resistivity and layer thicknesses), (Árnason, 2006a). Occam’s inversion seeks the smoothest or minimum norm, model subject to an appropriate fit to the data (Constable et al., 1987, deGroot-Hedlin and Constable, 1990). The same program is discussed in this project under Section 6.5 and with Equation 6.7, additional mathematical demonstrations are provided.

7.3 Application of WSINV3DMT code for 3-D inversion

In order to model resistivity data using the 3-D inversion method for Asal geothermal field; the WSINV3DMT code was used. The code which was written by Weerachai Siripunvaraporn (Siripunvaraporn et al 2005; Siripunvaraporn and Egbert, 2009) is full 3-D inversion program and mathematical tool which calculates the model that best fits the data. It is an extension of 2-D data space Occam inversion which was originally introduced by Constable et al. (1987) for 1-D MT data. The fact that they are all Occam and 3-D inversions is based on the model-space matrices; all computations depending on the size of model parameter, M justify the difficulty associated to their applications. To overcome this complicated situation, it uses finite difference forward algorithm and utilizes a formulation of the inverse problem in the data space rather than in the model space; which has radically reduced the dimensionality of the problem and made feasible 3-D inversion of MT data (Hersir et al., 2013). In this case, matrix dimensions depend on the size of the data set, N instead of depending on the number of model parameters M .

The 3-D forward modelling algorithm is based on a staggered grid finite difference solution of Maxwell’s equations which allows complicated model structures (Siripunvaraporn et al., 2005). To apply this code, the data parameter size N stands for the total size of the dataset, which is generally the product of the number of periods N_p , the number of stations N_s and the number of responses N_r (maximum is 8 for all impedances); $N = N_p \times N_s \times N_r$.

On the other hand, the model parameter size M is the total number of discretization blocks which is a product of the number of discretization in X (North-South) M_x , number of discretisation in Y (East-West) M_y and number of discretization in Z (vertical) M_z ; $M = M_x \times M_y \times M_z$.

The RAM storage memory of $1.2 \times (8N^2 + 8NM)$ is needed for WSINV3DMT program to be able to store the $N \times N$ matrix and $N \times M$ sensitivity matrix. The program requires extra memory for other computations but the total storage is dominated by these two matrices. The factor 1.2 is an average approximation and ranges between 1.0 to 1.4 (or larger) depending on N and M (Siripunvaraporn et al., 2006).

7.3.1 Data preparation and 3-D inversion

Extra work is needed to make MT data ready for running the WSINV3DMT code. Given that the processed MT data have the x-axis in true north, a mathematical rotation (Figure 14) was performed considering the Asal rift fissure swarms (Figure 1). The processed data and the model are defined in an internal (local) coordinate system or grid. In preference, one of the axes should be parallel to the dominant electric strike. According to the fissure swarm orientation in Asal rift, we have rotated the x-axis to 50° west of north. The internal coordinate system of the model is then, taken to have x-axis in $N50^\circ W$ where the MT impedance tensors were consequently rotated by -50° to the direction of the internal system.

The 3-D inversion is an iterative minimization process and the outcomes from the process are highly depending on the choice of initial model. It is known that the 3-D inversion of MT data is purely underdetermined problem; the number of unknown resistivity values is much bigger than the number of data values. In this project, the number of data points is 13020 (105 soundings \times 31 periods \times 4 real and imaginary off-diagonal tensor elements) while the model has 86528 unknown resistivity values ($52 \times 52 \times 32$). Hence, the inversion needs to be regularized by imposing constraints on the model (to make the model parameters interdependent in such a way that the number of actually free parameters is reduced). This can be achieved by constraining the model parameters to vary smoothly; it is commonly known as minimum structure or Occam inversion (Constable et al., 1987). Alternatively, it is also possible to perform the regularisation by using reference or "prior" model and constraint the inversion model not to deviate too much from prior model. The method of using a prior model allows the fixing some of the model parameters to a priori known values. The WSINV3DMT code uses the combination of these regularisation methods and minimises a "penalty function"; this is a weighted sum of the difference between measured data and calculated response (data misfit), the roughness of the model and the deviation from the prior model. It has the capacity of adjusting at earlier stage the model and reducing the severe misfit of the data. As it is iterating, the changes that would further decrease the data misfit are excluded as they may cause a severe deviation of the model from the prior model (Hersir et al., 2013).

7.3.2 Static shift analysis for 3-D inversions

The static shift problem discussed earlier in Section 4.2, is a commonly known issue in MT surveys in volcanic areas (as e.g. in Asal geothermal field). This problem is assumed to be mainly resulting from the distortion of the electric field. In this problem, the joint 1-D inversion between each of the polarizations and the TEM sounding collected at the same site could be the reliable solution by determining the shift in MT data. By using the program TEMTD for 1-D joint inversion of the rotated MT data and corresponding TEM soundings, we found out the static shift multipliers in the Asal area. The following formula describes the relationship between the shift multipliers for the xy and yx polarizations (Figure 19) of apparent resistivity and the shift corrected tensors (Árnason et al., 2010).

$$\begin{bmatrix} Z_{xx}^c & Z_{xy}^c \\ Z_{yx}^c & Z_{yy}^c \end{bmatrix} = \begin{bmatrix} C_x & 0 \\ 0 & C_y \end{bmatrix} \begin{bmatrix} Z_{xx} & Z_{xy} \\ Z_{yx} & Z_{yy} \end{bmatrix} = \quad (7.4)$$

and

$$C_x = \sqrt{1/S_{xy}}; \quad C_y = \sqrt{1/S_{yx}} \quad (7.5)$$

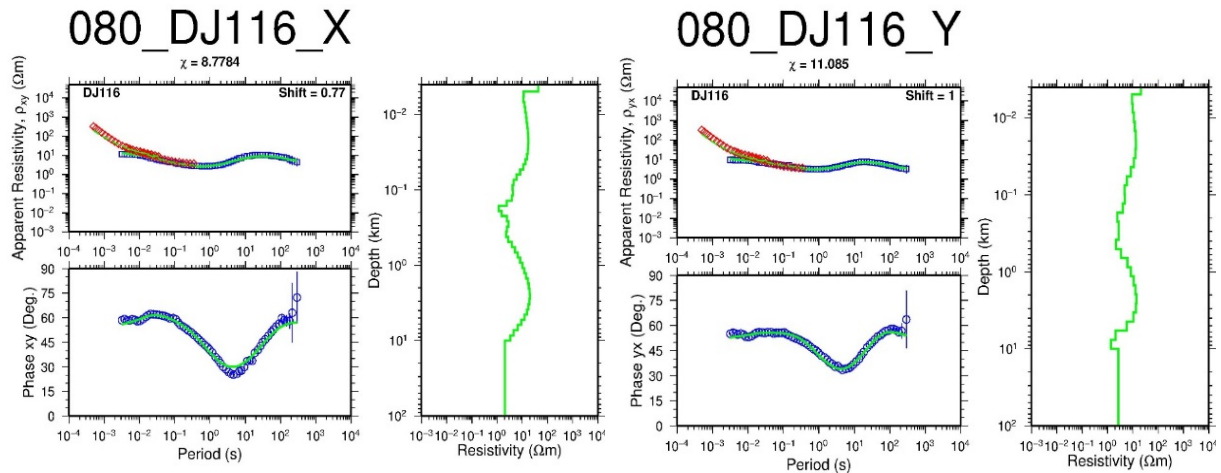


FIGURE 19: 1-D joint inversion of a TEM sounding and the xy (to the right) and yx (to the left) polarization of the nearby MT soundings in order to determine the static shift of MT data

where S_{xy} and S_{yx} are the shift multipliers for the xy and yx polarizations of apparent resistivity, respectively, Z^c and Z are corrected and uncorrected tensors, respectively.

The static shift multipliers for xy and yx polarizations for all MT soundings (105) collected from Asal rift and used in the 3-D inversion are plotted as histogram in Figure 20. The histogram shows that the static shift multipliers are in the wide range of 0.0 to 2.4 for xy polarization and 0.0 to 7.7 for yx polarization.

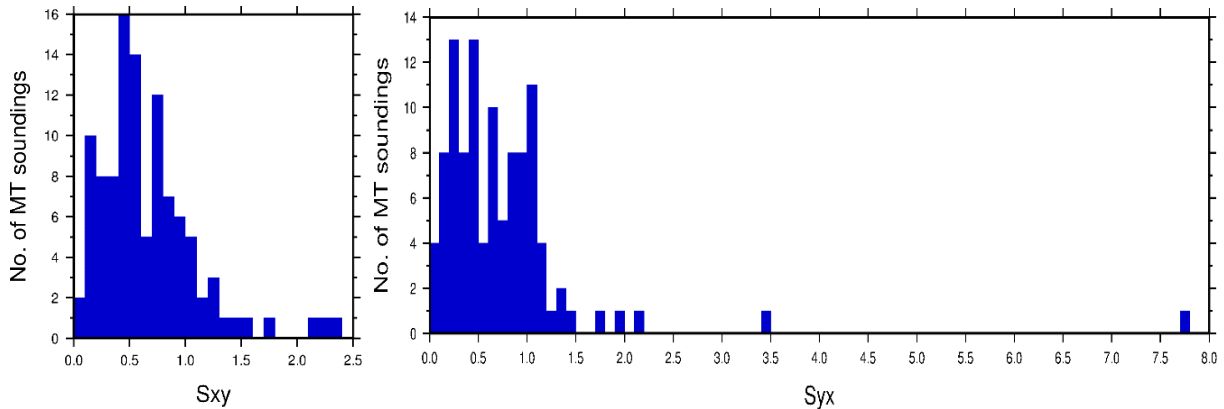


FIGURE 20: Histograms of the shift multipliers, S_{xy} and S_{yx} for the 105 MT soundings used in the MT 3-D inversion

7.3.3 Model mesh grid design for 3-D inversion

The realisation of the 3-D model goes with the decision and building of 3-D grid mesh. The model mesh grid is set out in such a way that the dense part of the grid covers the main area of data coverage. In designing the mesh a trade-off is required between the size of the grid and the computational time, it would require obtaining reasonable solutions to the models. The finer the grid the larger the time and memory resource required. Forward modelling solutions depend significantly on the mesh grid discretization used. The 3-D model consists of resistivity cubes built in the internal coordinate system generated from UTM coordinate system used during data collection. The grid was designed in such a way that its origin coincides approximately with the centre of survey area covered by the data (Figure 21). The x-axis is pointing towards N50°W and the y-axis is pointing towards N140°W (anticlockwise rotation). The mesh is built up with 52 vertical grid planes (2 edges and 50 internal planes perpendicular to the x-axis) in x-direction, 52 vertical grid planes (2 edges and 50 internal planes) in the y-direction and 32 horizontal grid planes (surface, bottom and 30 horizontal internal planes). The grid design was

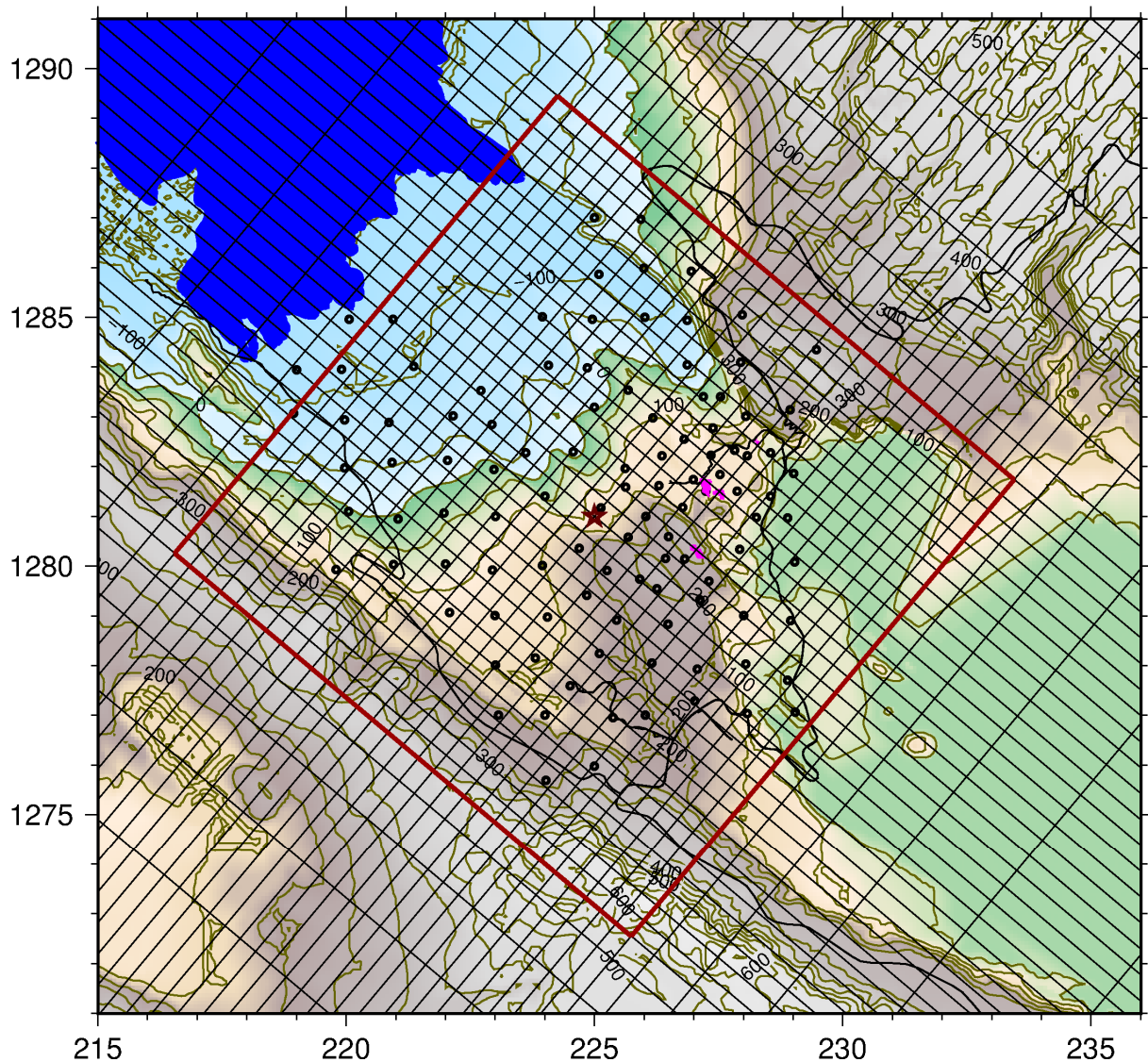


FIGURE 21: Horizontal slice showing vertical grid planes in the central part of the grid mesh for 3-D inversion. The heavy red lines mark the fine grid and within it the thin lines mark a 400 m x 400 m grid. A total of 105 MT soundings are shown as black circles. Thin grey lines: topographic contour lines in m a.s.l. Coordinates are UTM coordinates, zone 38N; WGS84 datum. North is up. Distances are given in km

made by considering the area of interest and high data coverage where it is considerably dense with 400 m grid spacing in the range of ± 6.2 km in the x-direction (NW-SE) and ± 6.2 km in the y-direction (NE-SW). Horizontally, the grid spacing increases exponentially outside the dense area (central part of the model) to the edges at ± 131.2 km and ± 131.2 km in the x and y-directions respectively. The shallowest layer thicknesses are 2, 4, 8, 16, 26, 36, 50, 76, 100, 158, 200, 300, 500 m etc. In z-direction, the grid spacing at shallow layers is small and increases exponentially with depth down to the bottom at 108.8 km.

7.3.4 Modelling parameters and initial models

The choice of model grid in the 3-D inversion was $M = 52 \times 52 \times 32 = 86528$ for x, y and z respectively. In the principle, the forward modelling problem considers this number to be unknowns. The normal technique of solving the inverse problem in the model-space will generate a tremendous computational problem. Therefore, to reduce the work and come up with attainable computation cost which can be accommodated by the available memory storage; the problem was instead reduced in data space 3-D inversion of $N=105$ (soundings) x 31 (periods) x 4 (impedance responses) equivalent to 13020. The

inversion program was executed using a parallel processing version of the WSINV3DMT code using the Message Passing Interface (MPI) parallel computing environment (Siripunvaraporn and Egbert, 2009). In the process, some components of the prior model can in some cases be assumed to be known a priori and fixed in the inversion. In our study area, Asal rift; the proximity of the sea has to be taken into account. Based on bathymetry, the resistivity of the model cells in the sea (Red Sea) and Lake Asal were assigned the average resistivity of seawater ($0.1 \Omega\text{m}$) and this was kept constant during the inversion.

This heavy computational task was performed on a special machine cluster at ÍSOR running on 32 cores and 128 GB of memory storage specific for handling such kind of big data set. Three different initial models were considered for the 3-D inversion and the data misfit was evaluated as the RMS (Root-Mean-Square) of the difference between the measured and calculated values, weighted by the variance of the measured values. The first initial model was compiled from the 1-D layered models interpolated from joint 1-D TEM and MT joint inversion. The initial RMS for this starting model was 6.5080 reducing to 1.4468 after four runs. The second case was $10 \Omega\text{m}$ homogeneous half-space initial model. This was considered to be low resistivity structure where the inversion tries to recover higher resistivity structures where necessary. The initial RMS misfit was 4.8327 and the final misfit was 1.4845 after four runs. For $50 \Omega\text{m}$ homogeneous half-space initial model which used as the third case, the initial RMS misfit was 61.8788 and the final misfit was 1.874 after five runs. Contrary to the second case of $10 \Omega\text{m}$; the $50 \Omega\text{m}$ homogeneous half-space initial was intended to reproduce the high resistivity structures and allow the inversion to insert lower resistivity structures where required. Each run counted five iterations for run and restarted with the best model from the previous run as initial and prior model. The stepwise inversion and relaxation of prior model continued until the data fit could not be improved any more. To run one round took about 50 hours and the whole work of computing took about 550 hours. At the end of calculations, in all cases using different initial models the measured data are well fitted as shown by a couple of examples given in Figure 22, while the data fit for all the 105 MT soundings is given in Appendix A of this report.

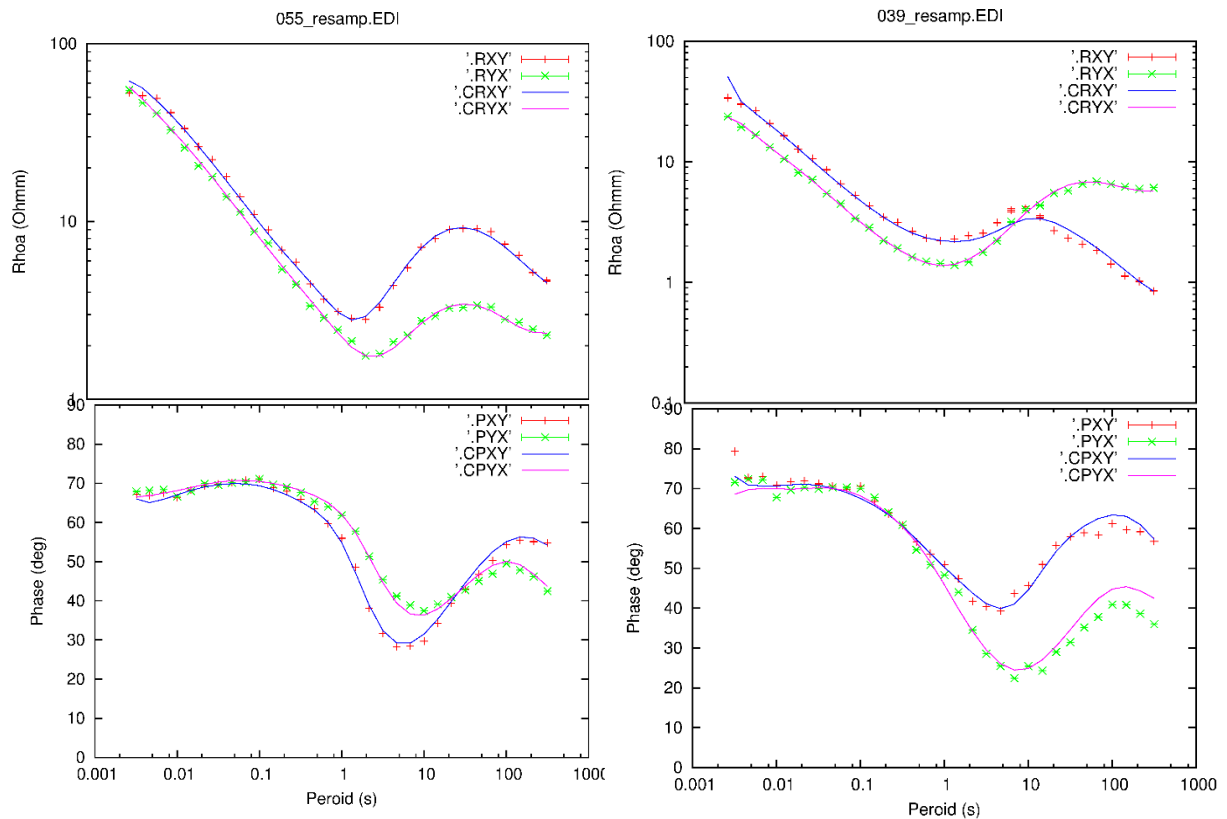


FIGURE 22: Data fit given as example for MT 055 and MT 039: A comparison of the (re-sampled) processed data (dots) for two soundings presented as apparent resistivity, phase and calculated response of the final model as result from the inversion (unbroken lines)

7.4 Presentation of 3-D inversion results

The final model resulting from the 3-D inversion of MT resistivity data is presented here in this project in two different ways; resistivity maps (contour plots) drawn at different elevations starting from the surface (sea level) and resistivity cross-sections taken in different directions of the field for studying in details the resistivity anomalies within the Asal geothermal area. This exercise is applied to the final model of the 3-D inversion generated from three different initial models as discussed in Section 7.3.4 for comparison purpose.

In Figure 23, an example of the final model of the inversion based on the 10 Ωm homogeneous half space initial model is shown; it is a presentation of a raw model (mosaic) displaying the resistivity in each cell of the model. As the inversion code (WSINV3DMT) doesn't consider the topography but assumes flat topographic surface; the cross-section presented here (Figure 23) was drawn regardless of the topographic changes. MT data are corrected for static shift, the correction removes topographic effects in the data; the depths below each model cell were converted to meters above sea level. The topography (current distortion due to the topography) is one of the reasons for the static shift problem in MT soundings as discussed earlier in Section 4.2.

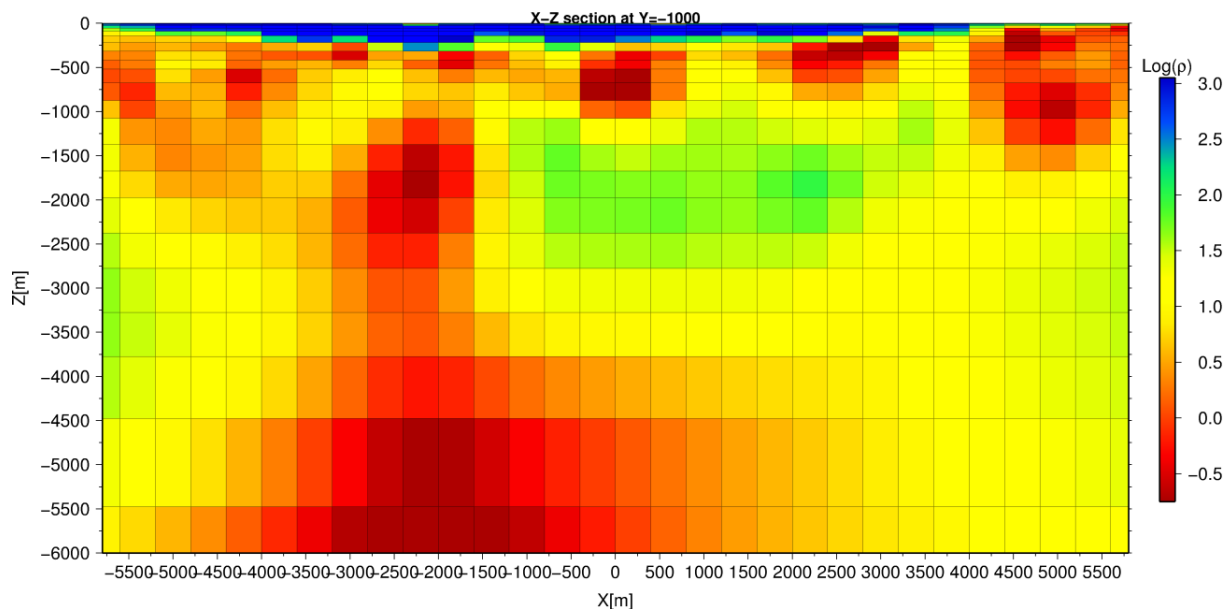


FIGURE 23: Raw model, resistivity cross-section along x-axis (NS-E) at $y = 1000$ m. Initial model: Homogeneous earth of resistivity 10 Ωm . See Figure 38 (a) for location

7.4.1 Initial models and their respective outcomes

The choice of three different initial models which are used in this project aims at understanding clearly the area of interest by taking a close look at the 3-D resistivity structure through different initial models. It is important to study the correlation patterns and to evaluate the constraints on the resulting 3-D resistivity model. For testing the final model; we have preferred first to run the inversion with the initial model compiled from the 1-D layered model, secondly with 10 Ωm homogeneous half-space initial model and lastly with 50 Ωm homogeneous half-space initial model. In all three cases, the models generated are showing particular similarities in terms of resistivity anomalies which makes the final model the most reliable one.

The example given in Figure 24 (a) - (c) compares the resistivity anomalies identified by 3-D inversion in three different cases. The resistivity anomalies shown by resistivity maps drawn at sea level are similar in all three cases which justify the total agreement in three initial models where the high resistivity is dominating the NW part as moving to Lake Asal and SE part of the Asal rift. The low resistivity layer at the surface is extending from NE and covering the volcano area and the zone of

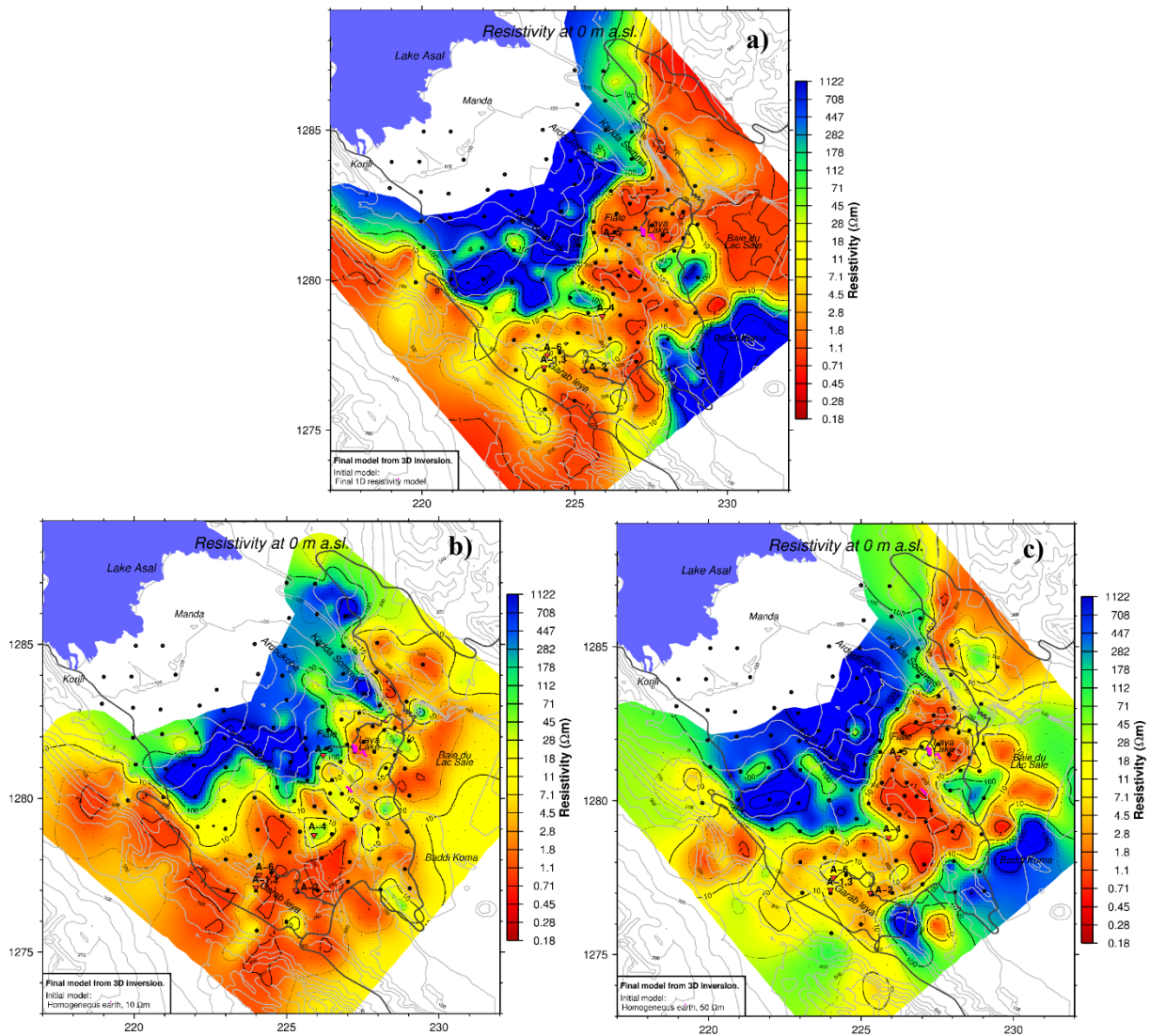


FIGURE 24: Resistivity maps at sea level showing comparison of the results from different initial models: (a) model compiled from 1-D inversion, (b) homogeneous 10 Ωm half space and (c) homogeneous 50 Ωm half space initial model. Thin grey lines: topographic contour lines in m a.s.l. Red triangles show boreholes and surface manifestations are shown in purple. Coordinates are UTM coordinates, zone 38N; WGS84 datum. North is up. Distances are given in km

surface geothermal manifestations to the SW of Asal rift. At 500 m b.s.l, the models are showing the decrease in resistivity where the conductive layer is covering almost the whole study area, some exceptions are located in central parts where the resistivity is comparatively higher. The iso-depth resistivity maps drawn at 1500 m b.s.l (Figure 25) the resistivity is slightly increasing with some conductive spots in central parts of the study area.

Figures 26 and 27 show examples of resistivity cross-sections reproduced from 3-D inversion with different initial models, a) compiled from 1-D inversion, b) from homogeneous 10 Ωm half space, and c) from homogeneous 50 Ωm half space.

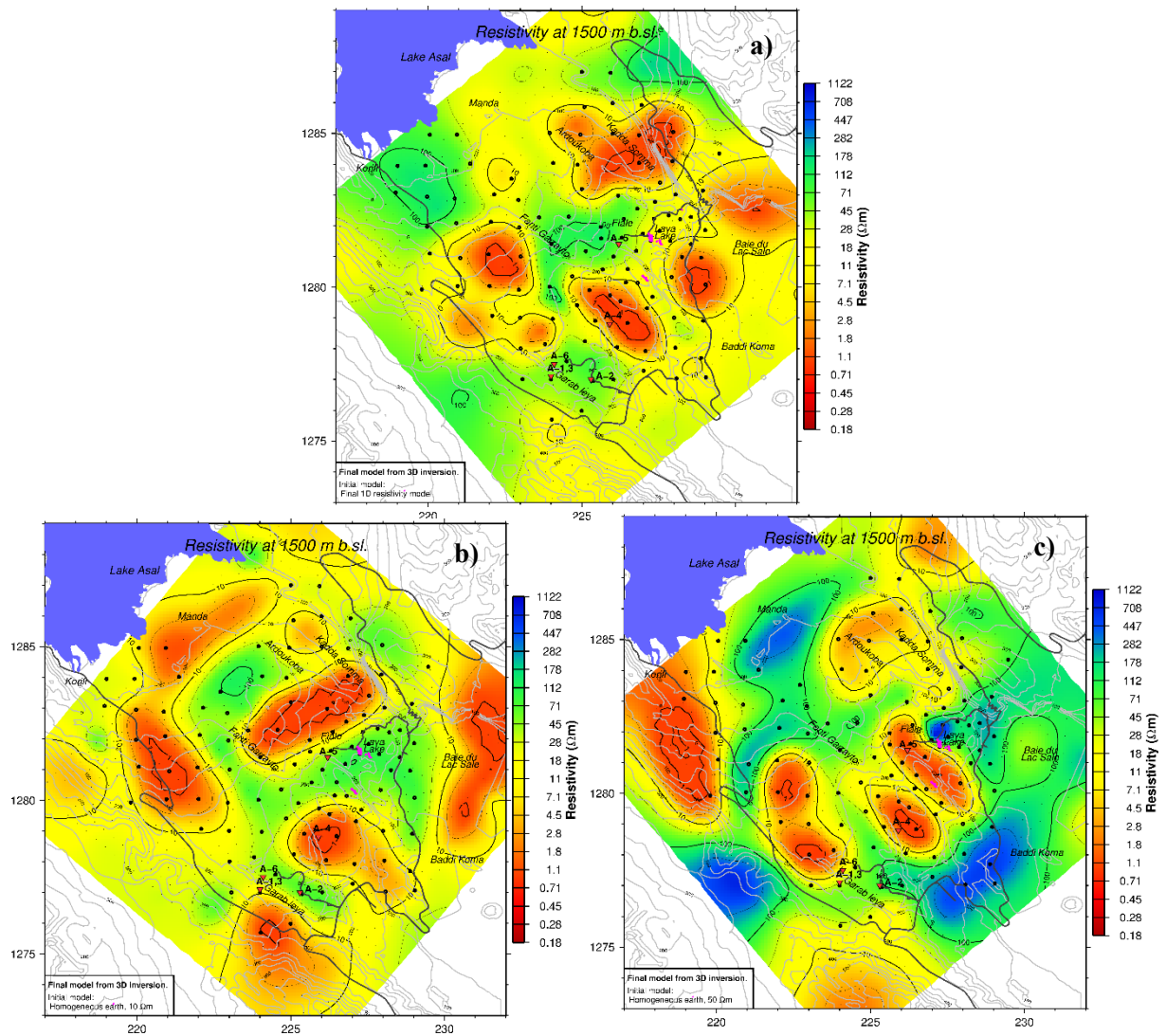


FIGURE 25: Resistivity maps at 1500 m b.s.l. showing comparison of the results from different initial models: (a) model compiled from 1-D inversion, (b) homogeneous 10 Ωm half space and (c) homogeneous 50 Ωm half space initial model. For legend, see Figure 24

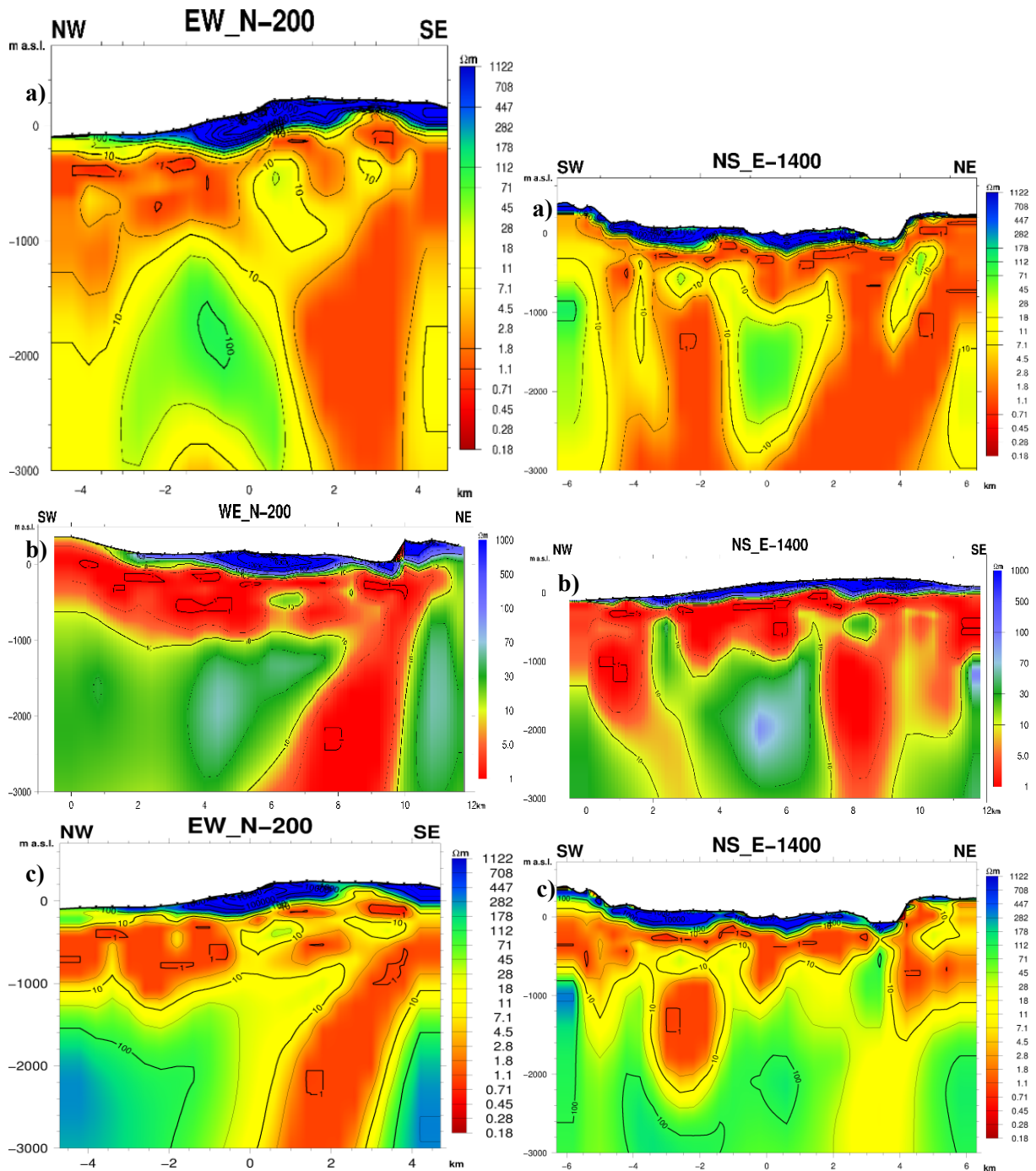


FIGURE 27: Resistivity cross-sections EW-N reproduced from 3-D inversion with different initial models: (a) model compiled from 1-D inversion, (b) homogeneous 10 Ωm half space and (c) homogeneous 50 Ωm half space initial model. The location on map is shown on Figure 39(a).

FIGURE 27: Resistivity cross-sections NS-E reproduced from 3-D inversion with different initial models: (a) model compiled from 1-D inversion, (b) homogeneous 10 Ωm half space and (c) homogeneous 50 Ωm half space initial model. The location on map is shown on Figure 38(a)

7.4.2 Iso-depth resistivity maps produced from 3-D inversion

The iso-depth resistivity maps are presented from sea level down to 10,000 m b.s.l. after elevation correction. Only a small number of the iso-depth resistivity maps are presented here and were produced based on homogeneous 10 Ωm initial model. More iso-depth resistivity maps are presented in Appendix B in this report and the landmarks are provided in Figure 24.

At sea level (Figure 28) high resistivity dominates the NW part of Asal rift towards Lake Asal in the vicinity of Ardoukoba volcano and the SE part of the rift around Baddikoma region. An updoming conductive cap intersects the high resistivity, running NE-SW and reflects presumably alteration within the geothermal system. It covers the central part of the Asal rift including the Fiale explosion crater (Lava Lake). This is the area where the fumaroles and hot springs in Asal rift are located.

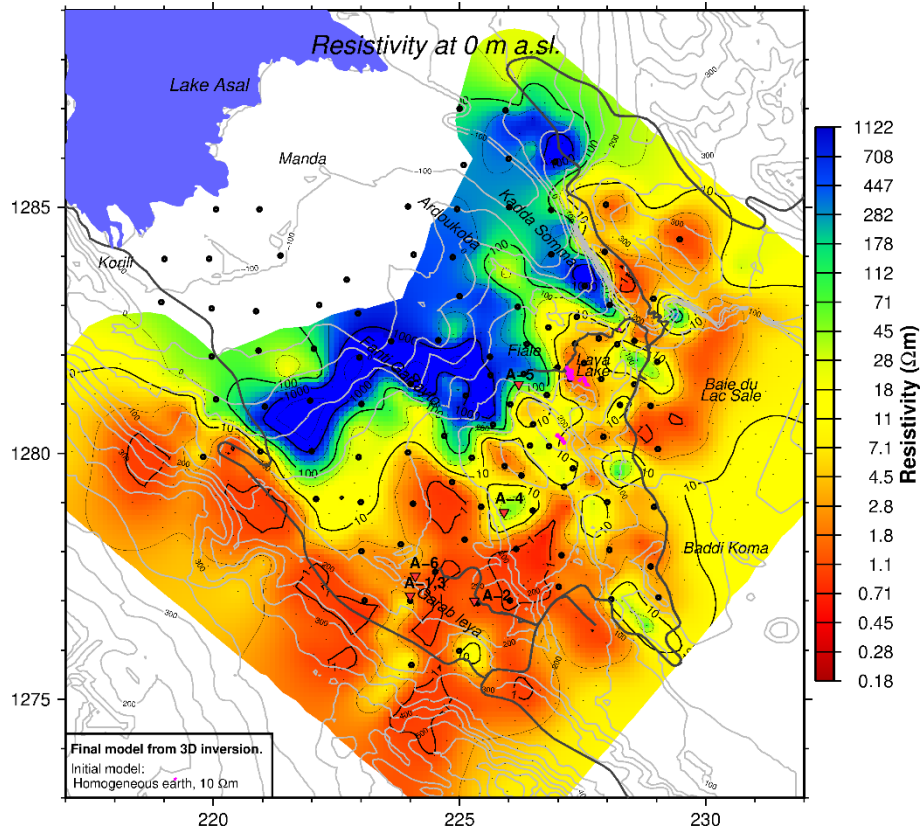


FIGURE 28: Iso-depth resistivity map at sea level: 3-D model produced from homogeneous 10 Ωm half space initial model. For legend, see Figure 24

At 100 m b.s.l. (Figure 29), the iso-map doesn't show a big difference from the previous one in terms of resistivity distribution. At this level only the part that was appearing resistive at sea level close to Lake Asal is getting much smaller. This confirms that the resistive layer appearing on the surface persists only at shallow depth less than 200 m.

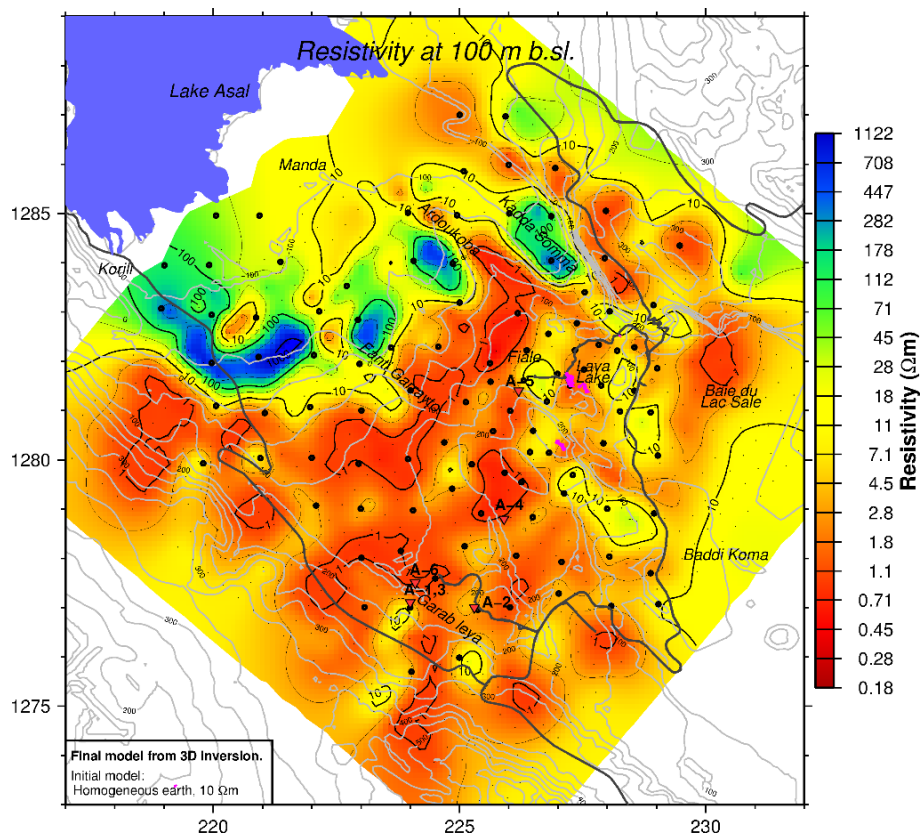


FIGURE 29: Resistivity map at 100 m b.s.l. For legend, see Figure 24

At 500 m b.s.l. (Figure 30), the resistivity is low within the whole Asal rift. It is only increasing slightly in the central part where some spots close to the Lava Lake area are observed and also within the area

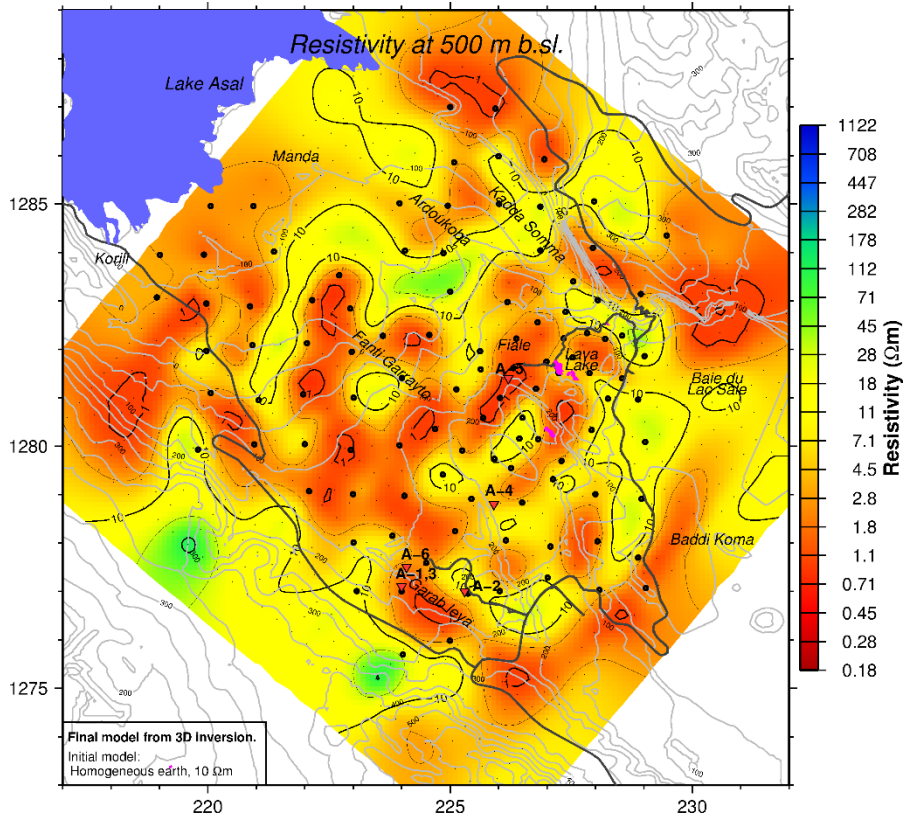


FIGURE 30: Resistivity map at 500 m b.s.l. For legend, see Figure 24

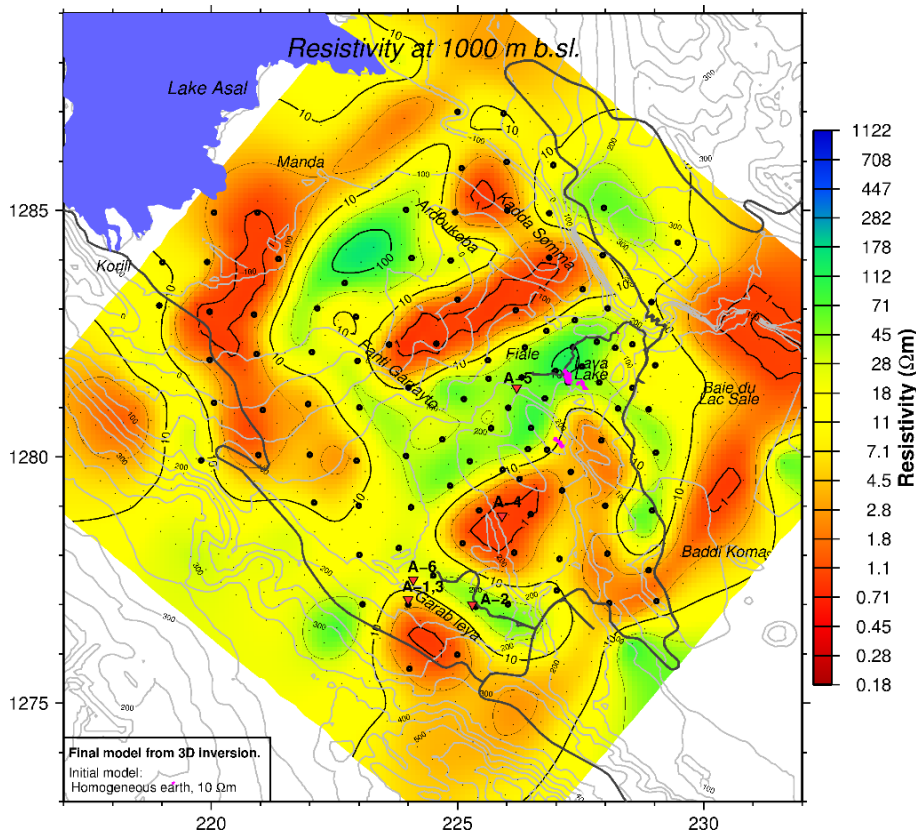


FIGURE 31: Resistivity map at 1000 m b.s.l. For legend, see Figure 24

surrounding the platform of well Asal-1, 2, 3 and 6 presenting the increase of resistivity as detailed by the 3-D model.

At 1000 m b.s.l. (Figure 31), the resistivity is increasing slightly along the Asal rift. Low resistivity spots are observed in the central part of the rift and forming a ring surrounding the Fiale area and including the area below well Asal-4 and the Ardoukoba volcano.

At 2500 m b.s.l. (Figure 32), a low resistivity anomaly is dominant to the NE below the Ardoukoba volcano area and it connects the low resistivity anomaly to the SW. A low resistivity anomaly is also seen below well Asal-4. In general, the decrease in resistivity values is observed all around the rift and decreases with depth.

At 3500 m b.s.l. (Figure 33), the low resistivity anomaly observed to the NE below the Ardoukoba volcano area is extending and connects completely to the low resistivity anomaly in the SW part covering the Fiale explosion crater (Lava Lake) and including the area under well Asal-5. The same low resistivity anomaly is also connected to the area below well Asal-4 to the SE of the rift as

well as the east part of the Lake Asal.

At 4500 m b.s.l. (Figure 34), the low resistivity becomes clearer by connecting all the low resistivity spots of different corners of Asal rift. The central part of the rift below Fanti Garrayto is dominated by the low resistivity which extends to the NE and SW. The area to the SW and SE of the low resistivity has comparatively lowest resistivity, this is where most of the wells around Lava Lake, Fiale and Garab leya (Asal-1, 2, 3, 5 and 6) are located.

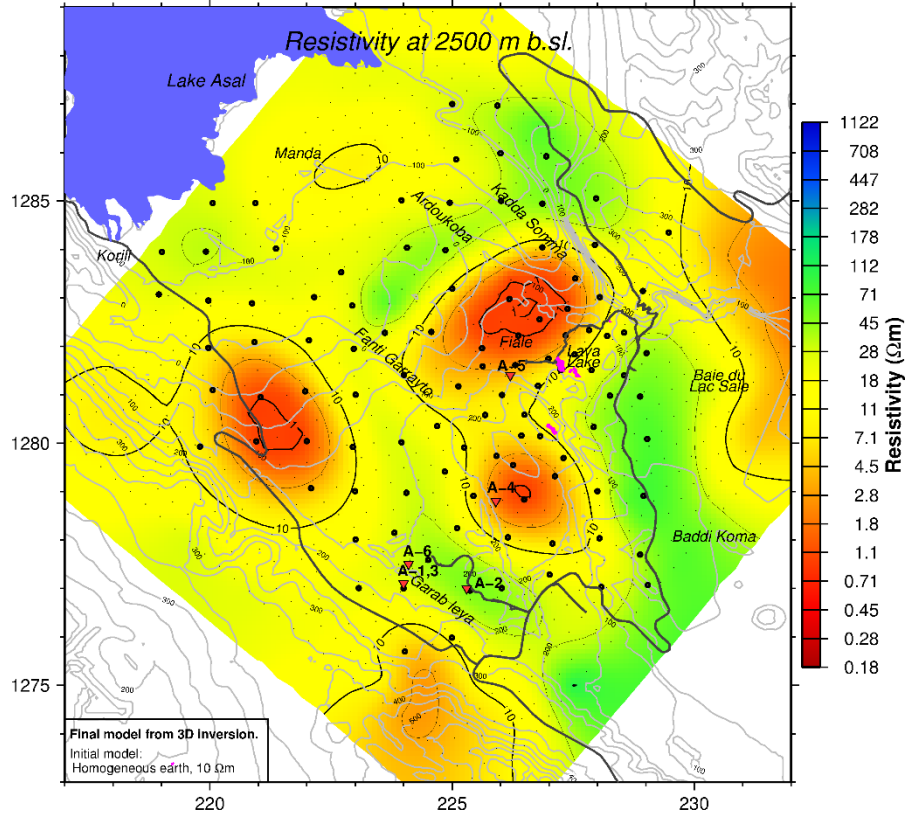


FIGURE 32: Resistivity map at 2500 m b.s.l. For legend, see Figure 24

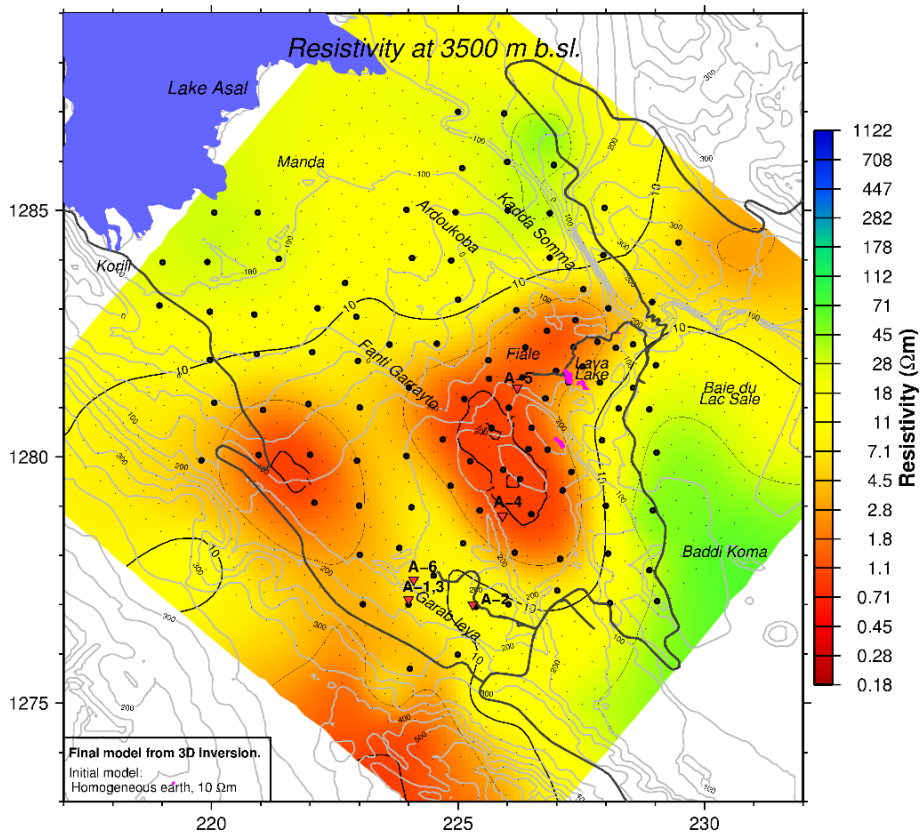


FIGURE 33: Resistivity map at 3500 m b.s.l. For legend, see Figure 24

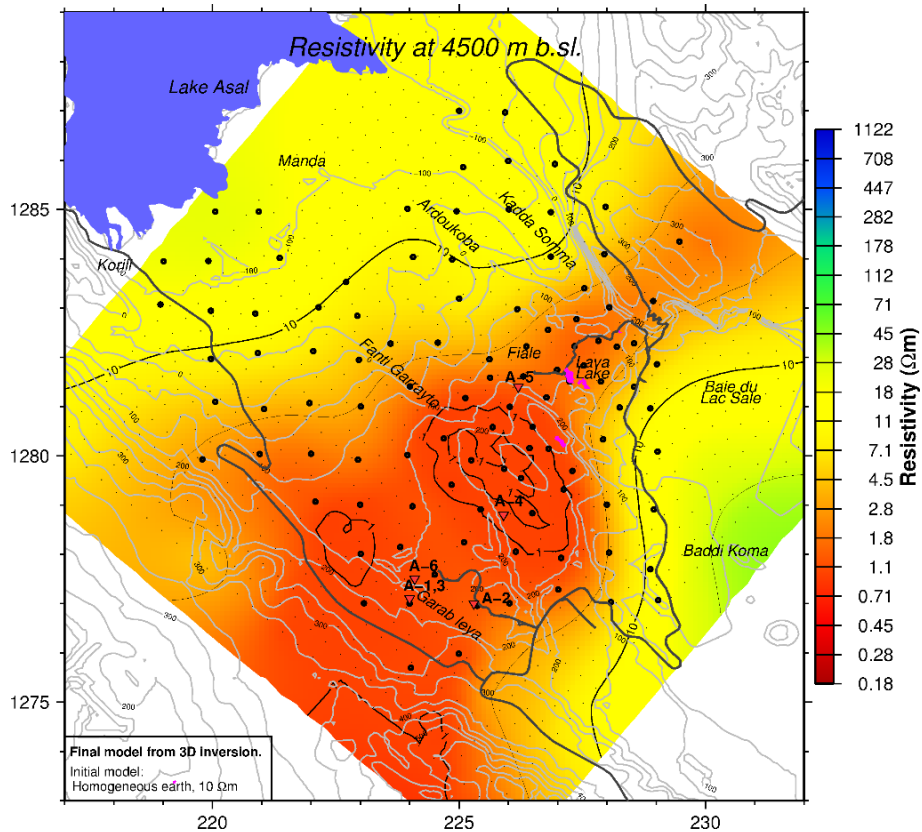


FIGURE 34: Resistivity map at 4500 m b.s.l. For legend, see Figure 24

Comparison of 3-D inversion and 1-D inversion (Iso-depth resistivity maps)

The results from 3-D inversion based on different initial models have shown that they are in quite good agreement which allows us to consider one 3-D model generated by the 10 Ωm homogeneous half-space initial model and the 1-D model as presented by Árnason et al. (2008). Figure 35 compares the resistivity map produced from the 3-D inversion at sea level and the resistivity map generated from the 1-D inversion at the same depth. At the surface, the high resistivity layer which characterises the Asal geothermal area and most of the geothermal areas in general is observed in both models (1-D and 3-D). The only difference is the smoothed appearance in the 1-D model and detailed resistivity structures given by the 3-D model. This can be justified by the fact that 1-D inversion gives results for each sounding and doesn't resolve the volume between the MT soundings.

Figure 36 shows the comparison between the resistivity map produced from 3-D inversion at 500 m b.s.l. and the resistivity map generated from the 1-D inversion at the same level. All models reveal a clear picture of the low resistivity cap but more constraints and the details are observed in the 3-D model without considering the artefacts provided by 3-D models outside the data coverage.

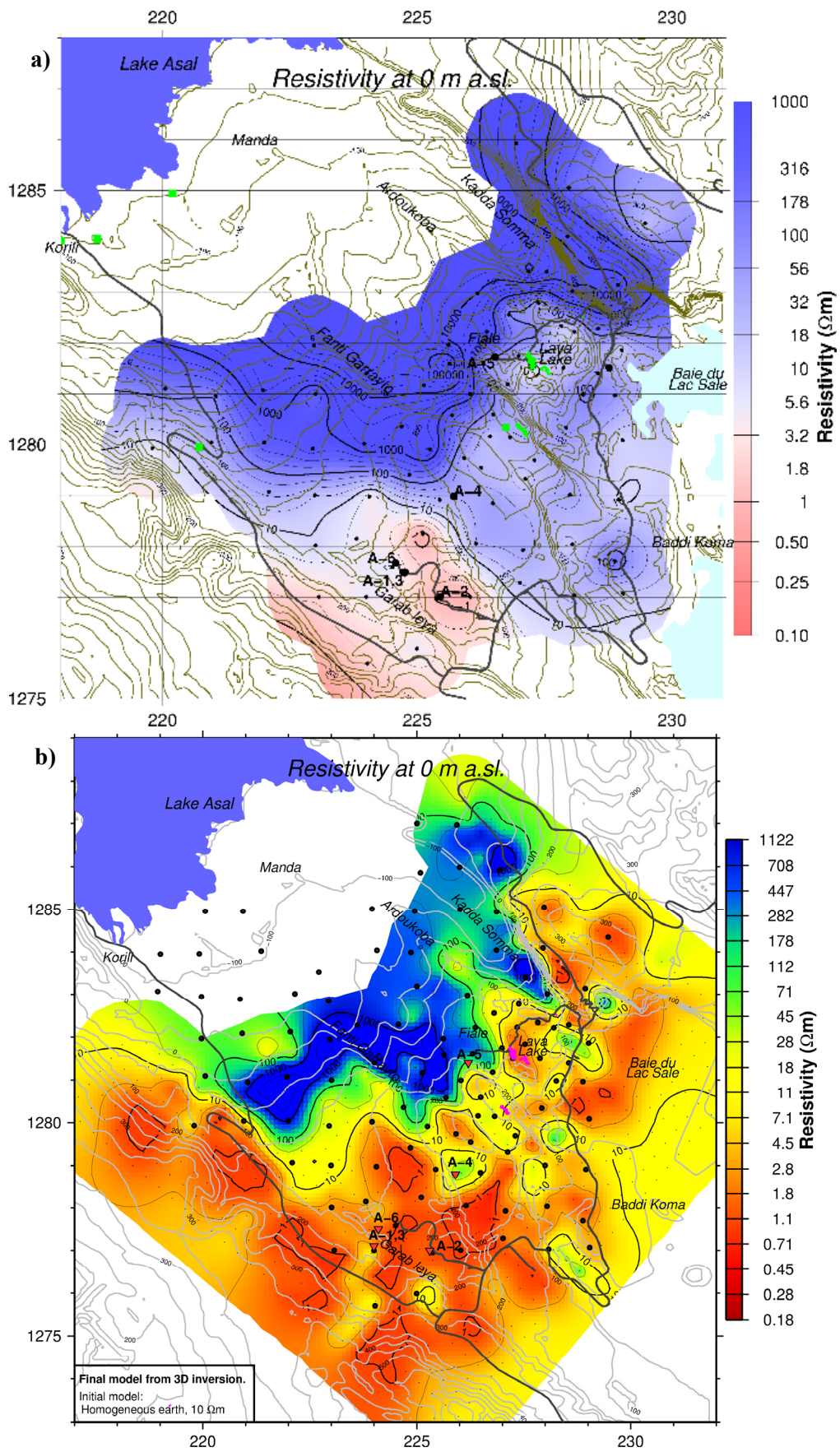


FIGURE 35: Resistivity models at sea level: 1-D inversion (a) (Árnason et al., 2008) compared to 3-D model using homogeneous 10 Ωm half space as initial model (b). For legend, see Figure 24

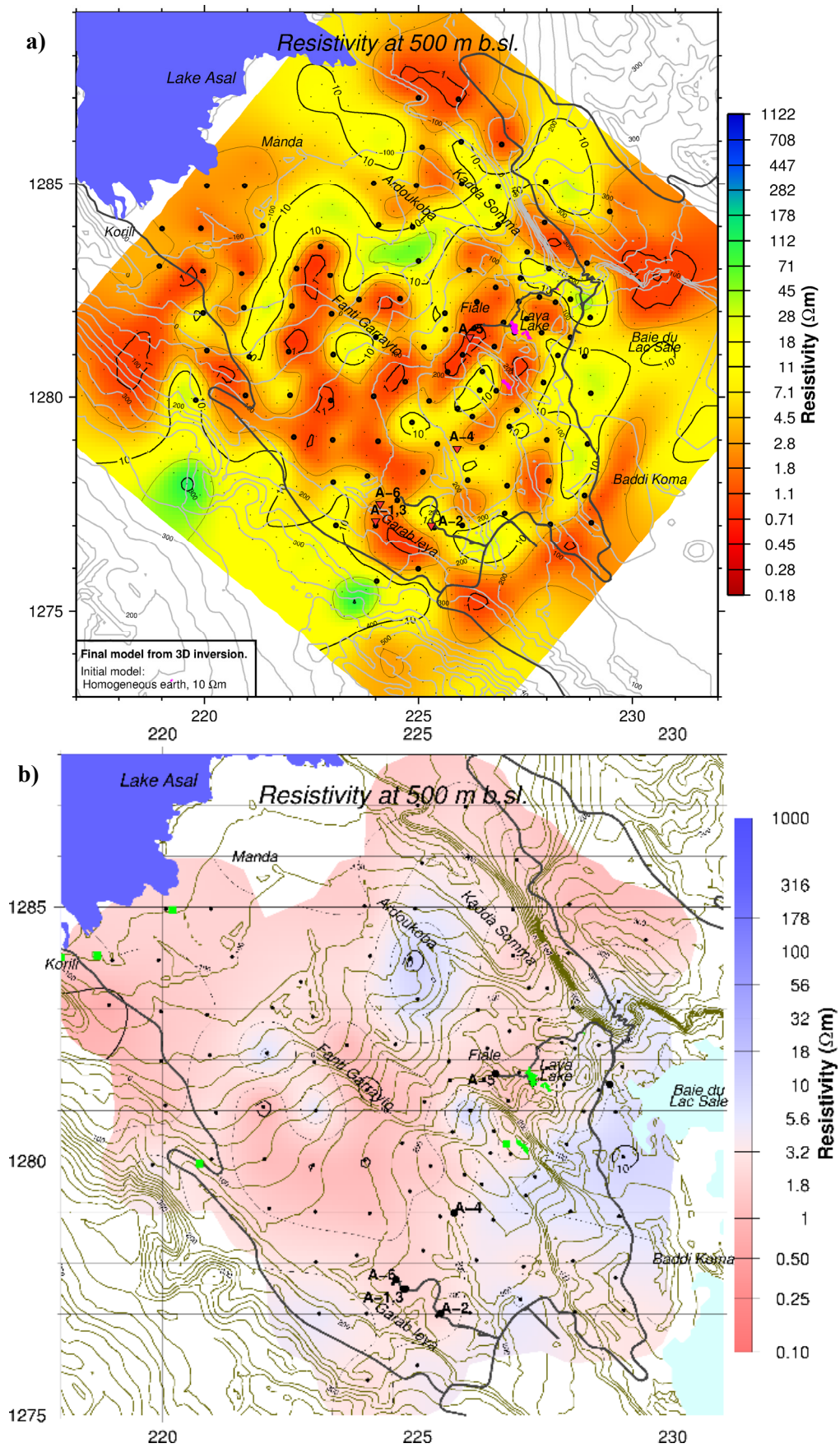


FIGURE 36: Resistivity models at 500 b.s.l.: 3-D model using homogeneous 10 Ωm half space as initial model (a) compared to 1-D inversion (b) (Árnason et al., 2008). For legend, see Figure 24

Comparison of 3-D and 1-D inversion (resistivity cross-sections)

In this section, the emphasis is on the comparison between the resistivity cross-sections based on 1-D inversion from the previous resistivity survey (Árnason et al., 2008) and the resistivity cross-sections presented based on the 3-D inversion. The 3-D inversion has the particularity of showing clearly, detailed and precisely resistivity resolution when compared to the 1-D inversion. In the sections presented here in Figure 37, the same shallow resistivity cap followed by the low resistive layer is observed in both sections. The resistivity is then increased at around 2000 m depth and below a deep seated conductive cap is found presumably reflecting the heat source of the system.

7.4.3 Resistivity cross-sections produced from 3-D inversion

For better understanding the resistivity structures and observing the detailed resistivity within the Asal geothermal area; the resistivity cross-sections produced from 3-D inversion were drawn in two main orthogonal directions in the area of interest based on the fissure swarms orientations within Asal rift. The vertical cross-sections presented in this project are oriented either perpendicular or parallel to the Asal rift. The vertical cross-sections presented here are drawn along the rift NS-E (Figure 38: NS_E200 (b), NS_E1800 (c) and NS_E-3000 (d) and perpendicular to fissure swarms, NE-SW in the rift (Figure 39: EW_N-1000 (b), EW_N2600 (c) and EW_N-2200(d). More cross-sections as presented in Appendix C in the report.

All the resistivity cross-sections show the same general resistivity structure particular for high geothermal fields of a volcanic area. A shallow lying thin high resistivity layer ($> 75 \Omega\text{m}$) followed by low resistivity (conductive cap; $< 1 \Omega\text{m}$). Below there is a high resistivity layer (resistive core) underlain by a deep lying conductor. Lithology based on well data shows that the shallow thin high resistivity layer corresponds to dry basaltic rocks covering the surface, the conductive layer reflects saline fluids but correlates also with low temperature alteration (smectite and zeolites), the deep resistive core correlates with the high temperature alteration minerals (chlorite and epidote).

At great depths, a prominent low resistive cap is observed and it is probably reflecting the heat source of the geothermal system underneath the Asal rift. Figure 38 (c) and (d) is clearly showing the deeper lying conductive lineament connecting to shallow resistivity layer. It could be the same confirmation of a shallow basaltic magma chamber below Fiale explosion crater (Lava Lake) between 2000 and 5000 m depth as discussed in Vergne et al. (2012).

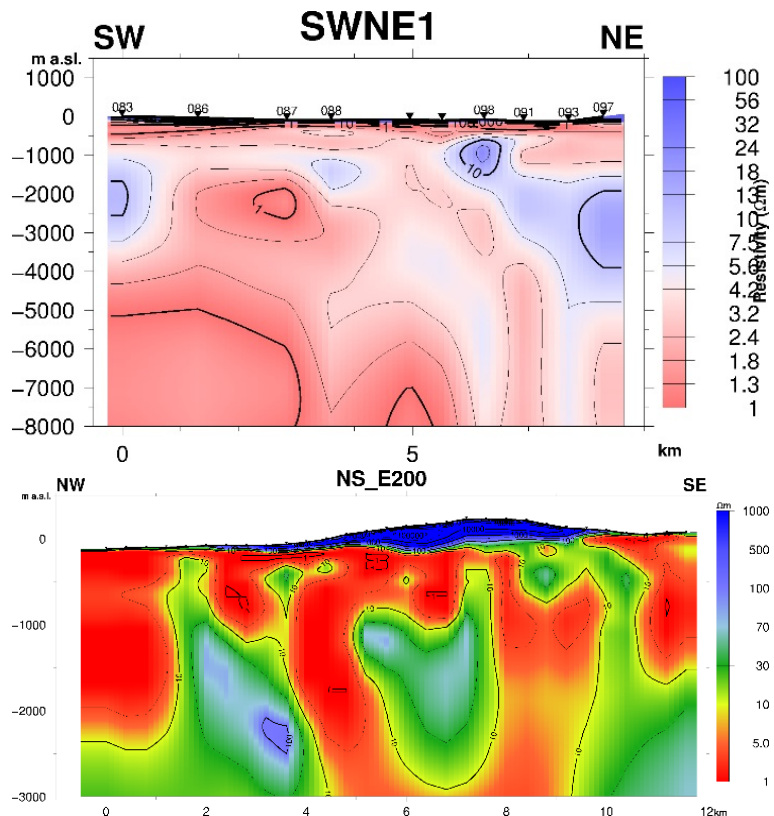


FIGURE 37: Comparison between resistivity cross-sections generated from 1-D inversion (top) and 3-D inversion (bottom)

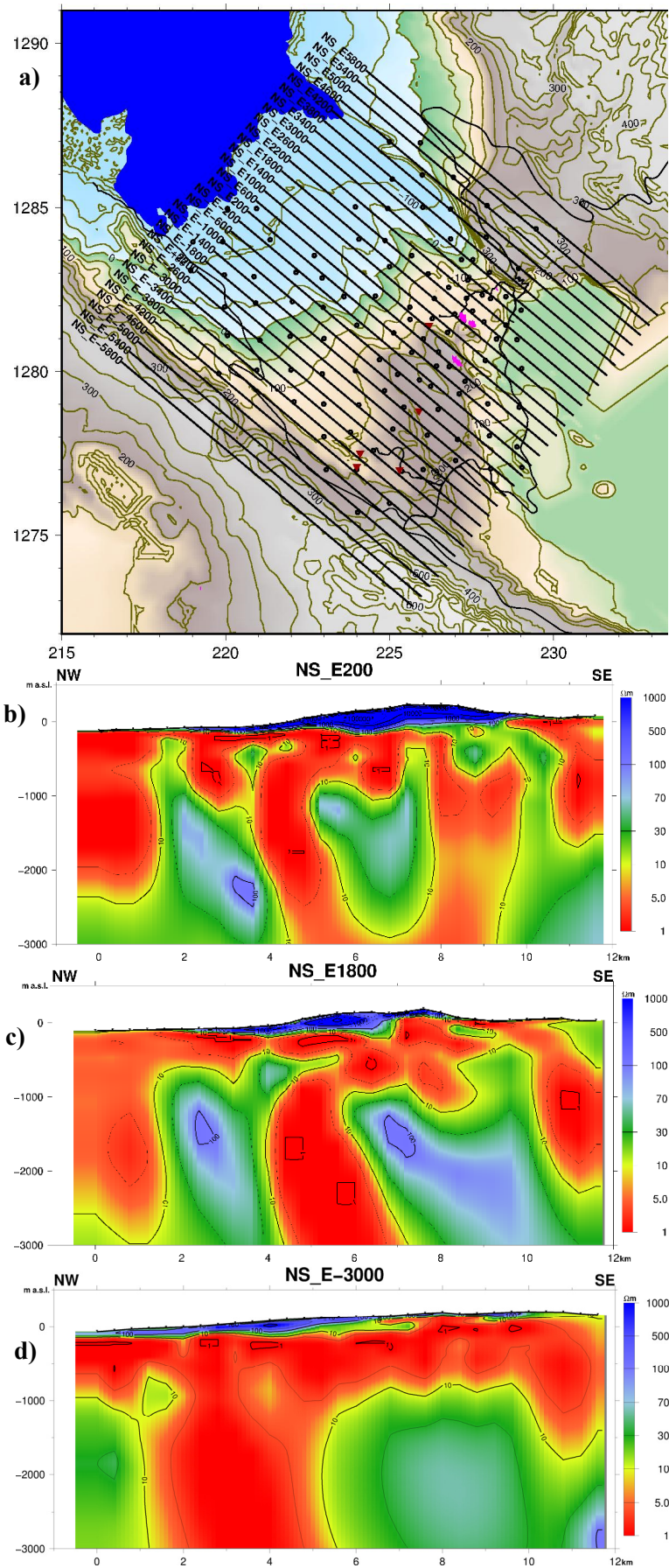


FIGURE 38: Resistivity cross-sections along the Asal rift; parallel to x-axis of the internal coordinate system; NS_E200 (b) to NS_E1800 (c) and NS_E-3000(d). The map (a) is showing the location of the cross-sections drawn along the Asal rift. For legend, see Figure 24

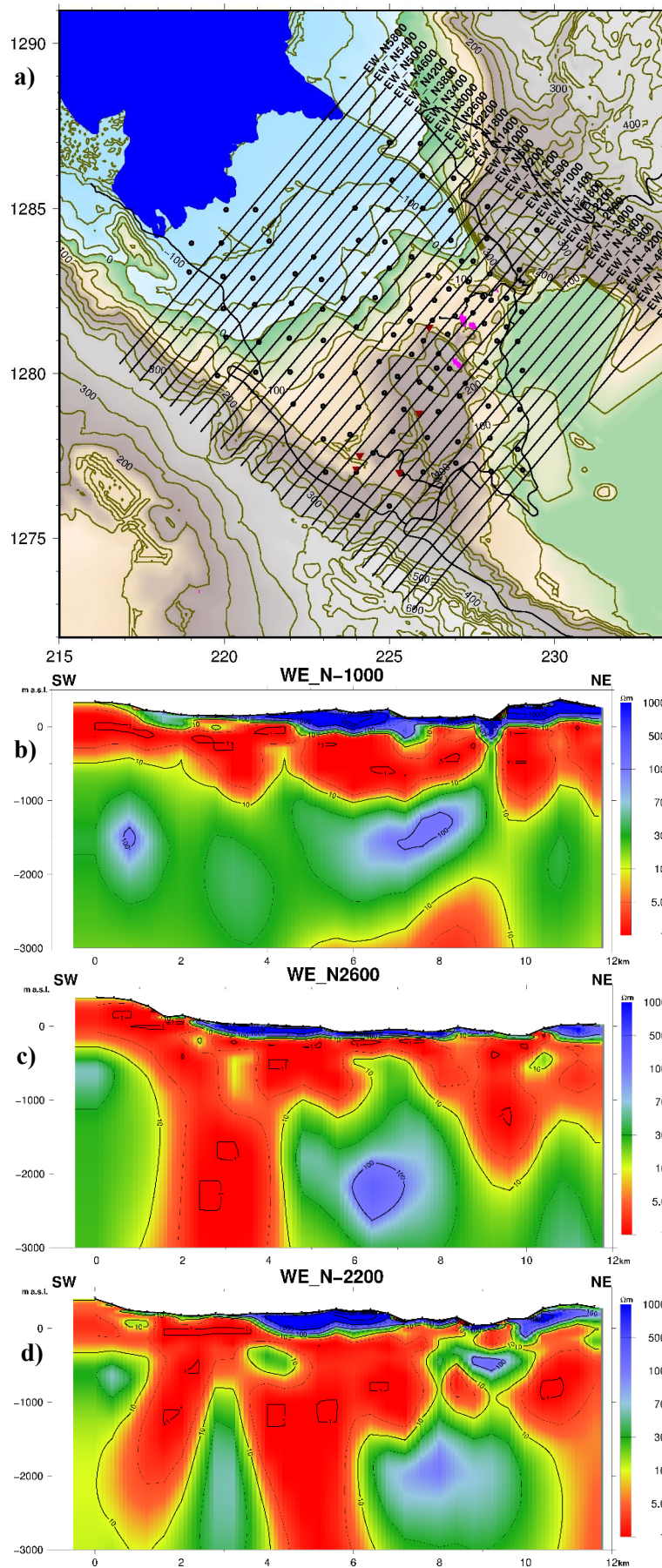


FIGURE 39: Resistivity cross-sections across the Asal rift; parallel to y-axis of the internal coordinate system; EW_N-1000 (b) to EW_N-2600 (c) and EW_N-2200 (d). The map (a) is showing the location of the cross-sections drawn along the Asal rift. For legend, see Figure 24

Discussion of the 3-D inversion

The 3-D inversion of MT data was presented as iso-depth resistivity maps and resistivity cross-sections (Figures 28-34 and Figures 38-39). Due to the quality of MT data, it was possible to achieve a good resolution at great depths. The resistivity structure within and underneath the Asal rift is characterized mainly by four resistivity layers as shown by the iso-depth resistivity maps and cross-sections drawn to 10000 m. A high resistivity and thin surface layer is linked to the younger basaltic lava as observed along the vertical cross-sections drawn across and along the Asal rift. The low resistivity anomaly at sea level linked to the geothermal surface manifestations is observed around Fiale explosion crater (Lava Lake), it is also observed at the well field (Asal-1, 2, 3 and 6). The low resistivity layer is underlain at shallow depth around 1000 m by resistivity values varying from 0.7 to 28 Ωm . It is mostly attributed to low temperature alteration minerals. The underlain layer with relatively higher resistivity is linked to the change in alteration minerals to higher temperature mineralogy underneath Lake Asal particularly in the central area below Fiale explosion crater (Lava Lake) and spreading below the well field to the SW of Asal rift. It is seen from deep resistivity cross-sections that a deeper lying conductive segment is at around 4000 m depth. It is quite dominating and prominent in most of the sections and could be linked to the presence of partial melt. It could be interpreted as the heat source of the geothermal system within the Asal rift. At the greater depths (450 m to 1000 m) the low resistivity layer is spreading all below the Asal rift where the NE and SW parts of Asal rift are showing the small difference in increase in terms of resistivity values.

7.5 Geological/geothermal interpretation of 3-D resistivity model of Asal rift

Geothermal exploration using the resistivity method in Asal rift has been successful and the resistivity structures found were interpreted and associated with existing geological formation as well as surface geothermal manifestations (hot spring and fumaroles) which are basically connected to volcanic activities. The detailed resistivity model of Asal geothermal field was generated from 3-D inversion of MT data. The model is revealing the typical resistivity structure for high temperature geothermal field similar to other geothermal fields of similar geological formation. Generally speaking, the resistivity structure is characterised by low resistivity cap underlain by a resistive core which is in most cases interpreted to be the host of the geothermal reservoir of the system (Árnason et al., 2000).

By comparing the well data with the observed resistivity structures at depths below Asal rift; the shallow low resistivity layer is matching with the beginning of thermal alteration (smectite and zeolites) which is found between 250 m and 450 m depth in well Asal-4 (Figure 40). This is the zone above water table where the rocks at this layer are partially saturated. Below water table, the resistivity is decreasing due to the influence of saline groundwater. The resistivity structures of Asal rift at sea level are also distinguished by the elevation differences. The NW part of the Asal rift, east of Lake Asal (-100 m) is characterized by the high resistive cap which is connected to dry rocks (basalts) found in the same zone. The Asal rift is very tectonically active with faults and fissures oriented mostly NW to SE within the rift. The low resistivity layer starts to vanish below 600 m and the resistivity increases again from the central part of the rift. The borehole data corresponds to the same layer with high temperature alteration

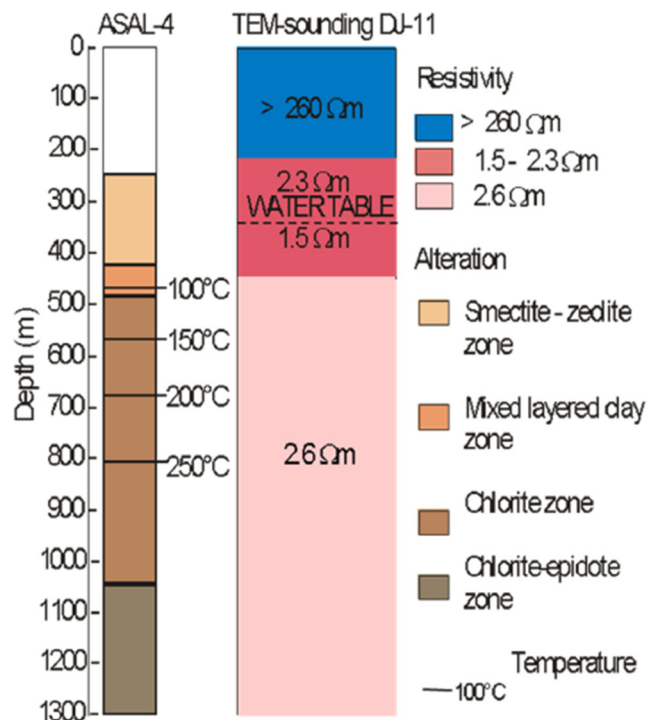


FIGURE 40: Alteration mineralogy in well Asal-4 and 1-D inversion of a nearby TEM sounding (Árnason et al., 2008)

minerals (chlorite and epidote) are overtaking the low temperature alteration minerals which are no longer controlling the resistivity changes at this depth (600-1000 m). The increase in mineral precipitation and reduced porosity could contribute to some extent to the increase of resistivity in the same zone. At deeper lying substructures, the resistivity is normally increasing with the exception of the low resistivity forming the ring beneath the zones surrounding Fiale explosion crater (Lava Lake) and running towards Ardoukoba volcano passing well Asal-4 area. When reaching a depth below 3000 m, the resistivity starts to decrease again and the low resistivity anomaly is highly dominant in the central part of the the Asal rift particularly in the East part of Lake Asal (Figure 35). This anomaly could be reflecting hypersaline fluid encountered by well Asal-1, 3 and 6 (Aqater, 1989). As discussed by Ngoc et al. (1981); the low resistivity found at greater depths of Asal rift could be the magmatic brine trapped below the ductile/brittle boundary at about 700°C. Most of the low resistivity anomalies found below the wells and especially to SE of Lake Asal have been attributed to the hypersaline, main characteristic of hydrothermal fluids in Asal rift.

In the subsurface, the factors that are affecting resistivity structures are different and vary from one field to another based on geological formation. The resistivity structures in Asal rift are comparable to high temperature geothermal fields in Iceland; the resistivity structure of pure basaltic crust which has been found in Iceland could be the example and taken as reference to understand the crust of Asal rift that has a lot of resemblances to the rift zones. The resistivity changes are depending on different factors including degree of water saturation, boiling point, porosity of the rock in the same zone, formation temperature, and salinity of the pore fluid and the stage of the alteration of the rock (Árnason et al., 1988). All the above mentioned factors are kept in mind when interpreting the resistivity model, however, it is sometimes hard to make a conclusion about the geological meaning of the resistivity structure by considering only the results provided by MT soundings. The available geological and geophysical data from the same area should be considered for a meaningful and comprehensive interpretation.

8. CONCLUSIONS AND RECOMMENDATIONS

A three-dimensional inversion of MT data and resistivity interpretation based on geological and geothermal for Asal geothermal rift was performed with two main objectives: to become acquainted with the resistivity method and different ways of performing interpretation of MT data for deep lying subsurface investigations. The MT data collected from Asal geothermal area were used; the comparison between the results of 1-D inversion carried out previously and 3-D inversion is performed. A total of 105 MT soundings were considered in this research project and the same number of corresponding TEM soundings collected at the nearby sites. To allow the static shift correction in the 1-D inversion, the MT data were jointly inverted with TEM data. Shift correction was then applied to the two polarizations for 3-D inversion. The modern computing systems has made 3-D modelling of MT data achievable and it is now becoming common and useful for detailed subsurface survey in geothermal industries as well as in other fields including ground water, oil and natural gas and mineral to become acquainted with the resistivity method and ways of using multidimensional interpretation of MT data for deep subsurface investigations and to use MT data from Asal geothermal area; compare previous 1-D inversion to 3-D results and characterize the reservoir through a conceptual model.

In order to achieve these objectives, an equal number of 105 MT and 105 TEM soundings were used. The data were jointly inverted in order to find out and correct the static shifts of MT soundings. The 3-D inversion was performed with the WSINV3DMT inversion code where 31 periods logarithmically distributed from 0.003 to 300 s were used. Three different initial models were used to test the robustness. The first initial model was compiled from the 1-D layered models interpolated from joint 1-D inversion of TEM and MT data. The second one was a 10 Ωm homogeneous half-space initial model. This was considered to be a low resistivity structure where the inversion tries to recover higher resistivity structures where necessary. The third initial model was a 50 Ωm homogeneous half-space that intended to reproduce the high resistivity structures and allow the inversion to insert lower resistivity structures where required. The RMS when running the three different initial models were not differ with values of 1.44, 1.48 and 1.87, respectively. The final models were compared and it was found out that they are giving similar resistivity structures underneath Asal rift. The correction of elevation was performed and the models presented as iso-depth resistivity maps and cross-sections.

The results from the three initial models show the same resistivity anomalies of Asal geothermal field (from sea level to 10000 m depth). The resistivity structure observed in Asal geothermal area might be fully correlated with the hydrothermal alteration mineralogy. There are four resistivity layers in most part of the area of interest observed from 3-D inversion and they correspond to the ones found out by 1-D inversion performed previously. A shallow lying thin high resistivity layer followed by low resistivity (conductive cap). Below there is a high resistivity layer (resistive core) underlain by a deep lying conductor. Lithology based on well data shows that the shallow thin high resistivity layer corresponds to dry basaltic rocks covering the surface, the conductive layer reflects saline fluids but correlates also with low temperature alteration (smectite and zeolites), the deep resistive core correlates with the high temperature alteration minerals (chlorite and epidote) whereas the deep seated conductive body is most likely connected to the heat source of the Asal geothermal system while the deep conductor may represent the partial melt, which could be reflecting the heat source for the geothermal system.

Geothermal exploration and development doesn't rely on results provided by a single method; it is recommended that the 3-D model provided in this research study based on 3-D inversion of MT resistivity data should be constrained with the latest results from other exploration methods for better understanding the Asal geothermal system. Further infill measurements are encouraged for the future geothermal resource development in Asal field (SW part of the rift). Seismic monitoring is recommended for monitoring the volcano activities in the Asal rift. The conceptual model should be reviewed and reconstructed with the latest gravity, magnetic and seismic results for better estimation of geothermal reservoir in Asal geothermal field. The results of this study should be compared to information from a new gravity survey, applying modern techniques and interpretation could give more reliable structure information and should be considered.

REFERENCES

- Aquater, 1989: *Djibouti geothermal exploration project, Republic of Djibouti. Final Report*. GEOT A3770, JOB 339400.
- Archie, G.E., 1942: Electrical resistivity log as an aid in determining some reservoir characteristics. *Trans., AIME*, 146, 54-61.
- Árnason, K., 2006a: *TEM TD. Programme for 1D inversion of central-loop TEM and MT data. Short manual*. ÍSOR - Iceland GeoSurvey, Reykjavík, unpublished internal report, 16 pp.
- Árnason, K., 2006b: *TemX. A graphically interactive programme for processing central-loop TEM data. Short manual*. ÍSOR - Iceland GeoSurvey, unpublished internal report, 17 pp.
- Árnason, K., 2008: *The magnetotelluric static shift problem*. ÍSOR - Iceland GeoSurvey, Reykjavík, report ÍSOR-08088, 16 pp.
- Árnason, K., 1989: *Central-loop transient electromagnetic sounding over a horizontally layered earth*. Orkustofnun, Reykjavík, report OS-89032/JHD-06, 129 pp.
- Árnason, K., Björnsson G., Flóvenz, Ó.G., and Haraldsson E.H., 1988: *Geothermal resistivity survey in the Asal Rift in Djibouti*. Orkustofnun, Reykjavík, Report OS-88031/JHS-05, 48 pp.
- Árnason, K., Eysteinnsson, H., and Hersir, G.P., 2010: Joint 1D inversion of TEM and MT data and 3D inversion of MT data in the Hengill area, SW Iceland. *Geothermics*, 39, 13-34.
- Árnason, K., Eysteinnsson, H., and Vilhjálmsson, A. M., 2008: *The Asal geothermal field, Djibouti, geophysical surface exploration 2007-2008*. ÍSOR - Iceland GeoSurvey, Reykjavík, report ÍSOR-2008/019, 74 pp.
- Árnason, K. and Flóvenz, Ó. G., 1995: Geothermal exploration by TEM- soundings in the central Assal Rift in Djibouti, East Africa. *Proceedings of the World Geothermal Congress 1995*, Florence, Italy.
- Árnason, K., Karlsdóttir, R., Eysteinnsson, H., Flóvenz, Ó. G., and Gudlaugsson, S. Th., 2000: The resistivity structure of high-temperature geothermal systems in Iceland. *Proceedings of the World Geothermal Congress 2000, Kyushu-Tohoku, Japan*, 923-928.
- Berdichevsky, M.N., and Dmitriev, V.I., 2002: *Magnetotellurics in the context of the theory of ill-posed problems*. Society of Exploration Geophysicists, USA, 215 pp.
- Berdichevsky, M.N., and Dmitriev, V.I., 2008: *Models and methods of magnetotellurics*. Springer-Verlag, Berlin, Germany, 561 pp.
- Brigham, E.O., 1974: *The fast Fourier transform*. Prentice-Hall, Inc. 252 pp.
- Cagniard, L., 1953: Basic theory of the magneto-telluric method of geophysical prospecting: *Geophysics*, 18, 605-635.
- Christensen, A., Auken, E., and Sørensen, K., 2006: The transient electromagnetic method. *Groundwater Geophysics*, 71, 179-225.
- Clarke, J., Gamble, T.D., Goubau, W.M., Koch, R.H., and Miracky, R.F., 1983: Remote reference magnetotellurics: Equipment and procedures. *Geophys. Prosp.*, 31, 149-170.
- Constable, S.C., Parker, R.L., and Constable, C.G., 1987: Occam inversion: A practical algorithm for generating smooth models from electromagnetic sounding data. *Geophysics*, 52, 289-300.

- Correia, H., Fouillac, C., Gerard, A., and Varet, J., 1985: The Asal geothermal field, Republic of Djibouti. *Geothermal Resources Council, Transactions*, 9, 513-519.
- Corti, G., 2012: Evolution and characteristics of continental rifting: Analog modelling-inspired view and comparison with examples from the East African Rift System. *Tectonophysics*, 522-523, 1-33.
- Dague, Ph., Duroux, J., Lavigne, J., Lopoukhine, M., and Stieltjes, L., 1973: *Prospection géothermique de la région d'Asal. –Rapport de synthese*. BRGM, report 73, SGN 144 GTH.
- deGroot-Hedlin, C., and Constable, S., 1990: Occam inversion to generate smooth, two-dimensional models from magnetotelluric data. *Geophysics*, 55, 1613-1624.
- Delibrias, G., Marinelli, G. and Stieltjes, L., 1975: Assal Rift spreading rate: A geological approach. In: Pilger, A. and Rosler, A. (eds.), *Afar Depression of Ethiopia*, 1, 214-221. Schweizerbart, Stuttgart.
- Demange, J. and Puvilland, P., 1990: *Champ géothermique d'Asal, Djibouti; synthese des donnees*. BRGM, France.
- Dobre, C., 2004: Structure et Mecanismes des Segments de Rift Volcano-Tectoniques. Etudes de Rift Anciens (Ecosse, Islande) et d'un Rift Active (Asal-Ghoubbet). PhD thesis, University of Maine 422 pp.
- Dobre, C., Manighetti, I., Dorbath, I., Dorbath, C., Bertil, D., Delmond, J.C., 2007: Crustal structure and magmato-tectonic process in an active rift (Asal-Ghoubbet, Afar, East Africa): 2. Insights from the 23-year recording of seismicity since the last rifting event. *J. Geoph. Res.* 112, B05406 1029, 32 p.
- Egbert, G.D., and Booker, J.R., 1986: Robust estimation of geomagnetic transfer functions. *Geophys. J.R. Astr. Soc.*, 87, 173-194.
- EOS, 2007: *Geophysics foundations: Physical properties: Electrical resistivity of geologic materials*. Department of Earth, Ocean and Atmospheric Sciences, website: www.eos.ubc.ca/ubcgif/iag/foundations/properties/resistivity.htm
- Flóvenz, Ó.G., 1984: Application of the head-on resistivity profiling method in geothermal exploration. *Geothermal Resources Council, Transactions*, 8, 493-498.
- Flóvenz, Ó.G., Hersir, G.P., Saemundsson, K., Ármannsson, H and Fridriksson, Th., 2012: Geothermal energy exploration techniques. In: Sayigh, A., (ed.) *Comprehensive renewable energy*, 7. Elsevier, Oxford, 51-95.
- Flóvenz, Ó.G., Spangenberg, E., Kulenkampff, J., Árnason, K., Karlsdóttir, R., and Huenges, E., 2005: The role of electrical interface conduction in geothermal exploration. *Proceedings of the World Geothermal Congress 2005, Antalya, Turkey*, 9 pp.
- Fouillac, C., Fabriol, R., and Lundt, F., 1983: *Champ géothermique d'Asal. Synthèse des données disponibles au 1er janvier 1983*. Report 83SGN022GTH, 71 pp.
- Gamble, T.D., Goubau, W.M., and Clarke, J., 1979: Magnetotellurics with a remote magnetic reference. *Geophysics*, 44, 53-68.
- Goubau, W.M., Gamble, T.D., and Clarke, J., 1979: Magnetotelluric data analysis: removal of bias. *Geophysics*, 43, 1157-1169.
- Hersir, G.P., and Árnason, K., 2010: Resistivity of rocks. Paper presented at the “Short Course V on Exploration for Geothermal Resources”, organized by UNU-GTP, GDC and KenGen, at Lake Bogoria and Lake Naivasha, Kenya, 8 pp.

- Hersir, G.P., Árnason, K., and Vilhjálmsson, A., 2013: 3D inversion of magnetotelluric (MT) resistivity data from Krýsuvík high temperature area in SW Iceland. *Proceedings of the 38th Workshop on Geothermal Reservoir Engineering, Stanford University, Stanford, CA*, 14 pp.
- Hersir, G.P., and Björnsson, A., 1991: *Geophysical exploration for geothermal resources. Principles and applications*. UNU-GTP, Iceland, report 15, 94 pp.
- Jones, A.G., and Groom, R.G., 1993: Strike angle determination from the magnetotelluric impedance tensor in the presence of noise and local distortion: Rotate at your peril. *Geophys. J. Internat.*, 113, 524–534
- Karato, S. 1990: The role of hydrogen in the electrical conductivity of the upper mantle. *Nature*, 347, 272–273.
- Kariya, K.A., and Shankland, T.J., 1983: Electrical conductivity of dry lower crustal rocks. *Geophysics*, 48-1, 52-61.
- Lepine, J.C. and Hirn, A., 1992: Seismotectonics in the Republic of Djibouti, linking the Afar Depression and the Gulf of Aden. In: C.J. Ebinger, H.K. Gupta and Nyambok (editors), *Seismology and related sciences in Africa. Tectonophysics*, 209, 65-86.
- Manzella, A., 2007: *Geophysical methods in geothermal exploration*. Italian National Research Council, International Institute for Geothermal Research, Pisa. Web page: cabierta.uchile.cl/revista/12/articulos/pdf/A_Manzella.pdf, 40 pp.
- Mortensen, A. K., Guðmundsson, Á. Steingrímsson, B., Sigmundsson, F., Axelsson, G., Ármannsson, H., Björnsson, H., Ágústsson, K., Sæmundsson, K., Ólafsson, M., Karlsdóttir, R., Halldórsdóttir, S., and Hauksson, T., 2009: *Krafla geothermal system.conceptual model*. ÍSOR - Iceland GeoSurvey, Reykjavík, report ÍSOR-2009/057, LV-2009/111 (in Icelandic), 206 pp.
- Nabighian M.N., and Macnae, J.C., 1991: Time domain electromagnetic prospecting methods. In: Nabighian M.N (ed.), *Electromagnetic methods in applied geophysics*, 2. Society of Exploration Geophysicists, Tulsa, OK, 427–520.
- Naidu, G.D., 2012: *Deep crustal structure of the Son-Narmada-Tapti lineament, Central India*. Springer Theses, Springer-Verlag, Berlin, Heidelberg.
- Ngoc, P.V., Boyer, D., Mouel, J.L., and Cortillot, V., 1981: Identification of a magma chamber in the Ghoubbet-Asal Rift (Djibouti) from a magnetotelluric experiment. *Earth and Planetary Science Letters* 52, 372-382.
- Oldenburg, D.W., and Li, Y., 2005: Inversion for applied geophysics: a tutorial. Invited chapter in: *Near-surface geophysics, SEG investigations in geophysics*, 13, 89-150.
- Palacky, G.V., 1987: Resistivity characteristics of geologic targets. In: *Electromagnetic methods in applied geophysics*, vol. 1, Theory, 1351.
- Parkinson, W., 1959: Directions of rapid geomagnetic variations. *Geophys. J. R. Astr. Soc.* 2, 1–14.
- Pellerin, L., and Hohmann, G.W., 1990: Transient electromagnetic inversion: A remedy for magnetotelluric static shifts: *Geophysics*, 55-9, 1242-1250
- Phoenix Geophysics, 2005: *Data processing user guide*, Phoenix Geophysics Ltd., Toronto, ON Canada.

- Phoenix Geophysics, 2009: *V5 system 2000 MT/MTU. A user guide*. Phoenix Geophysics Ltd., Toronto, ON, 178 pp.
- Reddy, I.K., Rankin, D., and Phillips, R.J., 1977: Three-dimensional modelling in magnetotelluric and magnetic variational sounding. *Geophys. J. R. Astr. Soc.*, 51, 313-325.
- Rosenkjær, G.K., 2011: *Electromagnetic methods in geothermal exploration. 1-D and 3-D inversion of TEM and MT data from a synthetic geothermal area and the Hengill geothermal area, SW Iceland*. University of Iceland, Faculty of Earth Sciences, MSc. thesis, 137 pp.
- Rowland, B.F., 2002: *Time-domain electromagnetic exploration*. Northwest Geophysical Associates, Inc., 6 pp.
- Royal Observatory of Belgium, 2015: *SILSO data/image*. Website: www.sidc.be/silso/monthlyssnplot.
- Ruegg J.C., Lépine, J.C., and Tarantola A., 1979: Geodetic measurements of rifting associated with a seismo-volcanic crisis in Afar. *Geoph. Res. Letters*, 6, 817-820.
- Saemundsson, K., 1988: *Djibouti geothermal project. Analysis of geological data pertaining to geothermal exploration of Asal rift*. United Nations Development Programme, report, 18 pp.
- San Juan, B., Michard, G., and Michard, A., 1990: Origine des substances dissoutes dans les eaux des sources thermales et des forages de la région Asal-Goubhet (République de Djibouti). *J. Volcanology and Geothermal Research*, 43, 333-352
- Simpson, F., and Bahr, K., 2005: *Practical magnetotellurics*. Cambridge University Press, Cambridge, UK, 254 pp.
- Siripunvaraporn, W., and Egbert, G., 2000: An efficient data-subspace inversion method for 2-D Magnetotelluric data. *Geophysics*, 65, 791-803.
- Siripunvaraporn, W., and Egbert, G., 2009, WSINV3DMT: vertical magnetic field transfer function inversion and parallel implementation. *Physics of the Earth and Planetary Interiors*, 173, 317-329.
- Siripunvaraporn, W., Egbert, G., Lenbury, Y., and Uyeshima, M., 2005: Three-dimensional magnetotelluric inversion: data-space method. *Phys. Earth Planet. Interiors*, 150, 3-14.
- Siripunvaraporn, W., Egbert, G., Lenbury, Y., and Uyeshima, M., 2006: *WSINV3DMT version 1.0.0 for single processor machine user manual*. Mahidol University, Faculty of Science, Department of Physics, Bangkok, 21 pp.
- Smith, J.T., and Booker, J.R., 1991: Rapid inversion of two- and three-dimensional magnetotelluric data. *J. Geophys. Res.*, 96, 3905-3922.
- Spies, B.R., and Frischknecht, F.C., 1991: Electromagnetic sounding. In: Nabighian, M.N., (ed.), *Electromagnetic methods in Applied Geophysics*. Investigations in Geophysics, Vol. 2A, SEG.
- Sternberg, B.K., Washburne, J.C., and Pellerin, L., 1988: Correction for the static shift in magnetotellurics using transient electromagnetic soundings. *Geophysics*, 53, 1459-1468.
- Stieltjes, L., 1976: Research for a geothermal field in a zone of oceanic spreading: Examples of the Asal Rift. *Proceedings of the 2nd UN Symposium on the Development and Use of Geothermal Resources. San Francisco Vol. 1*, 613-623.
- Stieltjes, L., 1979: *Carte géologique du Rift d'Asal, 1:50,000*. CNRS/BRGM/ISERST.

Stieltjes, L., Joron, J.L., Treuil M., Varet J., 1976: Le rift d'Asal, segment de dorsale émergé, discussion pétrologique et géochimique. *Bull. Soc. Géol. France*, 18-4, 851-862

Swift, C. M., 1967: A magnetotelluric investigation of an electric conductivity anomaly in the southwestern U.S. MIT, Boston, PhD. Thesis, 211 pp.

Tikhonov, A.N., 1950: The determination of electrical properties of the deep layers of the Earth's crust. *Dokl. Aad. Nauk. SSR*, 73, 295-297 (in Russian).

Vergne J., Doubre, C., Mohamed K., Dujardin A., and Leroy, S., 2012: The lithospheric structure beneath mature continental rifts: New insights from a dense seismic profile across the Asal-Ghoubbet Rift (Djibouti). *Addis Ababa Afar Rift Symposium*.

Vilhjálmsson, A.M., Flóvenz, Ó.G., Karlsdóttir, R., Árnason, K., Eysteinnsson, H. and Saemundsson, K., 2008: Geophysical evidence for magmatic transport in the lower Crust in Iceland. *Poster at AGU conference 2008, Paper no., MR43A-1803*.

Violay, M., Gibert, B., Azais, P., Lods, G. and Pezard, P.A. 2012: A new cell for electrical conductivity measurement on saturated samples at upper crust conditions. *Transport in Porous Media*, 1, 1-11.

Vozoff, K., 1972: The magnetotelluric method in the exploration of sedimentary basins. *Geophysics*, 37, 98-141.

Vozoff, K., 1991: The magnetotelluric method. In: *Electromagnetic methods in applied geophysics. Vol 2B. Application*. Soc. Expl. Geophys., Tulsa, OK., 972 pp.

WestJEC, 2012: *Enhancement of planning capacity for geothermal energy development in African countries*. Course by Japan International Cooperation Agency (JICA) and West Japan Engineering Consultants, Inc. (West JEC), Fukuoka, Japan, July, 233 pp.

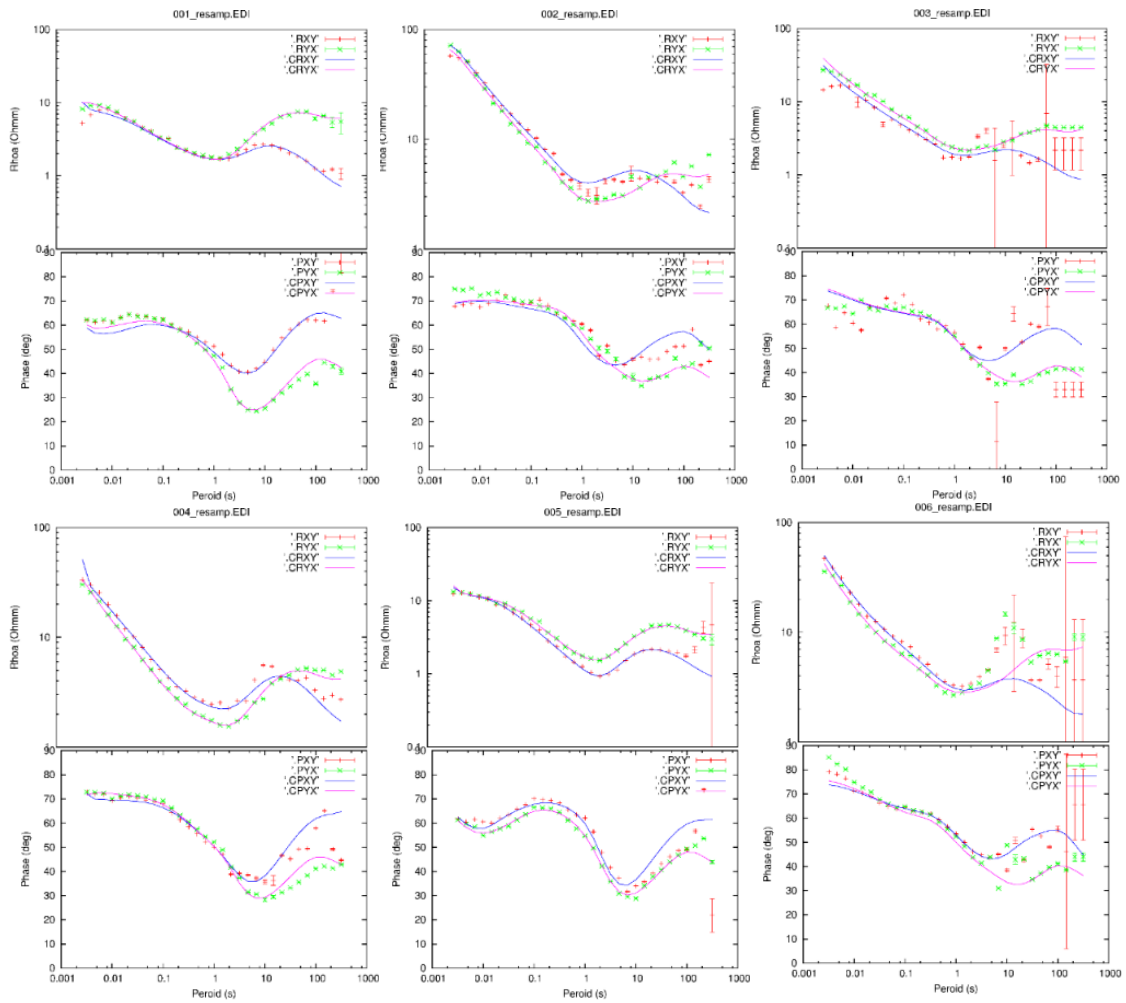
Wiese, H., 1962: Geomagnetische Tiefentellurik, Teil 2, Die Streichrichtung der Untergrundstrukturen des elektrischen Widerstandes, erschlossen aus geomagnetischen Variationen, *Geofis. Pura. Appl.* 52, 83-103.

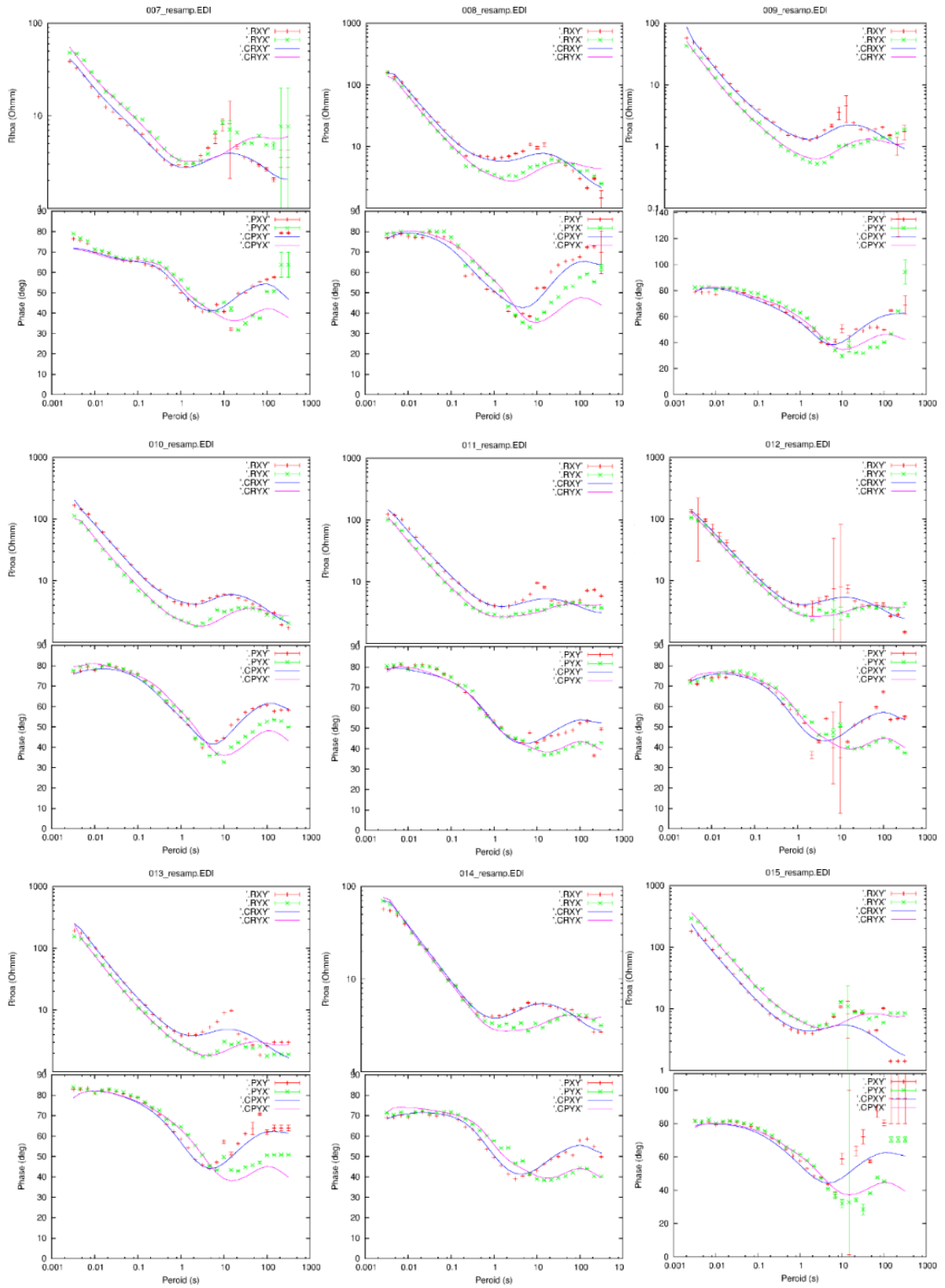
Geographic.org, 2015: Website: www.geographic.org/maps/new2/djibouti_maps.html

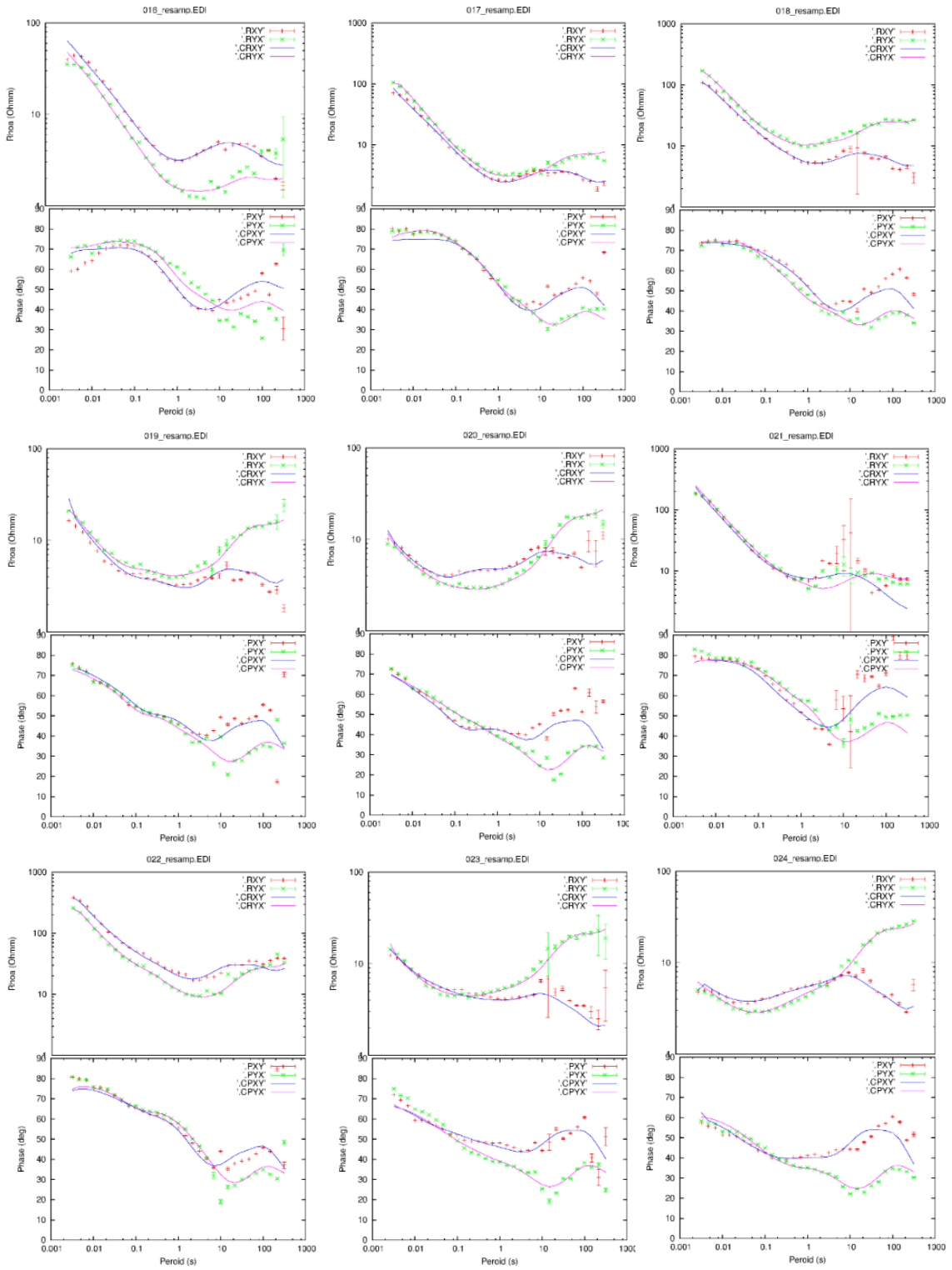
Zhang, P., Roberts, R.G., and Pedersen, L.B., 1987: Magnetotelluric strike rules, *Geophysics*, 52, 267-278.

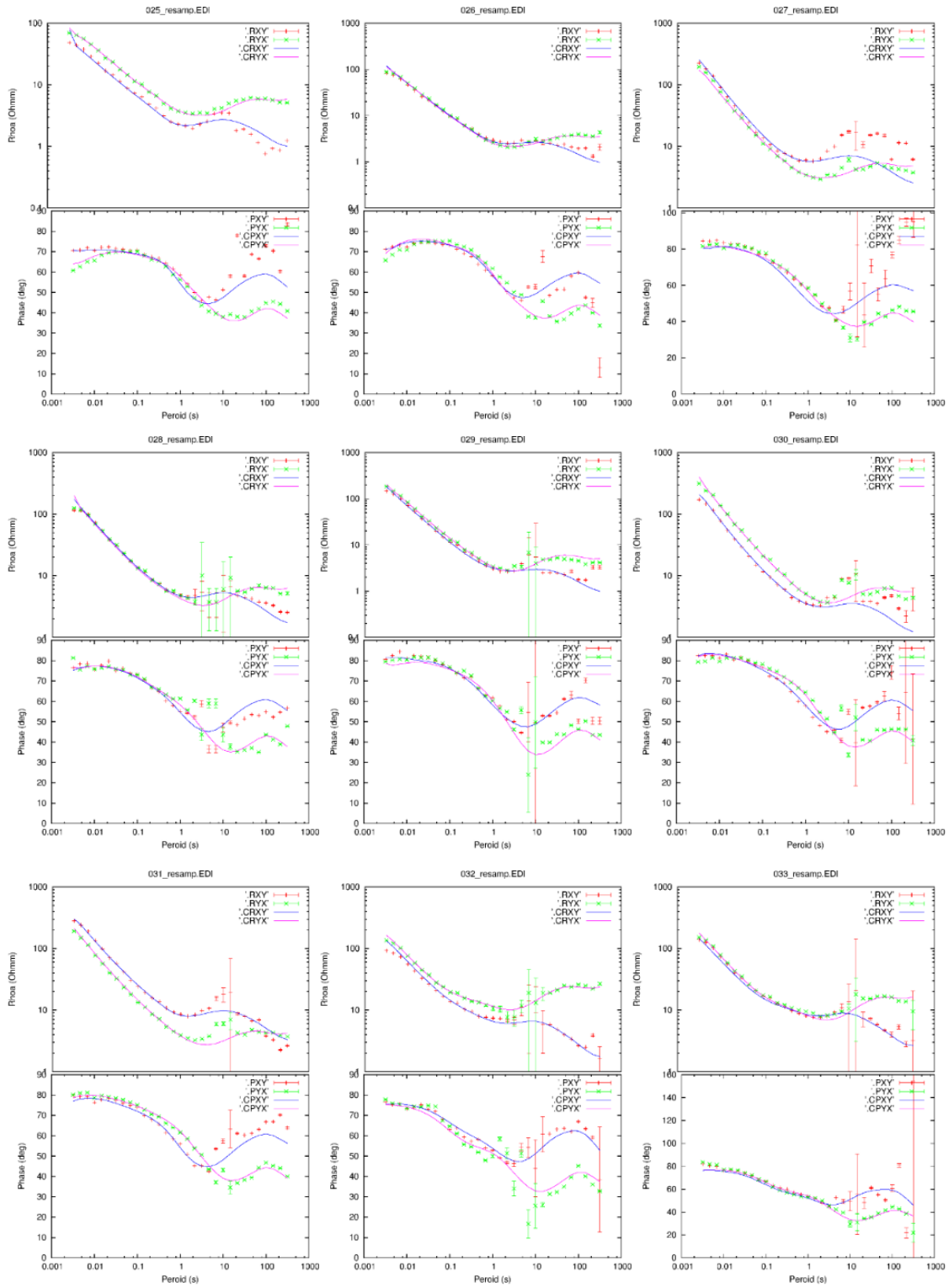
APPENDIX A: 3-D MT inversion responses

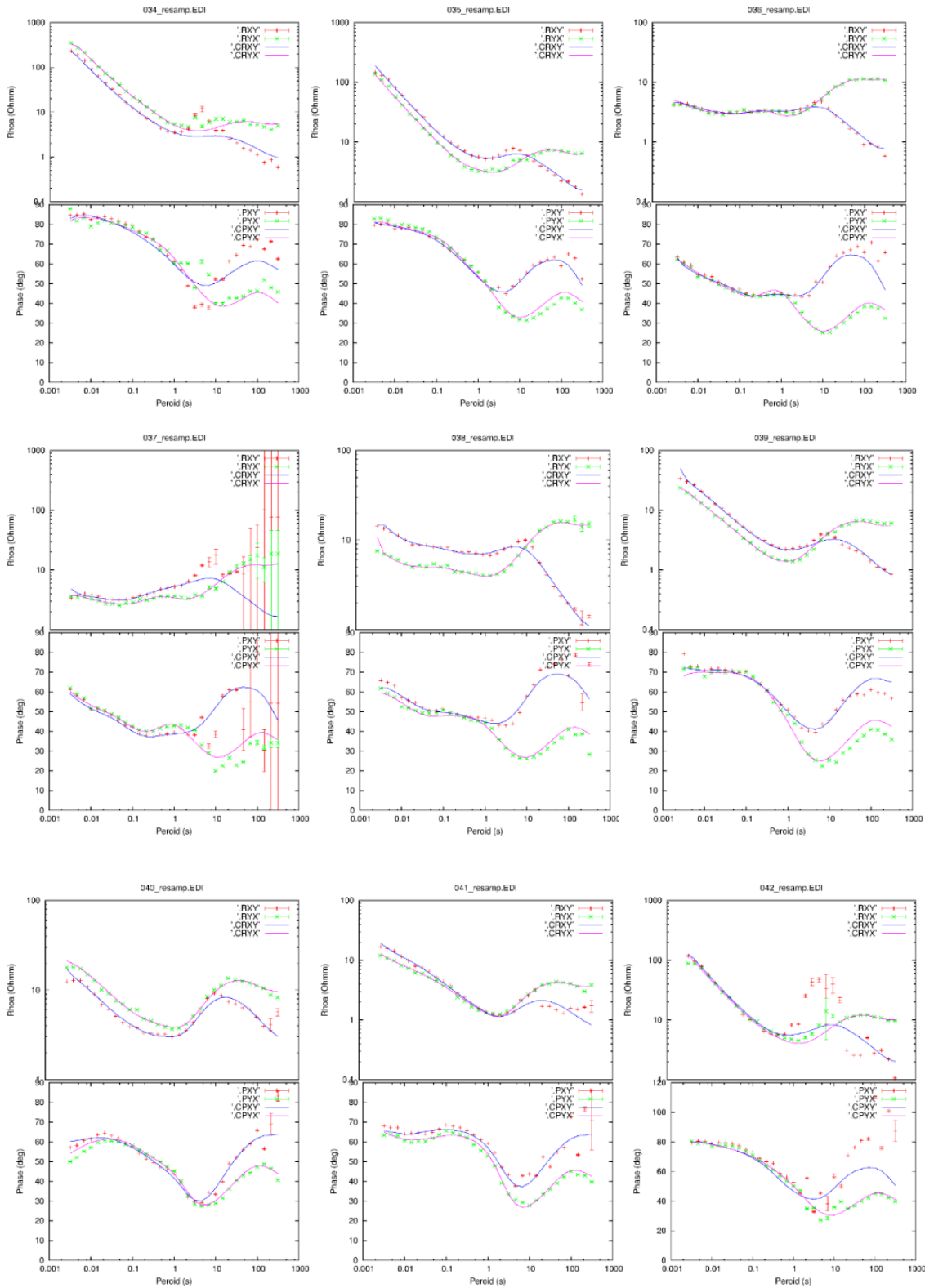
A comparison of the measured data for all the inverted 105 MT soundings (presented as apparent resistivity, ρ_{xy} , ρ_{yx} and the apparent phase, ϕ), and the calculated responses of the final model from the homogeneous $10 \Omega\text{m}$ initial model. The data misfit is defined as the RMS (Root-Mean-Square) of the difference between the measured and calculated values of the off-diagonal tensor elements (real and imaginary parts). The RMS misfit for the final model from the homogeneous $10 \Omega\text{m}$ initial model was 1.48. Blue and purple solid lines: calculated responses of apparent resistivity and phase for the xy and yx polarization, respectively. Red and Green crosses: the measured static shift corrected apparent resistivity and phase data for the xy and yx polarization, respectively.

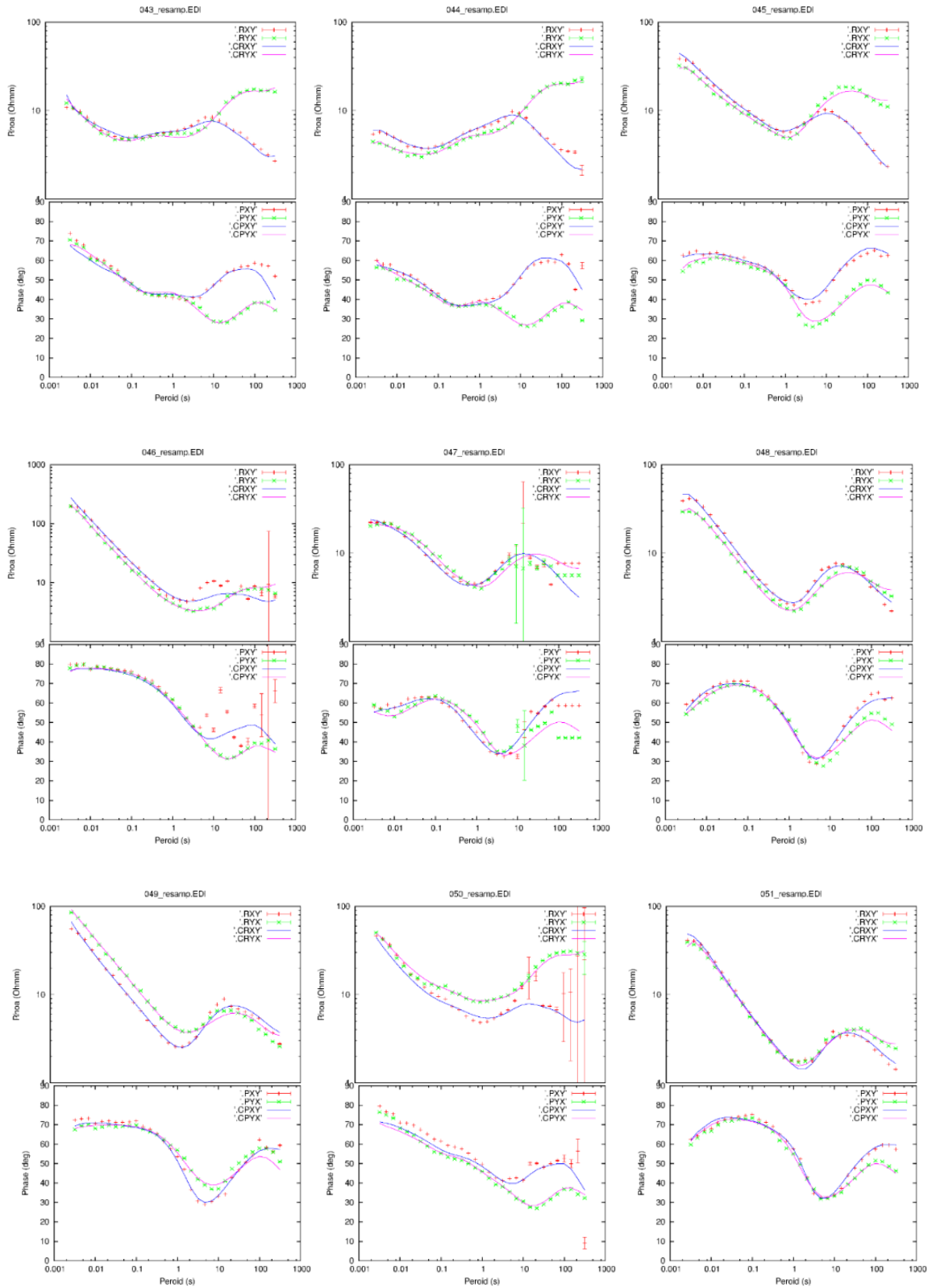


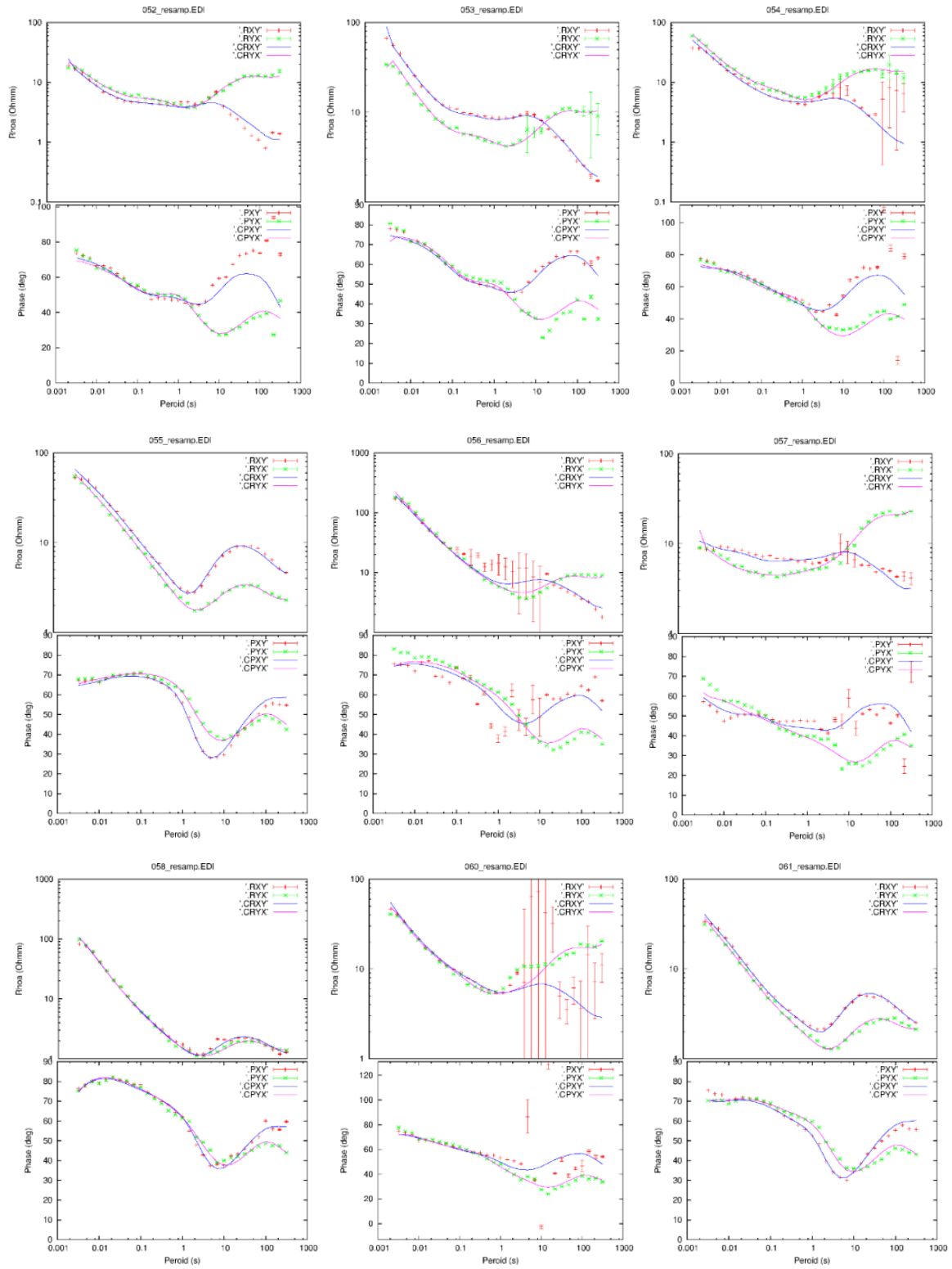


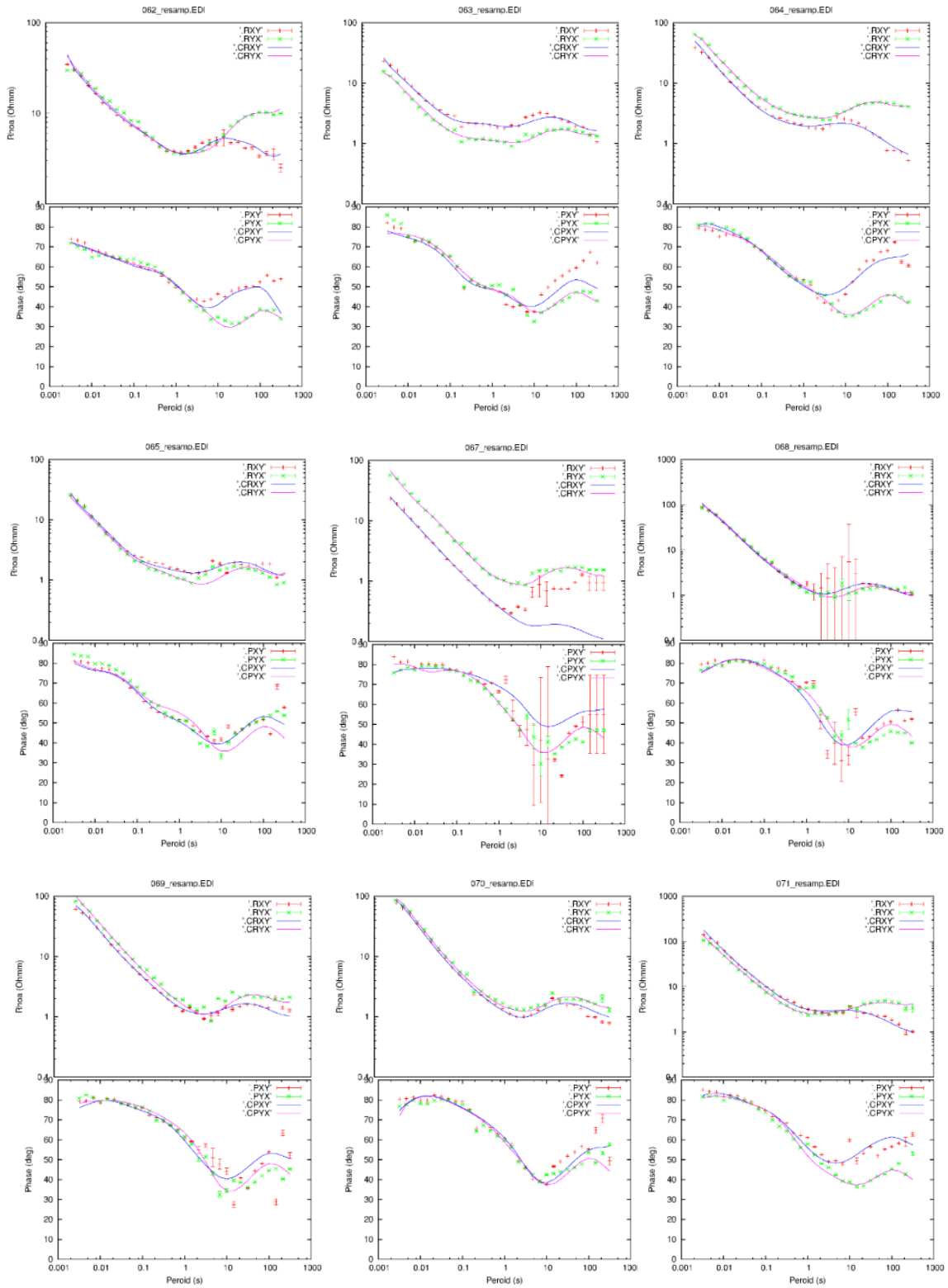


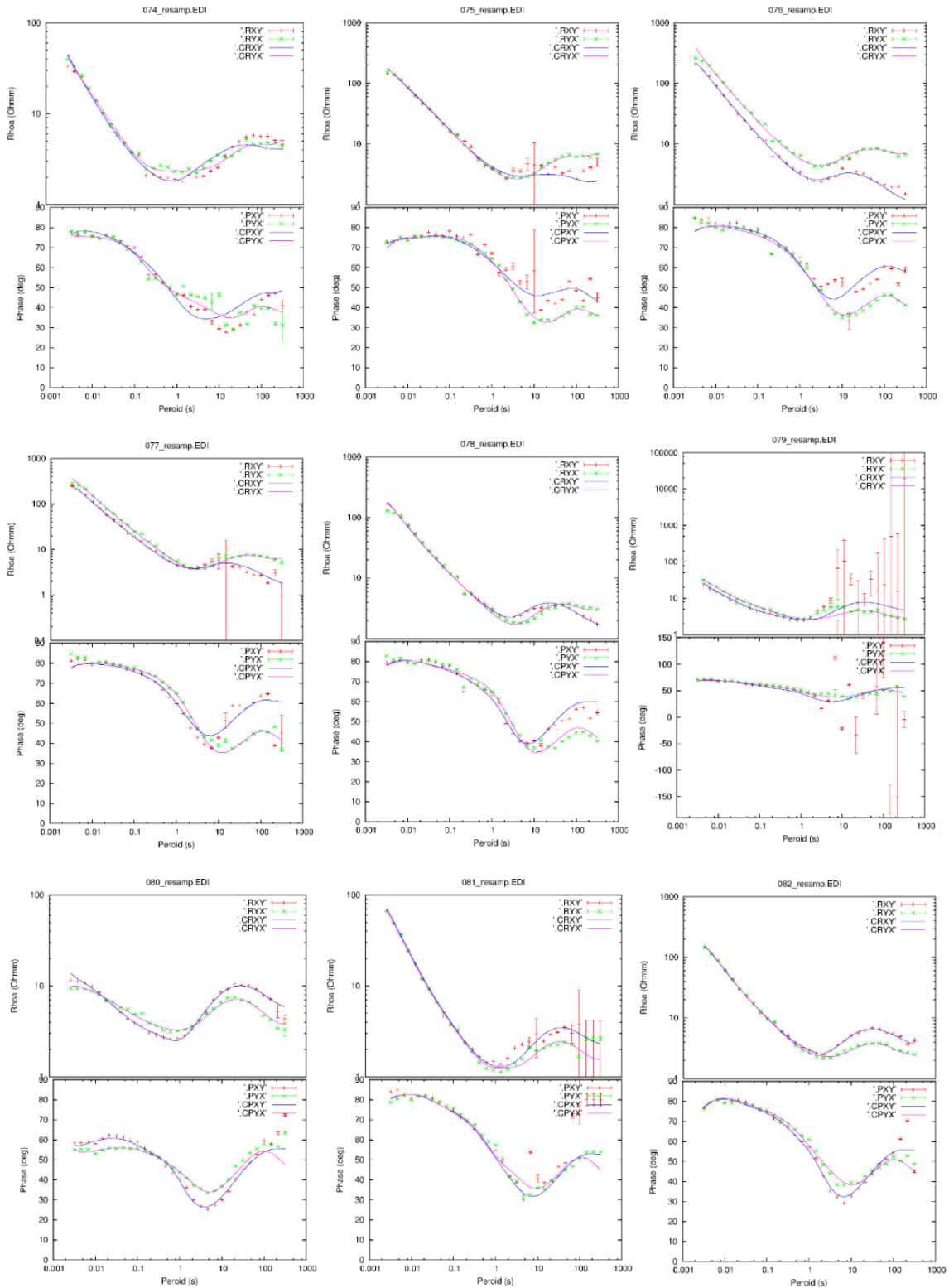


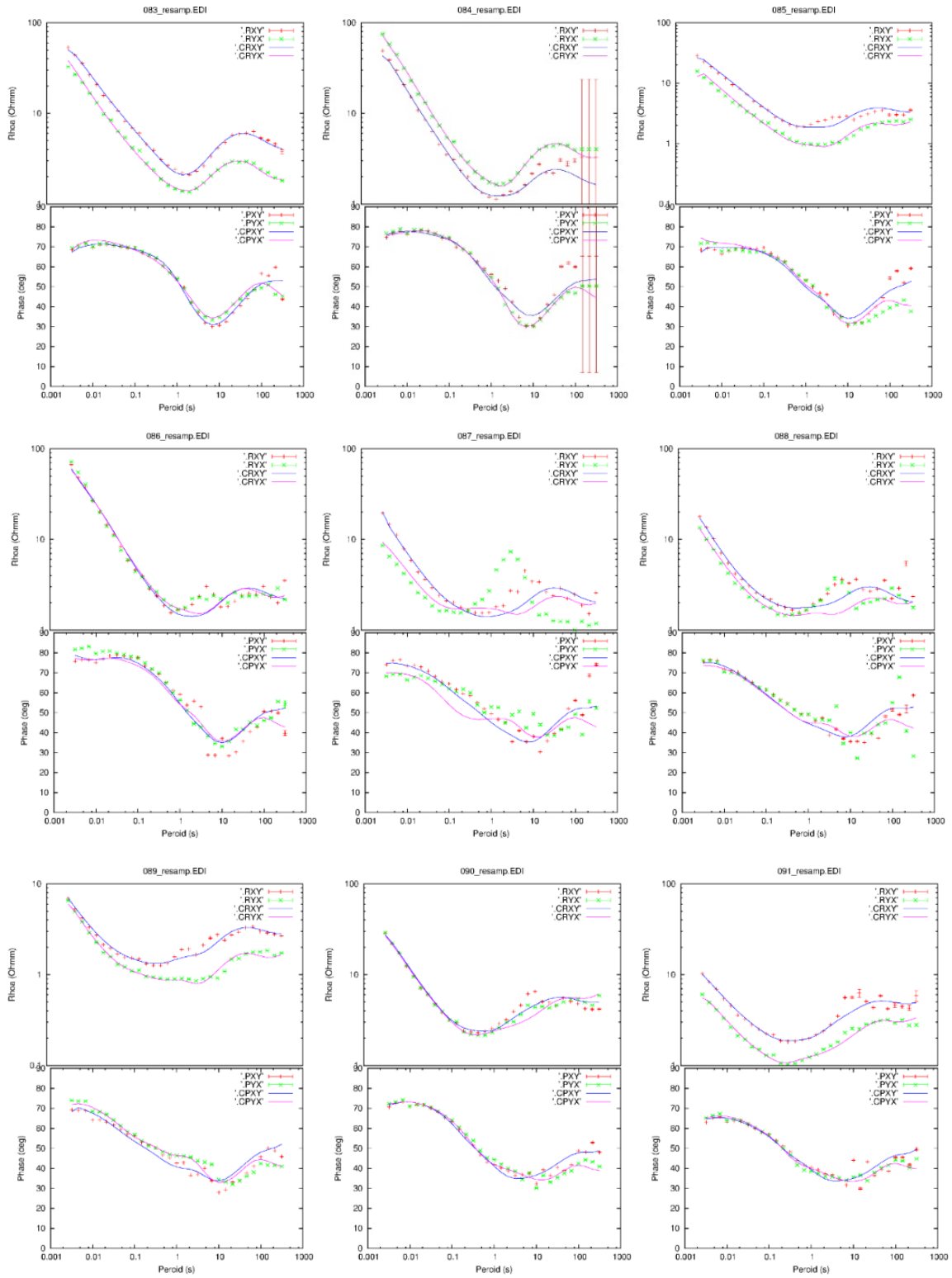


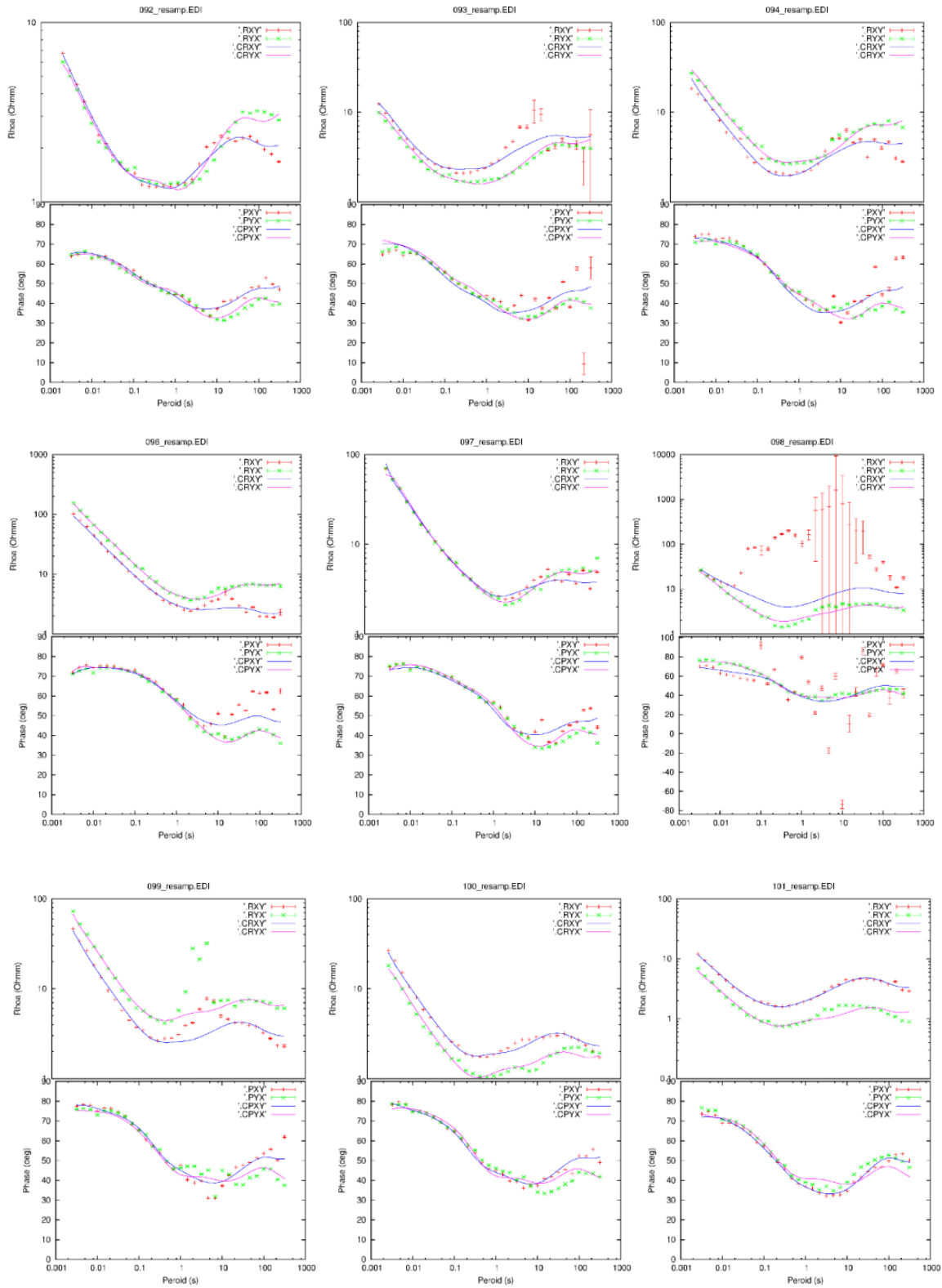


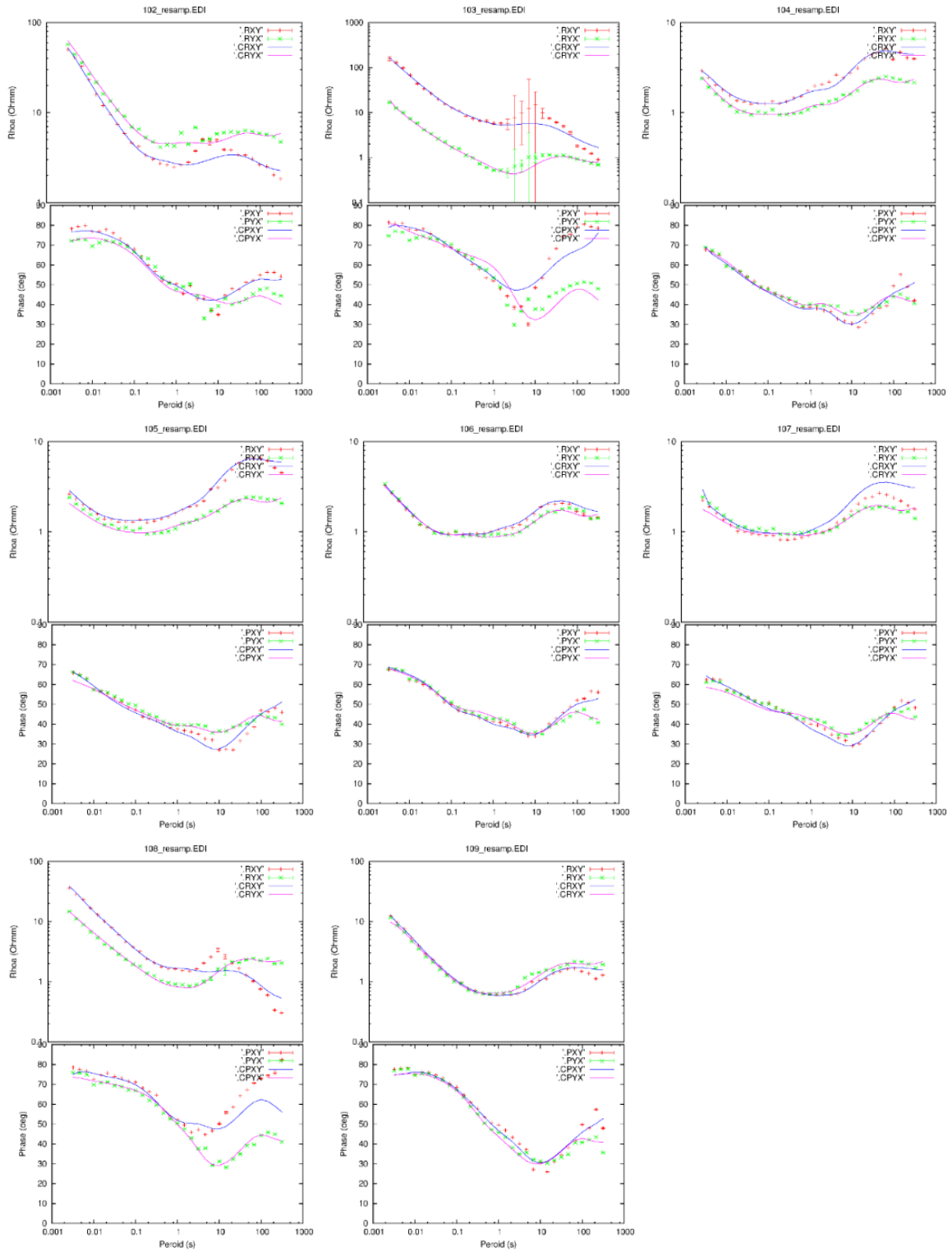






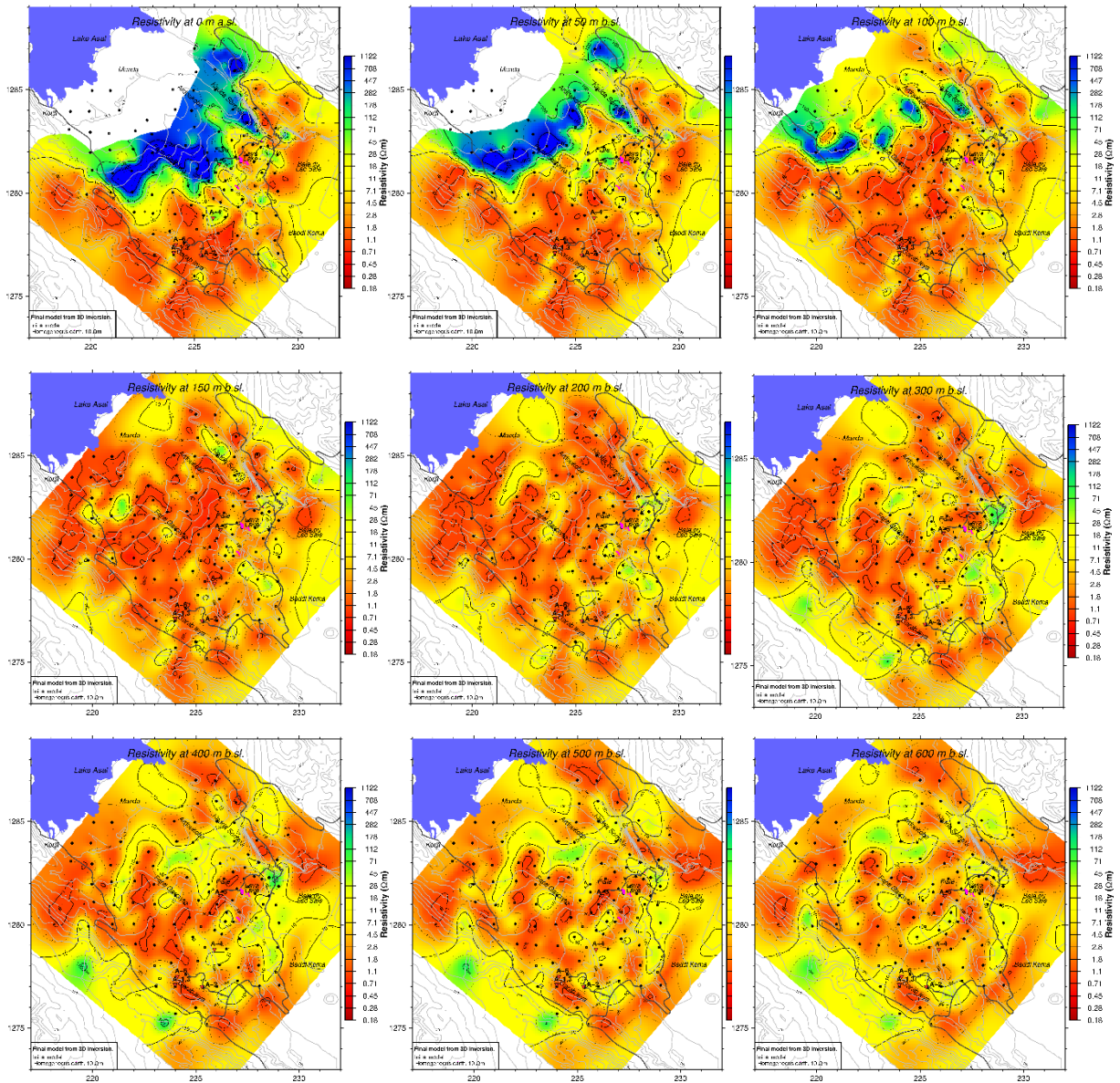


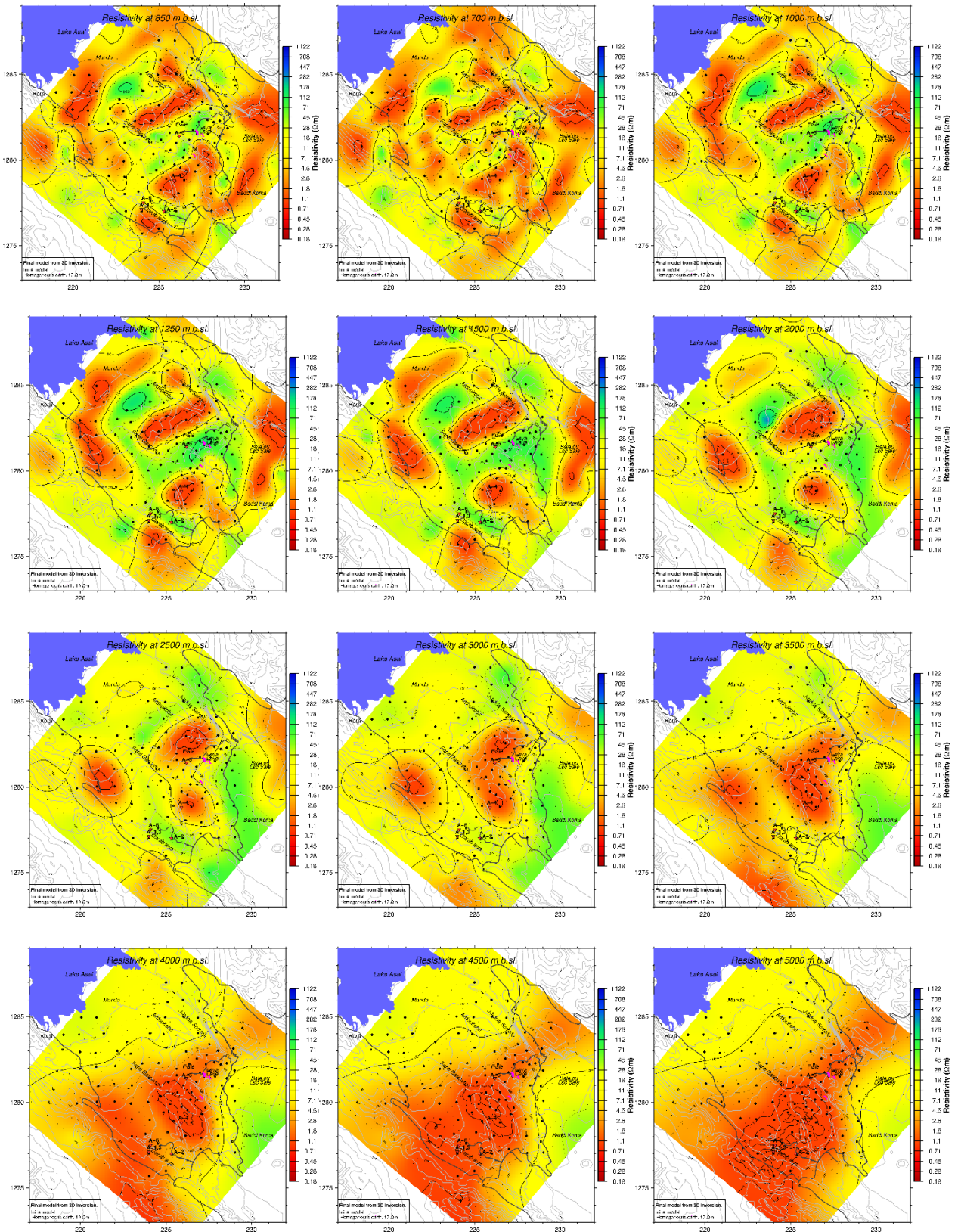


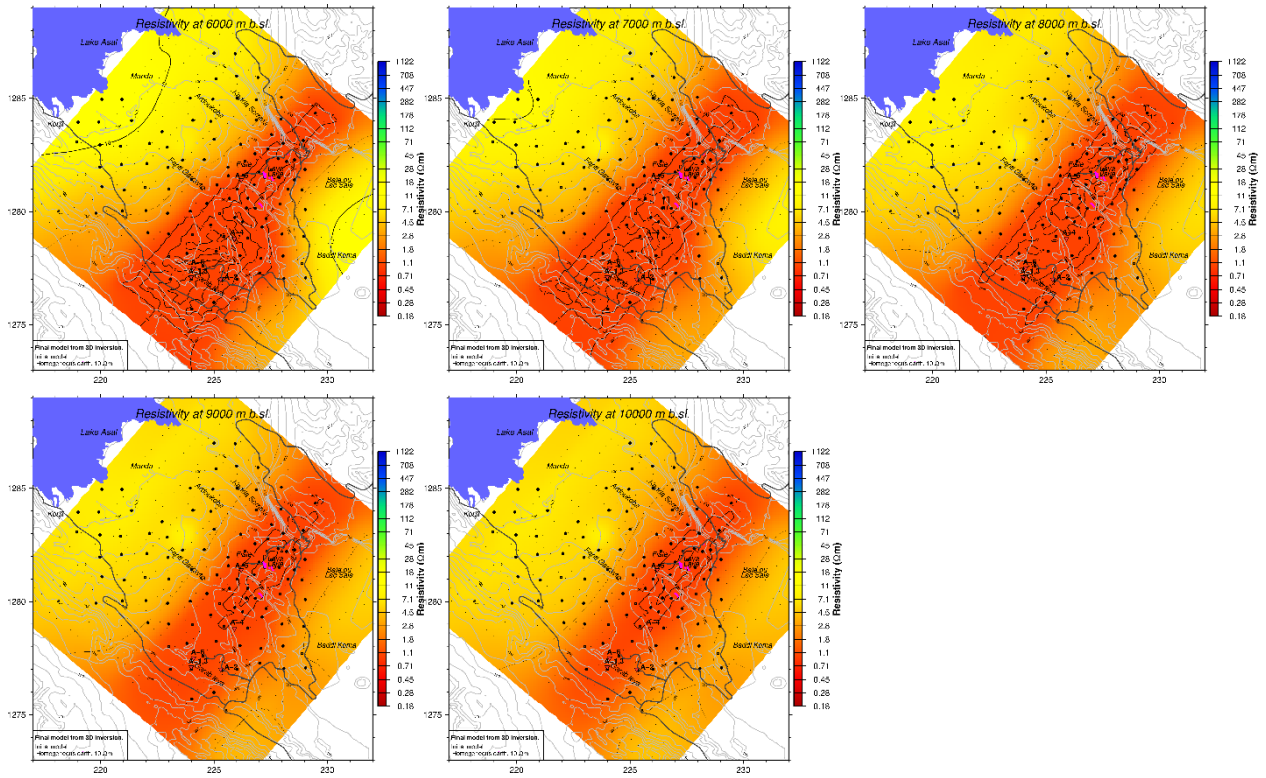


APPENDIX B: Iso-resistivity maps produced from 3-D inversion

The resistivity models are drawn and presented as smoothed resistivity maps reproduced from 3-D inversion with homogeneous 10 Ωm initial model after the elevation correction. Black dots: MT soundings; geothermal surface manifestations are shown by purple; black line: road; thin grey lines: topographic contour lines in m a.s.l. Coordinates are UTM coordinates, zone 38N; WGS84. Distances are given in km.







APPENDIX C: Resistivity cross-sections

Resistivity cross-sections along the Asal rift (NS-E); parallel to the x-axis of the internal coordinate system:

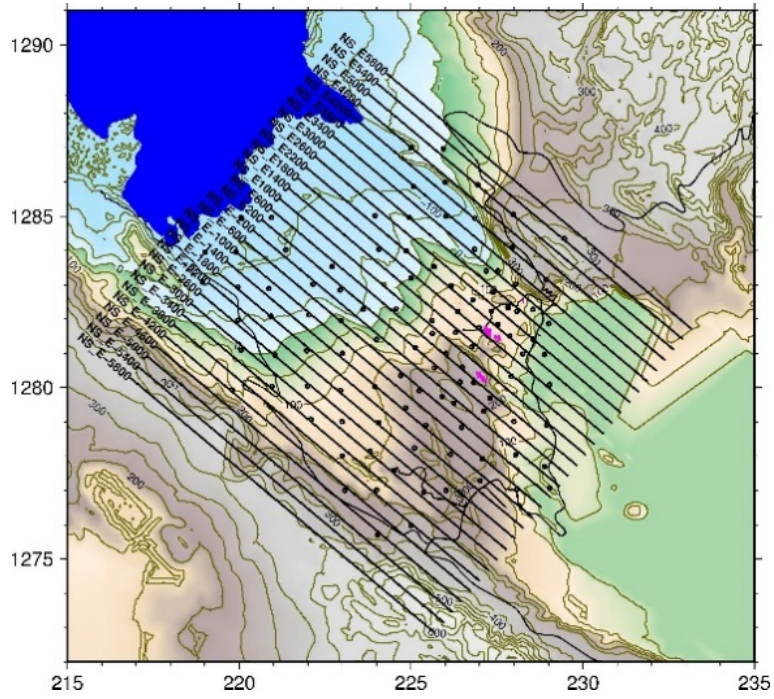
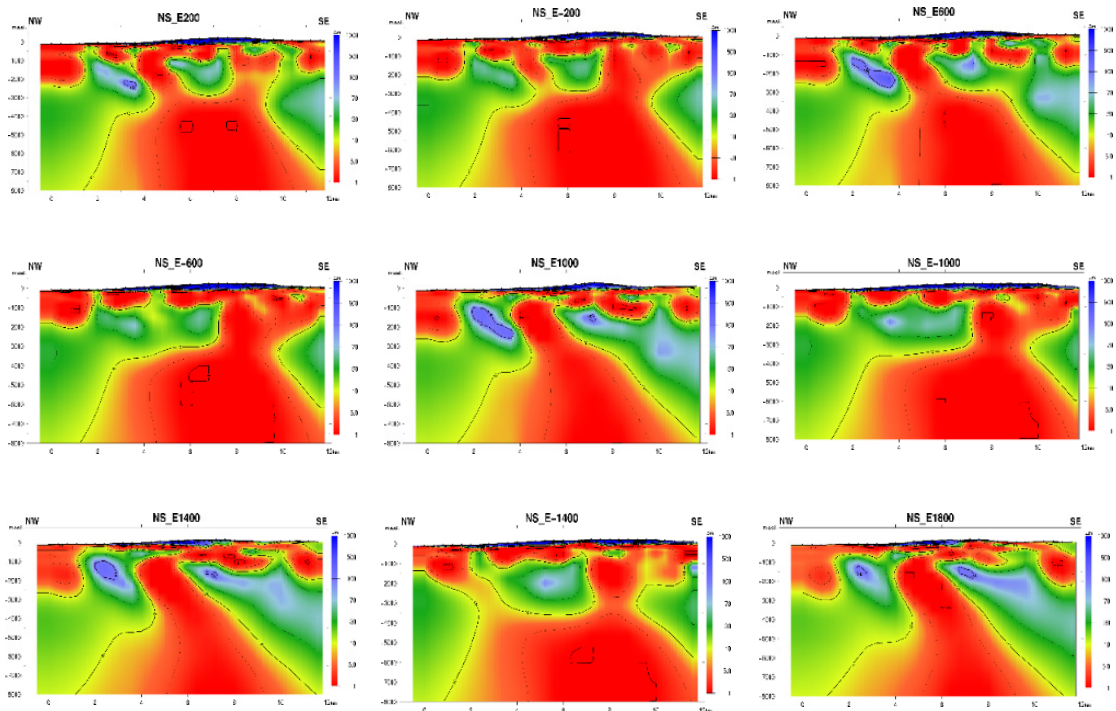
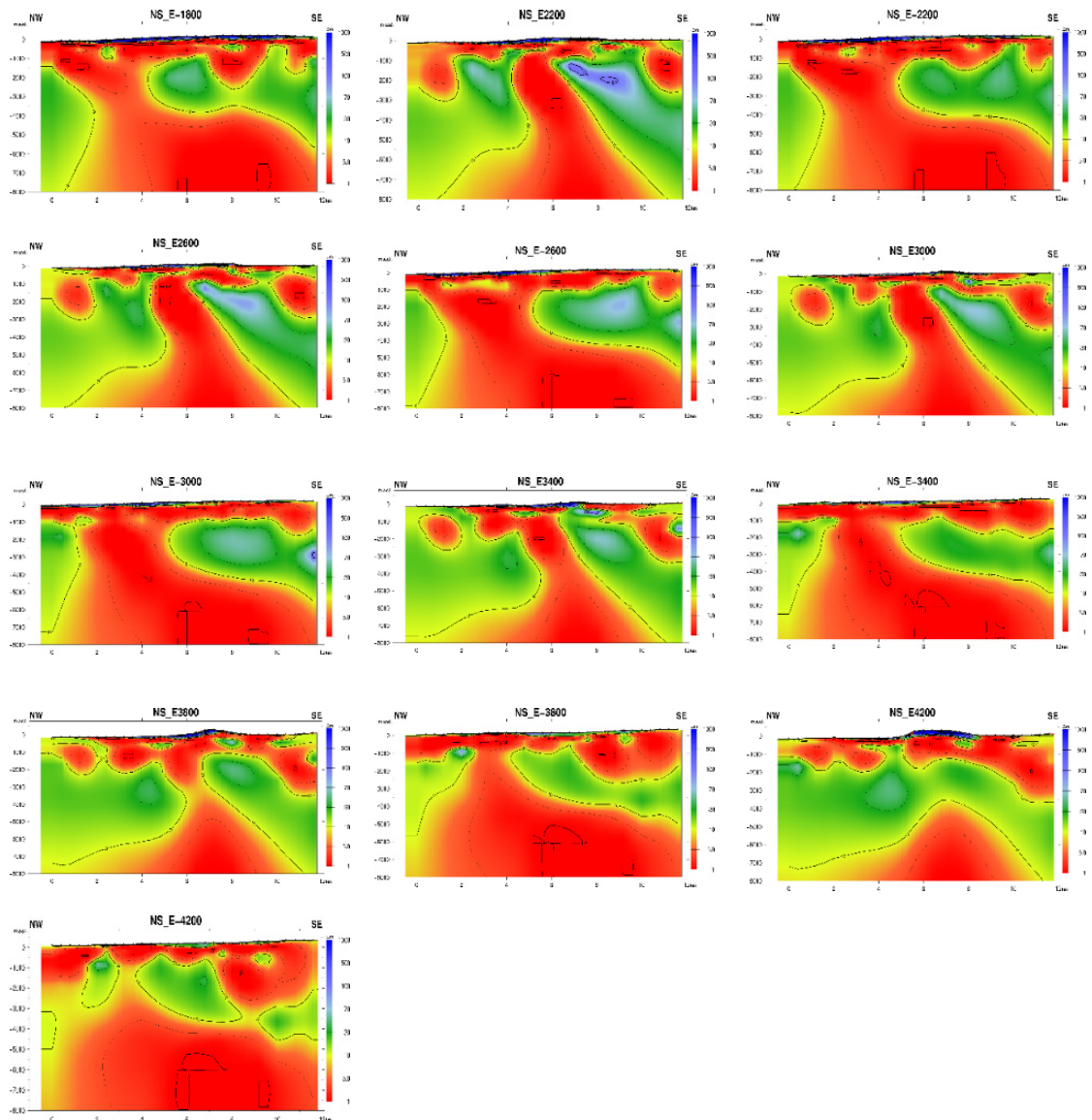


FIGURE 1: Map showing the location of the cross-sections





Resistivity cross-sections across the Asal rift (EW-N); parallel to y-axis of the internal coordinate:

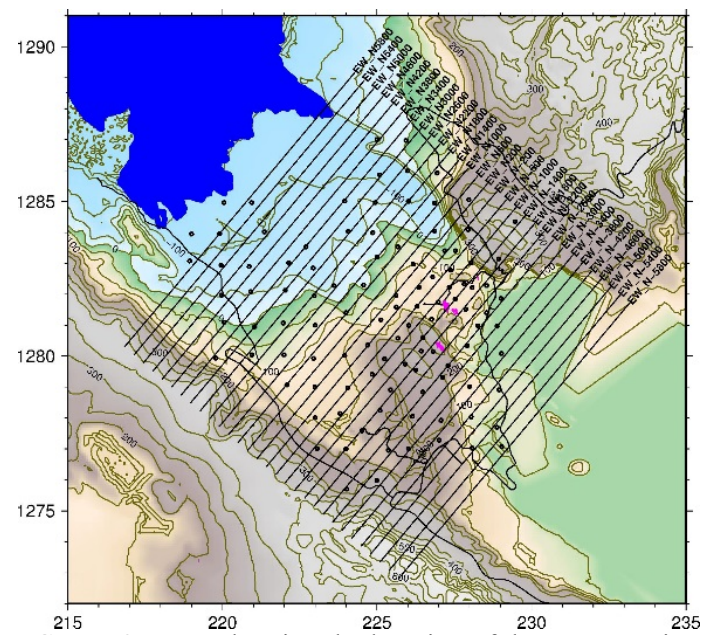


FIGURE 2: Map showing the location of the cross-sections

